Rare-Earth Doped Photonic Crystal Fibre Lasers and Amplifiers

Hougaard, Kristian G.

Publication date:
2005

Document Version
Publisher's PDF, also known as Version of record

Rare-Earth Doped Photonic Crystal Fibre Lasers and Amplifiers

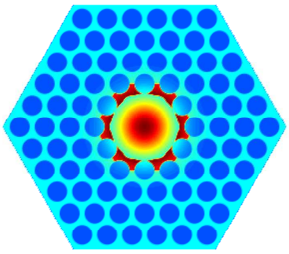

Kristian Hougaard

Ph.D. Thesis

February 28th, 2005

Rare-Earth Doped
Photonic Crystal Fibre Lasers and Amplifiers

Ph.D. Thesis

Kristian Hougaard

Supervisors:
Jesper Lægsgaard, COM
Jes Broeng, Crystal Fibre A/S
Anders Bjarklev, COM

Research Center COM
Technical University of Denmark
Building 345V
2800 Kgs. Lyngby
Denmark

Preface

This thesis has been written as part of the requirements to obtain the Ph.D. title at the Technical University of Denmark. The work presented in this thesis have been carried out at Research Center COM, in the period March 1st, 2002 to February 28th, 2005.

The supervisors of the Ph.D. project were Associate Professor Jesper Lægsgaard and Professor Dr. Techn. Anders Bjarklev from Research Center COM and Ph.D. Jes Broeng from Crystal Fibre A/S.

I would like to thank all my supervisors for the inspiration and guidance they have provided throughout the project period. Thanks also to all my colleagues at Research Center COM, who have really made COM a great place to work. In particular I wish to thank my good friends and colleagues Dr. Riishede, Dr. Sørensen, Dr. Alkeskjold, and Dr. Hansen. Thank you for all the discussions, your invaluable support, and many many enjoyable hours.

Kristian Hougaard
DTU, February 28th, 2005

Abstract

In this thesis, a theoretical and numerical study of the use of rare-earth-doped photonic crystal fibres as optical amplifiers and lasers, has been performed.

Photonic crystal fibres or microstructured optical fibres is a new kind of optical fibre in which the cladding region typically consist of a periodic microstructure, resulting in a fibre with very different properties compared to conventional optical fibres.

The properties of photonic crystals fibres are described, with focus on the advantages this technology provides compared to conventional fibres, within the area of optical amplification.

The thesis also presents the basic properties of optical amplification, and describes the numerical model developed to model the behaviour of lasers and amplifiers based on photonic crystal fibres.

The developed numerical tools are then used to investigate specific applications of photonic crystal fibres. Their novel properties allow for design of optical fibre amplifiers and fibre lasers with superior performance, compared to solutions based on conventional fibres.

The primary applications considered are high efficiency fibre amplifiers based on index guiding photonic crystal fibres, and cladding pumped air-guiding fibre lasers, based on photonic bandgap guiding fibres.

Resumé

Denne afhandling omhandler en teoretisk og numerisk undersøgelse af fotoniske krystalfibre, og mulighederne for at benytte disse fibre til optisk forstærkning ved dotering med sjældne jordarter.

Fotoniske krystalfibre eller mikrostrukturerede fibre er en relativ ny klasse af optiske fibre, hvor kapperegionen typisk består af en periodisk mikrostruktur. Dette resulterer i fibre med markant anderledes egenskaber end konventionelle optiske fibre.

Ved hjælp af numeriske modeller beskrives de optiske egenskaber for disse fibre, med fokus på de fordele denne teknologi giver indenfor optisk forstærkning.

Afhandlingen præsenterer også mekanismerne bag optisk forstærkning i doterede fibre og beskriver den numeriske model, der er udviklet, til at modellere egenskaberne af lasere og forstærkere baseret på fotoniske krystalfibre.

De udviklede værktøjer bliver benyttet til at undersøge specifikke områder, hvor egenskaberne af fotoniske krystalfibre kan udnyttes til at designe fiberforstærkere og fiberlasere med forbedrede egenskaber, sammenlignet med løsninger baseret på konventionelle fibre.

Hovedområderne, der er beskrevet, er effektive fiberforstærkere, baseret på indexguidende fotoniske krystalfibre, og kappepumpede luftguidende fiberlasere, baseret på båndgabsguidende krystalfibre.

Contents

Chapter 1

Introduction

The development of silica based optical fibres with acceptable losses [1], led to an intense research within optical communication systems. First the wavelength region around 800 nm was used, then single-mode fibres, lower losses, and zero dispersion around 1300 nm lead to the use of the second telecommunication window, and finally dispersion shifted fibres and even lower losses resulted in the today most common wavelength interval, the third telecommunication window, around 1550 nm. At this point the performance of optical communication systems was limited by the losses in the fibres, and this lead to an extensive research within the area of optical amplification. The goal was to avoid the expensive and complicated electrical detection and regeneration, and in stead amplify the optical signal directly. This goal was achieved with the development of the *erbium doped fibre amplifier* (EDFA), which revolutionised the communication industry [2]. EDFAs had a number of excellent properties, which made them ideal for optical communication systems, such as high gain, low noise, bit-rate insensitivity, and broad bandwidth. Also the fibre nature of EDFAs results in polarisation insensitivity and easy integration with existing systems [3]. These excellent properties have made EDFAs, or more general, *rare-earth doped* (RED) fibre amplifiers a vital component in optical communication systems.

RED fibres have also gained extensive use as fibre lasers. Advances in

pump technology and advanced double cladding structures, combined with the excellent beam qualities have made RED fibre lasers, with very high output powers, commercially available [4], making fibre lasers a viable alternative within areas such as medicine [5], material processing [6], and sensor technology [7].

Recently a new class of optical fibres, *photonic crystal fibres* (PCFs), have been developed [8]. PCFs have a range of special properties, which makes them interesting for many applications, including RED fibre amplifiers and lasers. The main subject of this thesis is the combination of the two technologies RED fibres and photonic crystal fibres.

The remainder of this thesis is organised in the following way:

Chapter 2 presents fundamental aspects of PCFs, and the guiding mechanisms and basic waveguiding properties are described. The numerical modelling techniques are presented, and finally the areas of bandgap-guiding PCFs and air-guiding PCFs are investigated.

Chapter 3 discusses the area of optical amplification in RED PCFs. The mechanisms of light/matter interactions are described, and the important area of double cladding structures is discussed. Then the advantages and challenges of using PCFs as active fibres is investigated, and finally the development of a numerical model to simulate RED PCFs is presented.

Chapter 4 describes the design of highly efficient amplifiers based on PCFs. By tightly confining the pump and signal in a small core fibre, it is possible to design fibre amplifiers that can be operated at very low pump powers.

Chapter 5 presents the idea of using double cladding air-guiding PCFs as fibre lasers. In air-guiding fibres the majority of the power is located in the hollow core, which makes it possible to increase the maximum power delivery of fibre laser system. The possibilities and limitation are thoroughly described based on numerical calculations.

Chapter 6 holds the conclusion of this thesis.

Chapter 2

Photonic Crystal Fibres

Microstructured fibres or *photonic crystal fibres* (PCFs) is a relatively new class of optical waveguides that was first mentioned by Knight et al. in 1996 [8]. PCFs have many novel properties, which makes them interesting for a range of applications.

In this chapter the concepts of PCFs and the basic waveguiding properties of these fibres are described. In section 2.2 theoretical tools, developed to analyse optical properties of these fibres, are presented. Finally important types of PCFs and important PCF applications are described.

The aim of this chapter is not to give an exhaustive description of all possible applications of PCFs. Focus will be on the properties and applications investigated throughout this project period. Other important areas, such as supercontinuum generation and dispersion management, are only briefly touched upon. For a comprehensive description of PCFs the reader is directed to the introductory book by Bjarklev, Broeng, and Bjarklev [9] or the numerous publications which are still emerging on these subjects.

2.1 Basic concepts of Photonic Crystal Fibres

PCFs are optical fibres which have a microstructered refractive index profile in the fibre cross section. Typically these fibres are made from pure silica, and the cladding structure of the fibre contains a number of periodically arranged air holes, running along the length of the fibre. The core of the fibre typically consist of pure silica.

2.1.1 Microstructered Cladding Structure

The cladding structure of PCFs consists of multiple materials (where air is counted as a material), with different refractive indices, typically arranged in a microstructered periodic array. Fig. 2.1 shows an example of a cladding structure, which is a triangular arrangement of air holes in a silica background. Each dark blue circle indicate an air hole, which runs along the entire length of the PCF. The index profile of the fibre is therefore invariant along this direction, defined as the z-direction. Triangular lattices, as the one showed, are the most used structure, but other possibilities such as square lattices [10], honeycomb lattices [11] or even random hole distributions have been published [12]. Also, the typical air/silica fibres can also be enhanced with doped regions in the core and/or cladding [13], or the microstructure can be made solely by doping, thus avoiding the air holes [14].

The period of the lattice is in the same order of magnitude as the wavelength of the light. These small structures mean that the cladding material may be seen as a single material, with a refractive index somewhere in between the refractive indices of the separate material components. This average refractive index is determined by examining the light propagation in the composite material and finding the frequencies and propagation constants of the allowed modes in the structure. An effective index, as known from conventional fibre optics, is then defined as:

$$n_{\text{eff}} = \frac{\beta}{k} \tag{2.1}$$

where β is the propagation constant, and k is the free-space wave number. The effective index of the material is defined by the allowed mode with

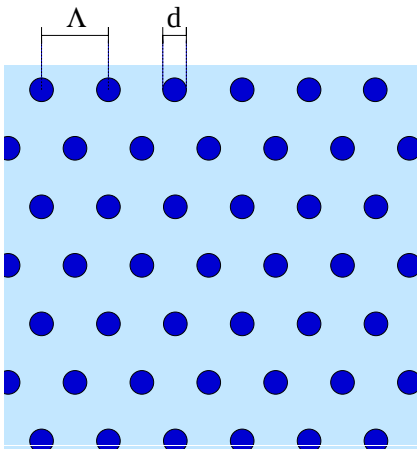

Figure 2.1: *PCF cladding structure with a triangular periodic arrangement of air holes in a silica background. The two fundamental parameters defining the structure are indicated: The distance between 2 neighbouring air holes, the pitch, is denoted* Λ*, and the diameter of the air holes is denoted,* d*. Typically a normalized value,* d/Λ *is used to specify the hole size.*

the highest effective index, also known as the *fundamental space-filling mode* (FSM) of the cladding structure [15].

The effective indices of such microstructured materials are highly wavelength dependent. In the low frequency limit, the solution converges towards plane waves, and the effective index become a weighted average of the refractive index of the constituent materials. Analytical expressions for this effective index, can, for certain geometries, be found [16]. In the high frequency limit, modes can be completely confined to the high index material, and the effective index will converge towards the highest index in the structure. In this case, however, assuming the material is a homogeneous material with an effective index, might not be accurate.

The effective index for the simple triangular structure shown in Fig. 2.1, as a function of normalized frequency, $\frac{\Lambda}{\lambda}$, is shown in Fig. 2.2. The index for three different hole sizes is shown. The background material has a refractive index of 1.45, which is the index value used for silica throughout this thesis, when material dispersion is neglected. It is easy

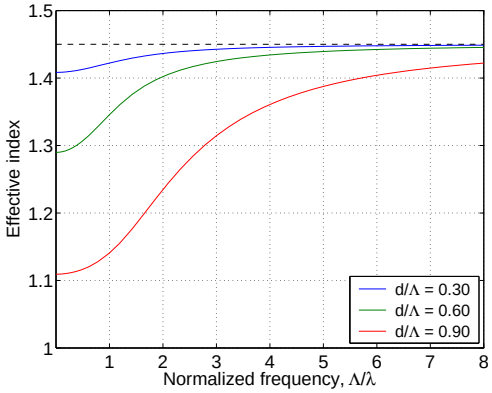

Figure 2.2: *Effective refractive index of a triangular structure of air holes in silica, as a function of normalized frequency. Curves for three different hole sizes are shown. The background material has a refractive index of 1.45, as indicated by the horizontal dashed line.*

to get an intuitive feeling for the qualitative behaviour of the effective index curves shown. At long wavelengths the light spreads out into the holes, resulting in a low effective index. For high frequencies, the light is confined to the high index areas.

2.1.2 Introducing a Fibre Core

Locally breaking the symmetry in the periodic lattice creates a region, with different mode solutions, compared to the unperturbed region. This may be used to create the core in the photonic crystal fibre.

The simplest and most widely used method, is to omit a single air hole, which creates a region with a higher index compared to the cladding region. Light may then be guided in the core region, since the effective index of the cladding region is lower than the index in the core. Such fibres are referred to as index-guiding PCFs. The guiding mechanism is often referred to as *modified total internal reflection* (MTIR), which strongly resembles the principle of *total internal reflection* (TIR), which is well known from conventional optics, including *conventional optical fibres* (COFs).

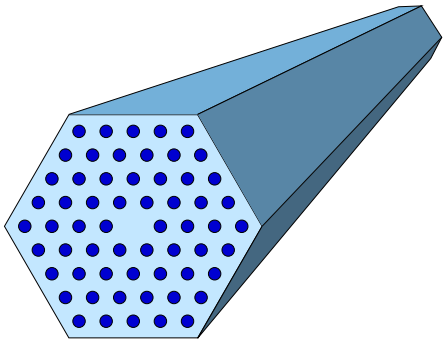

(a) Schematic illustration of a PCF.

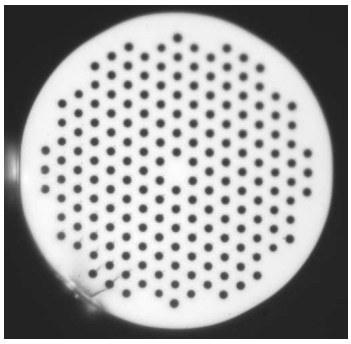

(b) SEM picture of a PCF. Picture is courtesy of Crystal Fibre A/S.

Figure 2.3: *Examples of index guiding photonic crystal fibres. The cross sections contain air holes, and a core is formed by excluding a single air hole. The index distributions are invariant in the z-direction.*

Two examples of index guiding PCFs are shown in Fig. 2.3. The schematic (a) shows the triangular cladding structure, and the core formed by removing a single air hole. The third invariant dimension is indicated. Fig. 2.3(b) show an actual PCF, fabricated at Crystal Fibre A/S [17]. The diameter of the shown structure is approximately the size of a human hair.

PCFs may also guide light by a fundamentally different mechanism, known as the *photonic bandgap* (PBG) effect. However, before the properties of PCFs are further investigated, different approaches to numerically investigating the behaviour of PCFs will be described.

2.2 Modelling of Photonic Crystal Fibres

Numerous modelling techniques exist for simulating electromagnetic wave propagation. During this project period two methods have been extensively used: The plane wave method and the finite difference method. In this section an introduction to these methods are given.

2.2.1 Electromagnetic wave propagation

The wave propagation in PCFs are governed by Maxwell's equations, which define the time and space dependency of the electric and magnetic fields:

$$\nabla \cdot \mathbf{D} = \rho \tag{2.2}$$
$$\nabla \cdot \mathbf{B} = 0 \tag{2.3}$$
$$\nabla \times \mathbf{E} = -\frac{\partial \mathbf{B}}{\partial t} \tag{2.4}$$
$$\nabla \times \mathbf{H} = \mathbf{j} + \frac{\partial \mathbf{D}}{\partial t} \tag{2.5}$$

where $\mathbf{E}$ and $\mathbf{H}$ are the macroscopic electric and magnetic fields, and $\mathbf{D}$ and $\mathbf{H}$ are the electric and magnetic flux densities, related through:

$$\mathbf{D} = \epsilon_0 \epsilon \mathbf{E} \tag{2.6}$$
$$\mathbf{B} = \mu \mathbf{H} \tag{2.7}$$

$\mathbf{j}$ is the current density, and ρ is the charge density. Since only non-magnetic, non-conductive materials are considered $\mathbf{j} = 0$ and $\rho = 0$. Assuming a harmonic time dependency of the electric and magnetic field, these can be written as.

$$\mathbf{E}(\mathbf{r}, \mathbf{t}) = \mathbf{E}(\mathbf{r}) \exp(\mathbf{i}\omega\mathbf{t}) \tag{2.8}$$
$$\mathbf{H}(\mathbf{r}, \mathbf{t}) = \mathbf{H}(\mathbf{r}) \exp(\mathbf{i}\omega\mathbf{t}) \tag{2.9}$$

Using this (2.2)-(2.5) becomes:

$$\nabla \cdot \mathbf{D} = 0 \tag{2.10}$$
$$\nabla \cdot \mathbf{H} = 0 \tag{2.11}$$
$$\nabla \times \mathbf{E} = -i\omega\mu_0 \mathbf{H} \tag{2.12}$$
$$\nabla \times \mathbf{H} = i\omega\epsilon_0 \epsilon \mathbf{E} \tag{2.13}$$

Combining (2.12) and (2.13) it is possible to eliminate either one of the fields, formulating an equation using only the $\mathbf{H}$-field or the $\mathbf{E}$-field. Doing this for the $\mathbf{H}$-field yields:

$$\nabla \times \left[\frac{1}{\epsilon} \nabla \times \mathbf{H}\right] = \frac{\omega^2}{c^2} \mathbf{H} \tag{2.14}$$

(2.14) is a Hermitian eigenvalue equation, and is known as the wave equation for the magnetic field. Together with (2.11), this is the basic equation, which needs to be solved. Solving the above equation will give the magnetic field distribution. If the electric field distribution is needed, it may be calculated e.g. by using (2.13).

2.2.2 The plane wave method

The *plane wave method* (PWM) is used to solve periodic electromagnetic problems. The solutions are found as a superposition of plane waves. Since the cladding structures of PCFs are periodic, this method is an excellent choice for determining the allowed solutions in the infinitely periodic cladding structure. For a detailed mathematical description of this method, the reader is referred to [18].

In a periodic structure Bloch's theorem states that any mode may be expanded as an infinite sum of plane waves. Working in the reciprocal space, the problem may be cast as a standard eigenvalue problem, where the eigenvalues are the frequency response to the considered wave vector. This eigenvalue problem may be solved using a standard eigenvalue solver.

In the typical case of a triangular lattice, the structure may be represented by a simple unit cell, as indicated in Fig. 2.4(a). Ultimately it may be shown that the allowed solutions in the cladding structure, for a given propagation constant $\beta = \hat{e}_z \cdot \mathbf{k}$, may be found by calculating the allowed modes for all values of the transverse wave vector $\mathbf{k}$ within the irreducible Brillouin-zone in reciprocal space, indicated by the dark blue region in Fig. 2.4(b). Even though no formal proof exist, experience suggest, that all allowed modes are bound by the modes located along the edge of the irreducible Brillouin-zone. The *MIT Photonic Bands* (MPB) program may be used to find the allowed solutions in the cladding structure, by varying the transverse part of $\mathbf{k}$ along $\Gamma \rightarrow M \rightarrow K \rightarrow \Gamma$.

The actual implementation used is the freely available software package MPB, developed by Steven Johnson [19].

The PWM is extremely efficient at finding the allowed cladding modes, due to the inherent periodicity of the cladding. If a core is introduced,

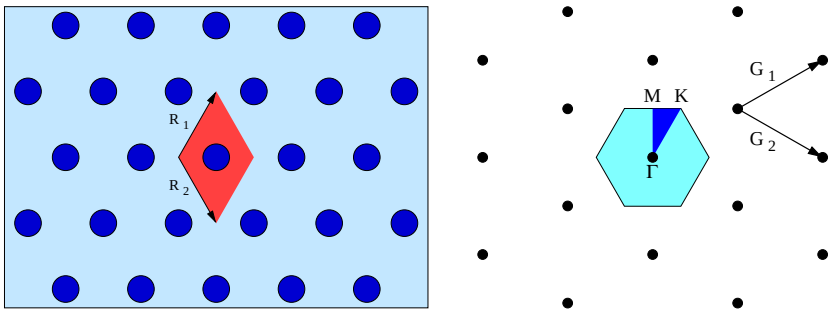

(a) Periodic triangular lattice structure. Red area indicated the unit cell, spanned by the lattice vectors, R_1 and R_2.

(b) Reciprocal lattice, with the reciprocal lattice vectors G_1 and G_2. Colored area indicate the 1st Brillouin-zone, and the irreducible Brillouin-zone with the high-symmetry points.

Figure 2.4: *Real lattice and reciprocal lattice for triangular lattice structure.*

in the form of a lattice defect, the periodicity is broken. The PWM may however still be used, if an artificial periodicity to the problem is imposed. This may be done by also reproducing the defect in the infinite lattice structure, as shown in Fig. 2.5. This is known as the supercell approximation. The computational demands are much higher in this case, since the size of the computational domain has increased significantly. To get an accurate solution, it is necessary to create a supercell, which is large enough, as to prevent coupling between the repeated defects.

For index guiding PCFs, the guided mode has the largest refractive index of all modes. The eigenvalue of this mode is therefore the numerically smallest eigenvalue. The eigensolver in MPB is highly optimized at finding the smallest eigenvalues of the problem, which means that MPB is very efficient when considering index guiding PCFs. When PBG guiding fibres are considered, and defects are introduced, the potential guided mode is no longer found by finding the smallest eigenvalue, this means that special measures have to be taken. Using MPB it is possible to search for the PBG guided modes, by shifting and squaring the eigenvalue spectrum, such that the guided mode again has the smallest eigenvalue. This unfortunately destroys the optimised conditioning of the matrix problem,

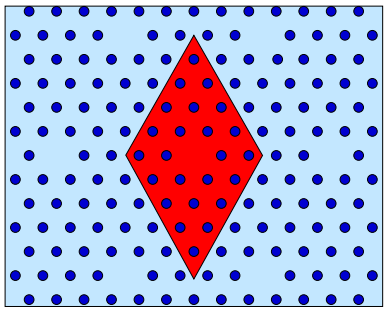

Figure 2.5: *Supercell approximation for the plane wave method. Example of a 5x5 supercell for a triangular lattice structure. Notice the periodic repeating of the core defect.*

and the the convergence becomes significantly slower.

2.2.3 The finite difference method

To overcome this problem (and for a number of other reasons), a finite difference program was developed, primarily, by Ph.D. student Jesper Riishede.

The finite difference method is a direct approach to solving the wave equation from (2.14). A system of linear equations are assembled based on finite difference approximations to the wave equation. The eigensolver of the program use inverse iteration. This means that to find a specific eigenvalue, the eigenvalue spectrum is shifted, and inverted. The desired eigenvalue now becomes the largest eigenvalue, which can be found fast. The price is that the inverse matrix is calculated explicitly, which is memory intensive. Thus memory is sacrificed in order to get a shorter execution time.

Finite difference approximations

In Fig. 2.6 a smooth function $f(x)$ is shown. The function is approximated on a set of discrete points on the x-axis, denoted x_i. The function

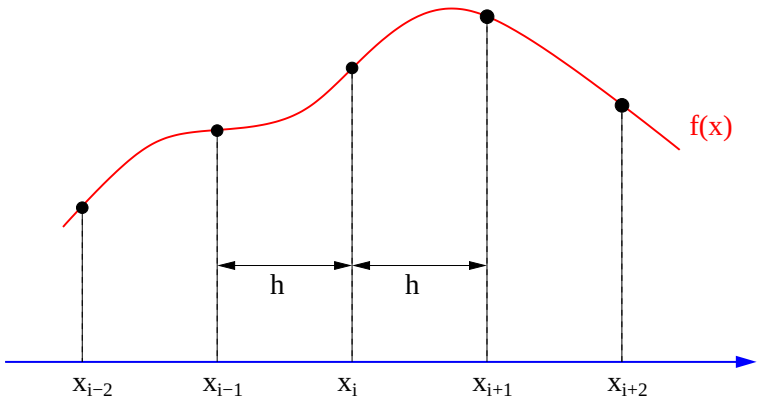

Figure 2.6: *Discretisation of a one dimensional function for use with the finite difference method. The function $f(x)$ is discretised in set of uniformly spaced points.*

values in these points are $f_i = f(x_i)$. The distance between each discrete point is denoted h, and are assumed constant. The n'th order derivative of f is denoted $f^{(n)}$.

The standard finite difference approximation to the derivatives of $f(x)$, may be found by making a Taylor series expansion of f_{i-1} and f_{i+1} around x_i [20]. The expression for the derivatives are:

$$f^{(1)}(x_i) = \frac{f_{i+1} - f_{i-1}}{2h} \tag{2.15}$$

$$f^{(2)}(x_i) = \frac{f_{i-1} - 2f_i + f_{i+1}}{h^2} \tag{2.16}$$

Approximations for varying step sizes may easily be derived, but the developed model only support uniform grids, so this is not shown. (2.15) and (2.16) may easily be expanded to two dimensional problems.

Scalar approximation

The scalar wave equation (Helmholtz equation) may be found from (2.14) by neglecting the derivative of the inverse dielectric function. The result-

ing equation is:

$$\nabla^2\Phi + n^2\frac{\omega^2}{c^2}\Phi = 0 \tag{2.17}$$

Assuming that the field has an $\exp(i\beta z)$ dependency in the z-direction, (2.17) become:

$$\frac{\partial^2\Phi}{\partial x^2} + \frac{\partial^2\Phi}{\partial y^2} + n^2\frac{\omega^2}{c^2}\Phi \;=\; \beta^2\Phi \tag{2.18}$$

The finite difference approximation to this equation then becomes:

$$\frac{\Phi_{i-1,j} - 2\Phi_{i,j} + \Phi_{i+1,j}}{h_x^2} + \frac{\Phi_{i,j-1} - 2\Phi_{i,j} + \Phi_{i,j+1}}{h_y^2} + n^2\frac{\omega^2}{c^2}\Phi_{i,j} = \beta^2\Phi_{i,j} \tag{2.19}$$

where i and j are the index along the x- and y-direction respectively.

Doing this for all points results in a linear set of equations, which may be cast directly into matrix form. It is, however, necessary to decide on a boundary condition. The two most used choices are periodic boundary conditions and metallic boundary conditions. In the first case, the solution is assumed to be periodic using a Neumann boundary condition, and in the latter the field is forced to zero at the boundary, using a Dirichlet boundary condition. A more detailed description of this method may be found in [21].

The scalar approximation neglects the derivative of the dielectric function. This means that the method is valid, when this dirivative is small, i.e. as long as the index contrasts are small. PCFs typically consist of air holes in a silica background material, which means that very large index contrasts are available. Therefore the scalar approcimation are generally not accurate enough. In stead the vectorial effects must be included.

Full vectorial and semi-vectorial solutions

After some mathematical detail, (2.14) may be rewritten to two equations for the x- and y parts of the magnetic field [20]:

$$\frac{\partial^2 H_x}{\partial x^2} + \underbrace{\epsilon\frac{\partial}{\partial y}\left(\frac{1}{\epsilon}\frac{\partial H_x}{\partial y}\right)}_{A} + \frac{\omega^2}{c^2}\epsilon H_x + \underbrace{\frac{1}{\epsilon}\frac{\partial\epsilon}{\partial y}\frac{\partial H_y}{\partial x}}_{B} \;=\; \beta^2 H_x \tag{2.20}$$

$$\frac{\partial^2 H_y}{\partial y^2} + \underbrace{\epsilon \frac{\partial}{\partial x}\left(\frac{1}{\epsilon}\frac{\partial H_y}{\partial x}\right)}_{A} + \frac{\omega^2}{c^2}\epsilon H_y + \underbrace{\frac{1}{\epsilon}\frac{\partial \epsilon}{\partial x}\frac{\partial H_x}{\partial y}}_{B} = \beta^2 H_y \qquad (2.21)$$

The braced terms A and B indicate the changes from the scalar approximation. If the derivative of the index distribution is assumed negligible, the equation reduces to the Helmholtz equation. The term marked B, results in a coupling of the two equations. If this term is neglected, but the term A is kept, the resulting equation is the so-called semi-vectorial wave equation. This equation is significantly more accurate than the scalar wave equation, and this is achieved without any significant increase in computation time, since the number of non-zero elements in the matrix system is not altered. Assembling the matrix system becomes slightly more complicated, since the derivative of the index structure must be calculated.

If both term A and B are kept, the number of rows in the matrix system will double, due to the coupling between the two equations. This will increase computational times significantly, but also result in more accurate results. The results presented in this thesis are all calculated with full vectorial models.

Finite Difference Modelling of Photonic Crystal Fibres

The developed model is very well suited for modelling PCFs. The properties of the cladding region may be modelled by using periodic boundary conditions. The size of the computational domain must, however, be chosen to be a whole number of the lattice constant in the x and y direction. Fibre structures may be investigated by introducing a core and in this case both metallic, periodic boundary conditions, or even more advanced boundary conditions may be used. The model is based on a Cartesian grid, which means that, when using periodic boundary conditions, the size of the unit cell is increased, compared to the unit cell of the PWM. An example of a unit cell and supercell are shown in Fig. 2.7. Both domains are chosen, so that periodic boundary conditions may be used.

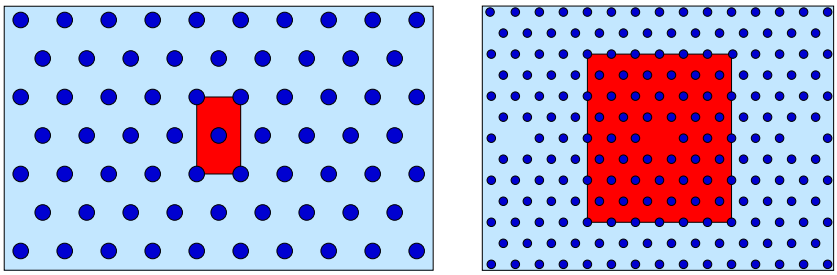

(a) Simple computational cell (b) $4\sqrt{3} \times 6$ super cell

Figure 2.7: *Computational cells for the finite difference model.*

Symmetries in the Structures

The majority of the fibre structures considered has a six-fold symmetry, meaning that the structure is not altered by a rotation of pi/3 radians. Such structures may be oriented, so that it is symmetric around both the x- and y-axis in a Cartesian coordinate system. This symmetry may be used to lower the size of the domain, since it is only necessary to calculate the solutions in one of the four quadrants of the domain.

2.2.4 Structure generation

To efficiently model PCFs it is important to be able to easily generate the complex index structures used. When the index structure has been generated, the discretised index profile and its spacial derivative is used to cast the finite difference equations into matrix form. Typical PCF structures have large discrete steps in the refractive index profile. It turns out that, if care is not taken, discretising such structures may result in significant errors, reducing the accuracy of the model.

To solve these problems, a structure generating program, StructGen, was developed. Using basic geometric building blocks, such as blocks, circles, ellipses and polygons, the program enables fast and easy generation of the complex index structures considered. The problem around the material interfaces are reduced by assigning an average refractive index to

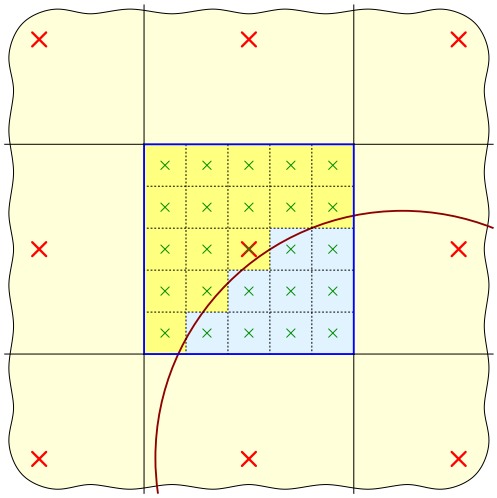

Figure 2.8: *If necessary, the refractive index is averaged, by subdividing the computational cell into a mesh, and then calculating how large a fraction of the cell is inside the considered objects. Red crosses indicate lattice points, while green crosses indicate subgridding points. The red curve shows a section of a rod, which intersects the computational cell.*

points, which are located on the boundary between two materials. Whenever a cell is found, which is partially inside two or more materials, the cell is divided into a $n \times n$ subgrid, and the index in these n^2 points are found. A weighted average is then calculated. The principle is illustrated in Fig. 2.8, where a section of a circle passes through a computational cell. The cell is divided into a 5×5 grid, and the number of points inside the circle is calculated. In the example shown, 9 out of 25 subgridding cells are inside the circle, and this fraction is used to calculate the average index of the cell.

The accuracy of the overall method is improved significantly by introducing the subgridding. In Fig. 2.8, the relative error, as a function of resolution is shown for no subgridding, and for four different subgrid resolutions. The fast oscillations in Fig. 2.9(a) makes it difficult to accurately interpret the curves, even though no subgridding clearly shows worse convergence, compared to doing the subgridding. If a Gaussian filter is applied, to remove the fast oscillations, the tendencies can more

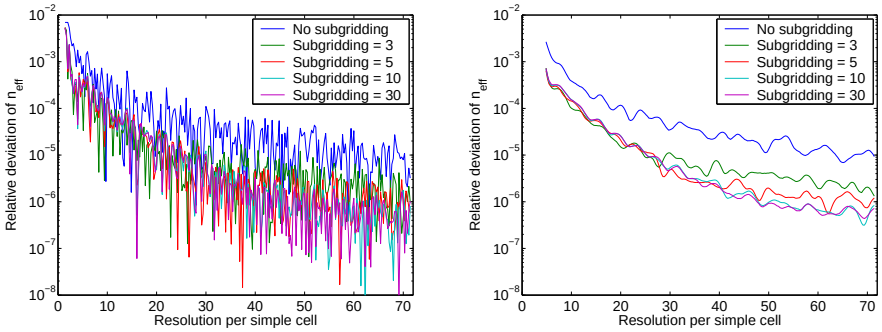

(a) No filtering.

(b) Gaussian filter applied.

Figure 2.9: *Relative error in effective index of an index guiding PCF as a function of the number of points per unit cell for 5 different degrees of subgridding. In (b) a Gaussian filter is applied to the data to remove the fast oscillations.*

easily be seen. No subgridding significantly lowers the accuracy. For resolutions below about 25, a subgridding of only 3×3 is just as good as a larger subgridding. This is because the accuracy is limited by the low resolution. When the resolution is increased, the subgridding start to be the limiting factor, and from a resolution of above 30, a difference can be seen between subgridding values of 3 and 5. For even higher values of the resolution, a difference between subgridding values 5 and 10 can also be seen.

The developed model may be used to create quite complex index structures, and very accurate descriptions of real index distributions. Two examples of so-called air-guiding PBG fibres generated with StructGen are shown in Fig. 2.10. This type of fibre will be described in detail later.

2.2.5 Other methods

The PWM and the finite difference methods have been the most extensively used numerical tools. Other methods have, however, been considered.

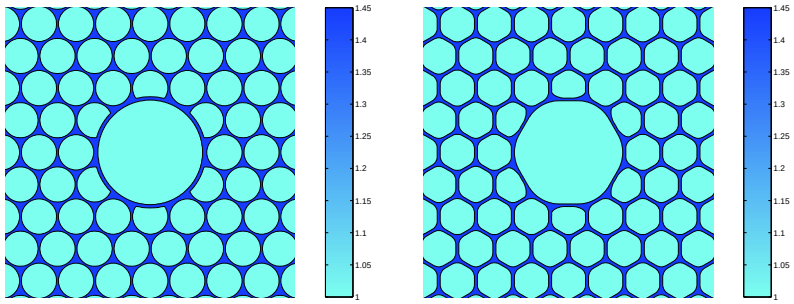

(a) Example of an air-guiding PCF

(b) Example of structure which include various objects with rounded corners.

Figure 2.10: STRUCTGEN *is a tool to design fibre cross-sections, and can be used to generate quite complex index structures.*

One of the drawbacks of the described models is the uniform resolution across the entire calculation domain. A uniform grid spacing makes it difficult to resolve very fine structures in the index distribution. The only options are to either make the domain very small, which leads to coupling between defect states or increase the number of points, resulting in increased memory comsumption and simulation times. Accurate modelling, will in some case rely on accurate description on very fine structures. One example of such a structure is the so-called *cobweb* structure shown in Fig. 2.11. This is a highly non-linear fibre, with a very high index contrast between the core and the cladding. The core is suspended in air by narrow silica bridges. To determine the effective index and non-linear properties of such a fibre, it is necessary resolve the very narrow silica bridges. The most obvious solution is to make a non-uniform grid, with a small grid spacing around the fine structures in the core area, and then a more coarse grid in the outer cladding regions. This may be achieved using the finite difference method, but is not implemented in the current model. The *finite element method* (FEM) is very well suited for problems like this, since the non-uniform grid is an inherent part of the model. FEM methods are being used extensively, also to model wave propagation in PCFs [22].

Many other methods are used, e.g. the multipole method [23], localized

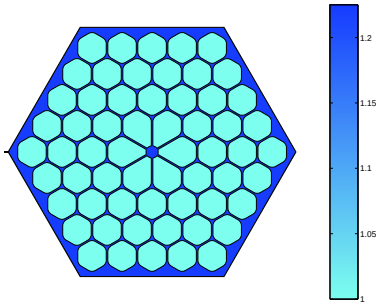

Figure 2.11: *Cobweb PCF. With a design like this it is possible to confine the light very tightly to the core region, because the effective cladding index is very low. To model such structures it is necessary with a high resolution around the very fine structures, which suggests a numerical method with a non-uniform computational grid.*

functions method and many more. These methods have, however, not been studied.

2.3 Index Guiding Photonic Crystal Fibres

As mentioned, omitting a single air hole in the fibre structure may be used to create a core area with a higher refractive index than in the cladding. By calculating the allowed mode in such a structure, some of the fundamental PCF properties are seen. Fig. 2.12 depicts the mode index as a function of normalized frequency, $\frac{\Lambda}{\lambda}$. The constant core index and the wavelength dependant cladding index are also shown. As for COFs, the mode index lies between the core and cladding index. The effective index contrast is large for low frequencies and small for high frequencies. For normalized frequencies above 1.7, the fibre is seen to support a second order mode.

The waveguiding properties of such fibres, do in many ways resemble that of COFs, and it is possible to estimate several properties of PCFs by evaluating the similarities with COFs.

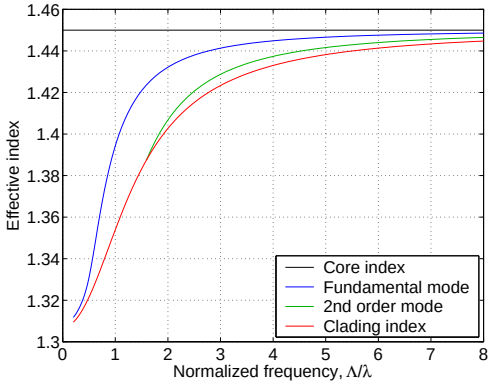

Figure 2.12: *Effective core, cladding and mode indices in a PCF with a triangular cladding structure. Both the mode indices and the cladding index is highly wavelength dependant. For $\Lambda/\lambda > 1.6$ the fibre guides a second order mode.*

2.3.1 Step-index fibre analogy

The effective index considerations above, allow the introduction of a step-index analogy to PCFs. For *step-index fibres* (SIFs) the effective frequency[1] is defined as:

$$V_{\text{eff}} \;=\; k\,a\,\sqrt{n_{co}^2 - n_{cl}^2} \tag{2.22}$$

where k is the wavenumber, a is the radius of the fibre core, and n_{co} and n_{cl} are the core and cladding refractive index. For a SIF these refractive indices are wavelength independent (neglecting material dispersion). A similar parameter for PCFs may be defined by replacing n_{cl} with the effective cladding index, n_{eff} described in the beginning of this chapter. The core radius of a PCF must also be approximated, since no discrete boundary between the core and cladding exist. A typical choice is $a = \Lambda$, but other choices are possible [24, 25].

Fig. 2.13 show V_{eff}, calculated for the same parameters as shown in Fig. 2.2. The effective frequency of a SIF is also shown for comparison.

[1] Often referred to as normalized frequency. Effective frequency is used to avoid confusion with the PCF normalized frequency, Λ/λ.

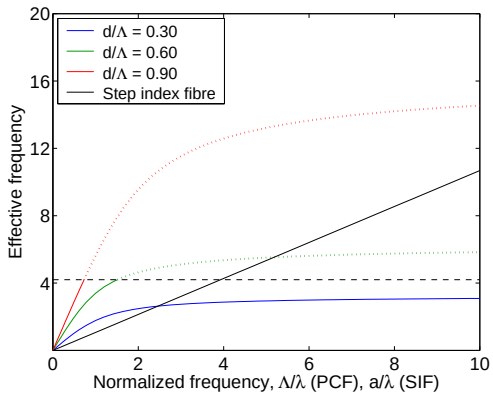

Figure 2.13: *Effective frequency, V_{eff}, of three PCFs as a function of normalized frequency. PCFs become multi-mode at $V_{\text{eff}} = 4.2$. The effective frequency of a SIF is also shown.*

A SIF supports multiple modes when the effective frequency is above 2.405. Since the effective frequency is proportional to the frequency, any SIF design will support multiple modes, for sufficiently large frequencies. PCFs support higher order modes when the effective frequency is above 4.2 (for $a \equiv \Lambda$), as indicated by the dotted part of the curves in Fig. 2.13. However, the effective frequency is no longer proportional to the frequency, due to the wavelength dependant cladding index. For high frequencies, the effective cladding index approaches the core index, and the *numerical aperture* (NA), $\sqrt{n_{co}^2 - n_{\text{eff}}^2}$ therefore approaches 0. As Fig. 2.13 shows, the slope therefore decreases with frequency. It can be shown that for any frequency only a finite number of modes are guided. If the normalized hole size is below approximately 0.45, only a single-mode is guided regardless of the wavelength of the light. This is the case for the blue curve on Fig. 2.13, where $\frac{d}{\Lambda} = 0.30$. Such fibres are known as endlessly single-mode fibres [15], which is a concept unique to PCFs.

As with COFs the effective frequency may be used to describe several important properties. The *mode-field diameter* (MFD) relative to the pitch, is only a function of effective frequency and not hole size or normalized frequency [24]. This is also the case for COFs [26].

The wavelength dependant cladding index may be used to design PCFs

with both very large index contrasts and very small index contrasts, for low and high normalized frequencies respectively[2]. This may be exploited to make fibres with more extreme values of the MFD.

Large mode area fibres

For several applications it is desirable to have as large a MFD as possible. Large MFDs results in low light intensities, and thus low non-linear effects. Generally, the fibres must remain single-mode, which means that if the core size in increased, the NA must be decreased. In conventional fibres, the NA is created by doping the fibre. This sets a lower limit on the NAs obtainable, due to the limited accuracy in doping levels.

Using PCF technology, very low NAs may be obtained. If the pitch is large, compared to the wavelength of the light, the cladding index approaches the core index, and the NA becomes small. This approach results in better control of the index contrast levels. In principle the pitch can be made arbitrarily large. Bend losses will, however, eventually limit the size of the pitch. Single-mode PCFs with mode areas as large as $600\mu m^2$ have been presented [27].

Non-linear fibres

Taken to the other extreme, small values of the pitch results in index contrasts significantly higher than what can be obtained in COFs. A high index contrast means that the mode can be very tightly confined to the core area, thus increasing the light intensity at a given power level. High intensities lead to high non-linear effects. Combined with the superior dispersion tailorability, this makes PCFs an ideal choice for many non-linear applications, such as super continuum generation [28].

[2]Which for a fixed wavelength corresponds to small and large values of the pitch respectively, due to the scale invariance of Maxwell's equations.

2.4 Photonic Bandgap Fibres

The majority of PCFs guide light by MTIR, and these fibres do in many respects resemble COFs. PCFs may also be designed to guide light by a fundamentally different mechanism, known as the PBG effect. In such fibres the photonic crystal cladding has a photonic bandgap, and they are often referred to as *photonic bandgap* (PBG) fibres or PBG guiding fibres. The behaviour of these fibres are very different from COFs.

Photonic bandgaps can be viewed as a optical analogue to electronic bandgaps in semiconductor materials [29]. In semiconductor crystals, the lattice period of the crystal lattice, which is formed by the atomic structure, has a size in the same order of magnitude as the wavelength of the electrons. This results in accurate control of the electron behaviour. In photonic crystals, periodic structures, with a lattice constant close to the the wavelength of the light, has similar implications, allowing for controlling the light propagation, by introducing photonic bandgaps. Photonic bandgaps are frequency intervals where electromagnetic waves cannot propagate regardless of propagating direction. This means that light, in the forbidden frequency region, incident on the PBG material, will be reflected. The PBG effect was first described independently by John and Yablonovitch in 1987 [30, 31], when they studied spontaneous emission control.

The periodicity of photonic crystals may extend into one, two or three dimensions, and are therefore categorised as one-, two-, or three-dimensional photonic crystals. Fig. 2.14 show schematic examples of such crystals. Different colors correspond to materials with different refractive index. The one-dimensional case corresponds to the well known Bragg grating, where wavelengths fulfilling the Bragg condition are reflected.

The cladding in a PBG fibre is a two-dimensional photonic crystal, with invariant index profile in the last dimension. One- and three-dimensional photonic crystals will not be investigated further in this thesis. Details on the properties of photonic crystals may be found in [32].

The PBG effect may be used to confine light. This is achieved by introducing a defect into the lattice crystal, thereby changing the mode

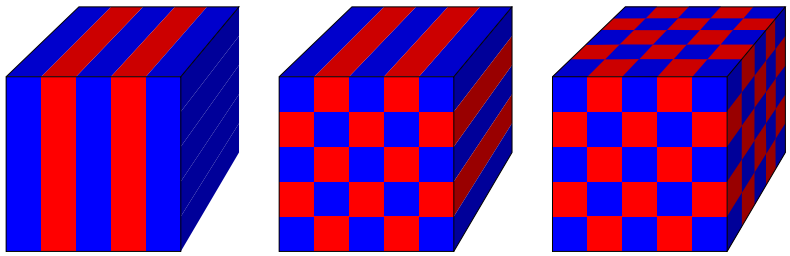

(a) One-dimensional photonic crystal (b) Two-dimensional photonic crystal (c) Three-dimensional photonic crystal

Figure 2.14: *Schematic illustration of one-, two-, and three-dimensional photonic crystals. Figure inspiration from [32].*

solutions in the area around the defect. Modes which are not allowed in the cladding structure may now be allowed around the defect region, from where it cannot escape, since the mode is not allowed in the cladding structure. Alternatively, one can say that all cladding modes have a significantly different mode index, which means that coupling from the core mode to the lossy cladding modes are suppressed.

To describe the PBG effect, the fibre in Fig. 2.15 is used as an example. The cladding consists of air holes arranged in a honeycomb lattice, and the core is formed by adding an extra air hole in the centre of the fibre. An air hole size of $\frac{d}{\Lambda} = 0.25$ is used. The properties of the photonic crystal cladding may be analysed by calculating the allowed modes in the simple unit cell as explained in section 2.2.2. The unit cell of the honeycomb lattice is shown in Fig. 2.15(b).

Using MPB, a large number of modes are calculated for propagation constants with a fixed z-component and in-plane components along the boundary of the irreducible Brillouin-zone. The resulting band diagram is shown in Fig. 2.16(a). A photonic bandgap exist around $\frac{\Lambda}{\lambda} = 2.09$. If a defect is introduced, as indicated in Fig. 2.15(a), the solutions around the core are altered. A mode, with a frequency inside the bandgap, can then be found. The electric power density, $\mathbf{E} \cdot \mathbf{D}$, of the mode is shown in Fig. 2.16(b). The mode is clearly located around the core region, even though the core have a lower refractive index, compared to the cladding. The normalized propagation constant, $\frac{\beta\Lambda}{2\pi}$, is equal to 3.

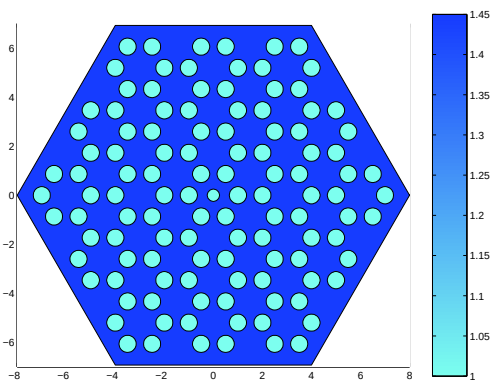

(a) Honeycomb PBG fibre.

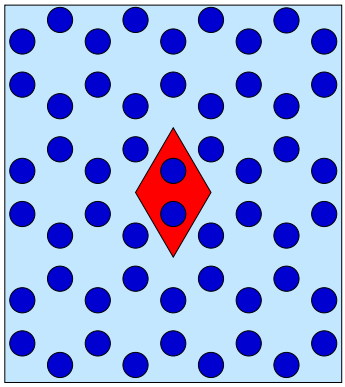

(b) Unit cell of the honeycomb lattice.

Figure 2.15: *Example of a photonic bandgap fibre with a honeycomb photonic crystal cladding (a), and the unit cell for computing the cladding properties (b).*

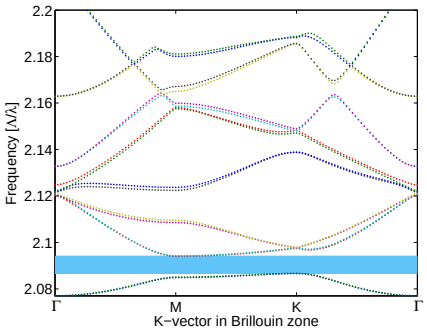

(a) Banddiagram.

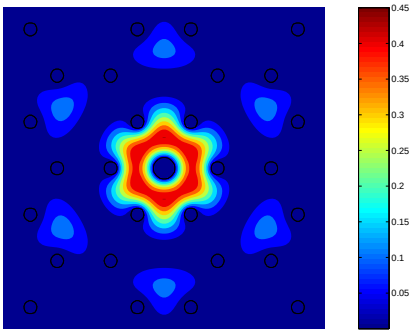

(b) PBG guided mode.

Figure 2.16: *Band diagram, (dispersion relation), of an infinite honeycomb lattice structure, (a). A photonic bandgap centered at* $\frac{\Lambda}{\lambda} = 2.09$ *is indicated by the blue region. A mode confined to the region around a lattice defect can be calculated, (b).*

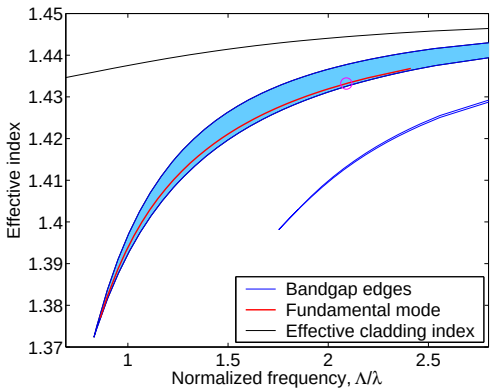

Figure 2.17: *Bandgap plot of honeycomb lattice. The boundaries of the bandgap region is shown as function of the normalized frequency. A guided mode can be seen within the bandgap.*

The position and size of the bandgap region depends on the value of the propagation constant (or equivalently on the frequency or wavelength). By calculating the allowed cladding modes for a range of propagation constants, it is possible to see the development of the photonic bandgap. Fig. 2.17 show the property of both the cladding structure and the guided mode in the fibre structure, as a function of normalized frequency. The black curve shows the effective cladding index, which is equivalent to the cladding index calculated for the index guiding structures. Below the effective cladding index a photonic bandgap opens up when the normalized frequency reaches about 0.8. The bandgap exist in a wide frequency range, and the effective index of the bandgap region increases with wavelength. As indicated by the red line, a guided mode can be found in the bandgap region. The red circle indicates the mode solution plotted in Fig. 2.16(b). The thin blue line below the primary bandgap is a higher order bandgap region. Generally, confined core modes may also be found in such higher order bandgaps, this bandgap is, however, too narrow.

PBG fibres may be used within several areas, such as advanced dispersion applications, sensor applications, tunable filters/attenuators and many more. However, the area receiving the largest interest is air-guiding PBG fibres.

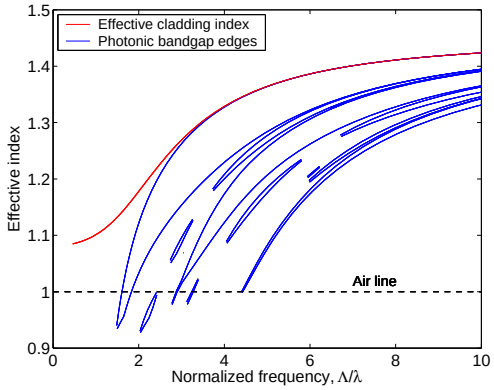

Figure 2.18: *Bandgaps in a triangular cladding structure with* $\frac{d}{\Lambda} = 0.94$. *Some of the bandgaps extends below the air line.*

2.4.1 Air-guiding Photonic Crystal Fibres

Air-guiding fibres allow for confinement of light to a hollow core. As just seen in the previous section, the PBG effect may be used to confine light to a core region, where the index is lower than the effective index of the cladding. To have a confined mode in a core region, the effective index of the mode must be lower than the effective index of the core. This means that to confine light to a low index core, it is necessary to have a bandgap which extends below the refractive index of the core region. Thus to guide light in an air filled core, it is necessary to have a bandgap extending below a refractive index of 1, referred to as the air-line. This can only be achieved with PCFs with high air-filling fractions. At the same time the cladding structure must be highly regular, to effectively avoid excessive losses.

Fig. 2.18 show the bandgap in a triangular cladding structure, with $\frac{d}{\Lambda} = 0.94$, as a function of the normalized frequency. Some of the bandgaps extend well below the air line, and in these areas, it may be possible to have guided modes that have the majority of the light located in the air core.

Air-guiding structures have been investigated intensively. The first realisation of an air-guiding fibre was presented in [33]. This was slightly

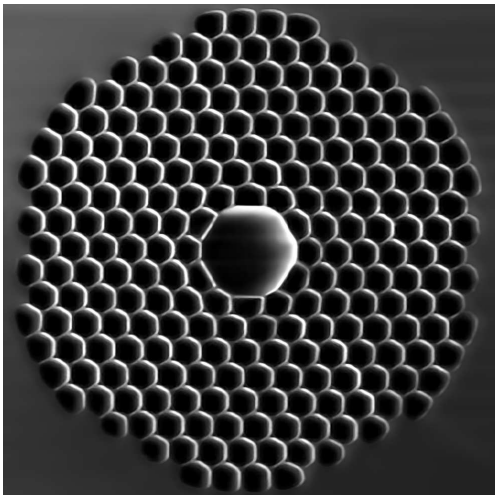

Figure 2.19: *SEM picture an air-guiding PCF with an operating wavelength around* $1\mu m$*. Picture is courtesy of Crystal Fibre A/S.*

before the first theoretical treatment of these waveguides, which was presented in [34]. Since then losses have been brought down, and losses as low as 1.7dB/km have been reported [35]. Results suggest that losses are ultimately limited by micro-deformations on the silica/air interfaces [36], but losses could ultimately be lower than the losses in COFs, since the light is primarily located in air, where effects such as Brillouin scattering may be avoided. An example of an air-guiding fibre, fabricated at Crystal Fibre A/S, is shown in Fig. 2.19.

The "tip" of the fundamental bandgap in Fig. 2.18 extends down to an effective index of about 0.93. It turns out that the fundamental bandgap, which is located between the 4th and 5th band, extends below the air line, for a wide range of hole sizes. To further investigate the demands on the cladding structure, the bandgap properties as a function of hole size is investigated. The bandgaps are calculated for a range of normalized hole sizes between 0.75 and 1. In Fig. 2.20, the lowest effective index of the bandgap, and the normalized frequency at this point, is shown as a function of the normalized hole size.

As the figure shows, the bandgap extends below the air line for normalized

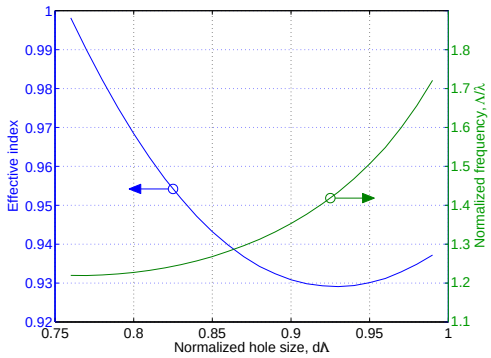

Figure 2.20: *Minimum refractive index of the edge of the bandgap, and the normalized frequency at this point.*

hole sizes above 0.76, corresponding to an air-filling fraction of just above 50%. This means that is is not possible to create an air-guiding fibre in a silica/air structure for air-filling fractions below 50%. To create airguiding structures at lower air-filling fractions, materials with higher refractive index must be used [37]. Higher air-filling fractions also result in a lower index of the bandgap tip, except for very large holes where the index rises again. This happens when the amount of silica material become too small, resulting in a slightly weaker bandgap. The approximate operating frequency is shown on the right axis of the figure. The frequency cannot be chosen freely, since it must be in the region where the bandgap extends below the air line.

The core of an air-guide is typically made by removing a number of the central silica rods. The choice of core structure has some implications, which will be described shortly. The typical core size corresponds to removing the inner 7 rods. The fundamental guided mode calculated in such a structure is shown in Fig. 2.21.

Several results utilising the special properties of air-guiding fibres have been published. In [38] an air-guiding fibre is used to compress ultra short frequency chirped pulses. The hollow core has also been used as a particle guide [39]. Also the confinement of light to an air region, effectively reduces the light intensity in the silica regions. This allows for more power in the fibre and reduces the non-linear effects [40]. This

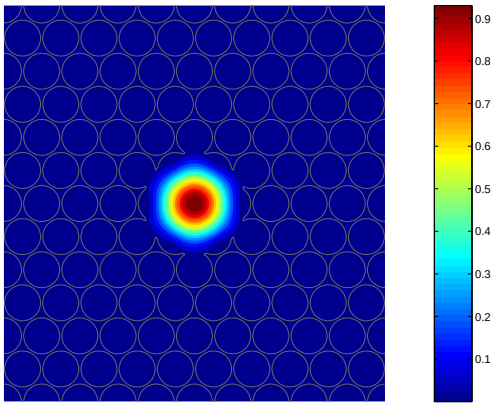

Figure 2.21: *Electric power density of the fundamental mode in an air-guiding PCF with* $\frac{d}{\Lambda} = 0.97$*. The light is effectively confined the the air core.*

concept will be thoroughly described in chapter 5.

Single-mode / multi-mode behaviour

Photonic bandgap fibres may, just like COFs, support higher order modes. For large air holes and large core sizes, the air-guide structure may support a second order mode. The modes must of course be located inside the bandgap. The multi-mode behaviour may be illustrated by calculating the allowed modes within the bandgap for the structure shown in Fig. 2.21. The guided modes within the bandgap region are shown in Fig. 2.22. The fundamental mode consists of two degenerate polarisation states. Just below the fundamental mode four polarisation states form the second order modes. If the core size or the hole size is decreased, the second order mode may cease being guided. The calculated second order mode is shown in Fig. 2.23. (a) shows the field amplitude, and it is seen that the mode resembles the LP_{11} from conventional fibre optics. (b) shows the sum of the electric power density of the four second order modes. The resulting intensity profile is *donut* shaped, with an intensity dip in the centre of the core.

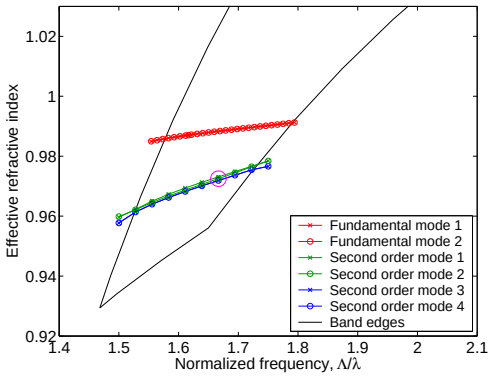

Figure 2.22: *Bandgap and mode index for a multi-mode air-guiding fibre.*

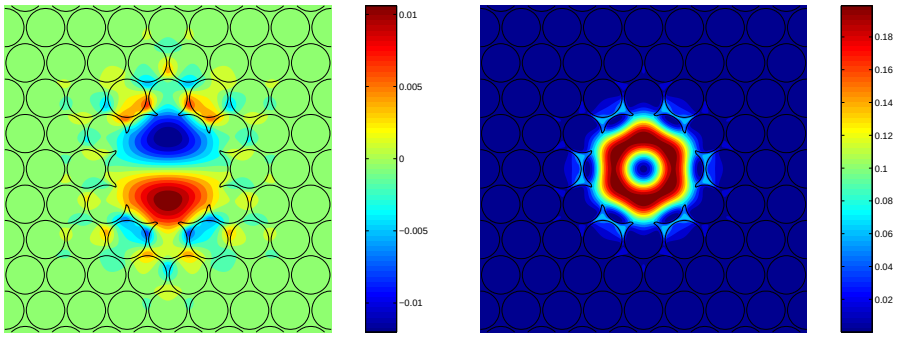

(a) Field distribution. (b) Electric power density.

Figure 2.23: *Field distribution of higher order mode in an air-guiding fibre.*

Surface modes

One of the primary limiting mechanisms of air-guiding PCFs is coupling to surface modes [41–43]. Perturbations in the index structure along the length of the fibre cause coupling from the guided core mode to leaky cladding modes. Perturbations may be caused by many different mechanisms, such as bending, surface roughness, stress or simply axial variations from the fabrication. The degree of coupling is determined by the magnitude of the perturbations and the difference in propagation constant between the considered modes [44].

Surface modes exist on the boundary between the core and the cladding of typical air-guiding PCFs. The field in such modes decay exponentially in both the core and the cladding region [45]. Surface modes arise due to the large perturbation when creating the core. This means that the geometry of the core has a significant influence on the number and localisation of the surface modes. If surface modes crosses the bandgap region, significant peaks in the loss occurs when the surface modes crosses the core modes. Due to avoided crossings the loss peaks are often wide, and the result is that the low loss region defined by the bandgap is divided into smaller low loss sections separated by loss peaks.

In [46] and [47] design guidelines are given on how to avoid surface modes. The creation of the core creates a large perturbation of the lattice. Surface modes may be avoided by carefully choosing a core that does not intersect silica nodes[3]. The field intensity in the silica nodes is high, and thus the perturbation is large. It is this large pertubation that creates the surface modes. In chapter 5, air-guiding PCFs are considered, and the core sizes chosen fulfil this simple criterion.

2.5 Summary of chapter 2

In this chapter a wide range of PCF properties were investigated. The fundamental principle of the PCF and the microstructured cladding structure were presented. Then a brief description of the main theoretical tools

[3]Silica region between three air holes.

used to model PCFs was given, including a description of the developed structure generation program. The two types of PCFs, index guiding and PBG guiding fibres, were presented, and some of the new possibilities with this new type of fibre was described. Finally special focus was made on air-guiding PCFs, where the light is confined to an air core. An important loss mechanism of these fibres are surface modes, and this subject was briefly touched upon.

Chapter 3

Rare Earth Doped Fibre Amplifiers and Lasers

In this chapter optical amplification using *rare-earth* (RE) ions is described. First the fundamental principles and properties of optical fibre amplifiers are presented, followed by a discussion on using *photonic crystal fibres* (PCFs) as active fibres. Finally the development of a numerical model to simulate the behaviour of PCF-based fibre amplifiers is presented.

3.1 Optical Amplification

In this section some of the fundamental principles and properties of *rare-earth doped* (RED) amplifiers and lasers are presented, followed by a description of fibre amplifiers, and double cladding fibre amplifiers. The description will not go into much detail. For further insight on topics such as optical amplifier fundamentals, material properties and applications that are common to traditional fibre amplifiers, the reader is referred to some of the comprehensive textbooks written on the subject [3, 48, 49].

3.1.1 Concepts of Optical Amplification with Rare-Earth-Ions

It is practical to use a specific active ion as an example in the description of the fundamental processes and the amplifier models. In the following *erbium* is used, since most of the original research has been based on this ion, because of emission in the important 3rd telecommunication window.

The fundamental processes involved in optical amplification in RED amplifiers are in principle rather simple. However, the choice of parameters such as RE material, concentration levels and co-dopants is quite complex, since one parameter may influence several of the amplifier characteristics. Here a short description is given on the fundamental processes and how the choice of host, RE and co-dopant materials relates to amplifier performance. Knowledge of these topics is essential for the understanding of amplifier modelling and some of the differences between amplifiers based on conventional fibres and PCFs.

Fundamental processes

Stimulated emission is the foundation of optical amplification. Population inversion is achieved optically through the absorption of pump photons. The number of energy levels involved in the amplification process depends on the active RE ion and on signal and pump wavelengths. Here an erbium doped silica amplifier pumped at 980 nm is used as an example; the energy level diagram for this system is shown in Fig. 3.1. Pump photons lift the erbium ions from the ground state $^4I_{15/2}$ to the intermediate state $^4I_{11/2}$ from which the ions drop down to the metastable state $^4I_{13/2}$ through fast non-radiative processes. When left in the metastable state, the ion can either participate in the amplification process through stimulated emission or drop down to the ground level again through spontaneous emission. The likelihood of having either an absorption or stimulated emission process is related to the wavelength of the photons involved in the process through the transition absorption/emission cross section spectra. Knowledge of these spectra is necessary for prediction of amplifier characteristics with the models described in the end of this chapter.

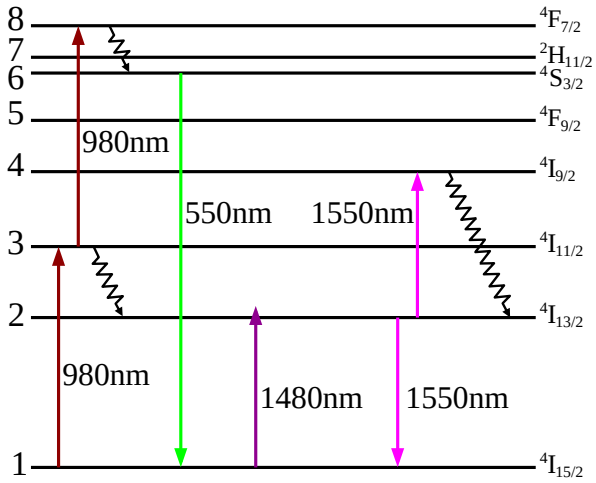

Figure 3.1: *Energy level diagram for Er^{3+} in silica. Arrows indicate transitions of interest to amplifier applications. Arrows pointing down indicate radiative emission, arrows pointing up indicate absorption. The numbers next to the transition arrows show the wavelength of a photon, with the corresponding energy. Black oblique arrows indicate fast non-radiative phonon transitions.*

The procedures used for deriving these spectra have been well described in standard textbooks on the subject, e.g., [48].

Detrimental processes

Processes other than the ones involved directly in the amplification may occur and may cause decreased gain, changed gain saturation characteristics and may in some cases contribute to enhanced amplifier noise. The existence and the significance of the detrimental processes depend on the specific active RE ions, the host material and the co-dopants. The detrimental processes can be divided into three categories; *amplified spontaneous emission* (ASE), *excited state absorption* (ESA), and co-operative energy transfer.

Spontaneously emitted photons are a source of noise in the amplifier.

Even though only a fraction of the spontaneously emitted photons are guided by the fibre, upon their propagation they will stimulate emission from other ions and the result is amplification of the spontaneously emitted photons. ASE occurs both in the forward and the backward direction of the fibre and affects amplifier gain, gain saturation characteristics as well as the amplifier noise figure.

ESA is a process that involves absorption of either a signal or a pump photon by an ion already in the exited state. The ion is lifted to an even higher state and will through non-radiative decays and/or fluorescence return to either the metastable state or the ground level and a pump photon is lost. Using again an *erbium doped fibre amplifier* (EDFA) pumped at 980 nm as an example, pump ESA at this wavelength can occur from the upper pump level $^4I_{11/2}$ to level $^4F_{7/2}$. Non-radiative processes and fluorescence bring the ion back to the ground level again. Because the ion lifetime in level $^4I_{11/2}$ is rather short, ESA, at this particular pump wavelength, only reveals itself in strongly pumped amplifiers [3]. The significance of ESA in various bands can be investigated by comparing the *ground state absorption* (GSA) and ESA transition cross section ratio. Co-dopants and the choice of host material affect the ratio.

Co-operative energy transfer can occur between two neighbouring active ions in the host material and various co-operative processes depending on the particular materials involved can occur. In EDFAs, the effect can reduce the population inversion when an ion in the exited state donates its energy to a neighbouring ion also in the exited state. As a result the acceptor ion is lifted to an even higher energy level $^4I_{9/12}$ from which it decays to the metastable level $^4I_{13/2}$ through non-radiative processes. Co-operative energy transfer is considered to be responsible for the concentration quenching effect found in Er-doped amplifiers particularly for high doping concentrations [50]. Co-doping with aluminium has been found to cause a more even distribution of the RE ions in the host material and, hence, alleviates concentration quenching effects associated with ion clustering.

Spectral broadening effects

RED amplifiers are characterised by several different broadening mechanisms such as lifetime broadening, phonon broadening, stark split broadening and inhomogeneous broadening. The first two broadening effects are well known from other lasers with phonon broadening similar to Doppler broadening and both are so-called homogeneous broadening effects. The energy levels for the active RE ions are split up into several sub levels caused by the external field from the glass host. This splitting is know as stark splitting and causes (in principle) inhomogeneous broadening of the amplifier. However, the stark split broadening can be treated as homogeneous as thermalization keeps sub level populations relative to the manifold population constant due to the small energy gaps between the sub levels [48]. Finally, site-to-site variations in the external field from the glass host cause further inhomogeneous broadening.

Active ions and host materials

EDFAs have received much attention due to their capability to amplify signals in the important third communication window, but several of the other RE elements have also been investigated, and it is possible to obtain amplification in both the visible and the infrared part of the spectrum, depending on the choice of RE ions.

Ytterbium is today attracting attention due to several important characteristics such as broad gain bandwidth and high efficiency, due to a low quantum defect. The low quantum defect means that less power is lost as heat, compared to e.g. erbium based systems, which are typically pumped at 980nm and emits at 1550m. The broad bandwidth makes ytterbium fibres attractive candidates as gain medium in ultrashort pulse lasers and, for example, applications within metrology. Gain bandwidths up to 118 nm have been reported [51], power records are constantly broken, and output powers surpassing the kilowatt limit has been showed [52].

Materials such as ytterbium sensitised praseodymium (output at 635 nm) [53] and ytterbium sensitised thulium (output at 482 nm) [54] have been used to make so-called up-conversion fibre lasers that emits in the

visible part of the spectrum. These lasers are special since they emit light at wavelengths shorter than the wavelength at which they are pumped. This is achieved by using two or more pump photons to pump the active ions to the upper laser level through one or more intermediate levels. Commercial systems are already available and may prove to be future competitors to e.g. frequency doubled solid state lasers. Finally, praseodymium and neodymium-doped amplifiers have been investigated in an attempt to develop amplifiers for amplification in the important second communication window (at 1.31 μm), but so far only moderate gains have been obtained with these amplifiers [49].

3.1.2 Fibre Lasers and Amplifiers

Fibre based amplifiers and lasers posses several desirable features compared to devices based on other technologies, such as semiconductor materials. Some of the favourable properties of RED fibre amplifiers and lasers based on ytterbium or erbium are:

- Excellent beam quality, with M^2 values very close to 1 even for high output powers.
- Easy efficient integration to fibre based optical systems.
- Excellent thermal properties, due to very large surface to volume ratios.
- High gain values.
- Broad gain bandwidths.
- High output powers.
- Wide range of pumping wavelengths can be used.
- Output can be tuned in a broad spectrum.

All these factors show why RED fibre amplifiers are an invaluable component. Improving the performance of such devices, by using PCFs could have a major impact on many areas.

3.1.3 Double Cladding Fibre Structures

One very active research area is high power fibre lasers. High power lasers are used within numerous applications such as micro machining, welding, surgery, marking, and many more. High power laser systems are often large bulky equipment, and not based on optical fibres, because fibre systems have not been able to deliver the power levels needed.

The primary limitation in fibre lasers were previously the coupling of pump power to the core of the fibre. To efficiently couple to the core of the fibre, transverse single-mode sources are needed, making the equipment expensive, difficult to handle, and only relative low powers are available. On the other hand, laser diodes generating many watts of power, operating at 915 nm and 980 nm, which makes them interesting for pumping fibre amplifiers and lasers, are commercially available. Unfortunately, they typically have poor spatial coherence and cannot be coupled efficiently into single-mode fibres.

Double cladding fibres were developed to solve this problem [55]. A double cladding fibre consists of a doped single-mode core surrounded by the inner cladding, and the signal propagates in the doped core. The inner cladding is surrounded by the outer cladding and supports a multi-mode pump field. A schematic of a double cladding fibre is shown in Fig. 3.2. The outer core is typically made of a low index polymer material, resulting in a very high *numerical aperture* (NA) to the inner cladding. This principle enables the use of low-cost high-power multi-mode diode laser arrays, which can be coupled efficiently into the inner cladding due to the high NA and large diameter. Consequently, cladding pumping schemes can reduce the pump count as well as the complexity of the pumping arrangement, due to lower demands on the alignment.

Compared to standard fibre lasers and amplifiers, cladding-pumped fibres need to be significantly longer [56]. This is due to the small core area compared to the inner cladding area. The pump light is gradually absorbed in the doped core region, but the small overlap results in the need for long fibres, to achieve efficient pump absorption. This means that it is important to optimize the overlap between the pump modes and the active core region. Previous results have shown that a circular symme-

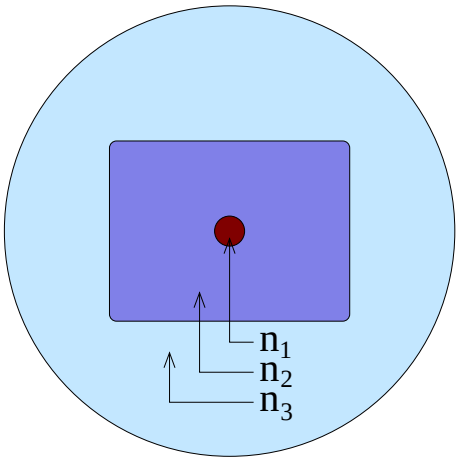

Figure 3.2: *Schematic of a double cladding optical fibre. The fibre has three regions, a core with index n_1, an inner cladding with a smaller refractive index n_2, and an outer cladding with an even lower refractive index n_3.*

try in the fibre results in several modes with very low overlap with the core region. The typical solution is to break the circular symmetry, either in a controlled fashion, or simply by disrupting the shape randomly. One approach is to make the inner cladding much larger in one direction, and then only slightly larger than the core in the other direction, since this also matches the output beam profile of broad stripe laser diodes. Several results have been published on the effects of changing in shape, but the only common conclusion found in literature, is that the circular symmetric cladding is very inefficient [57–59].

Double cladding fibres have resulted in numerous results, with ever increasing output powers. From 110W in 1999 [60], 500 Watts [61], 810 Watts [62] to 1.3 kilowatt [52].

3.2 Active Photonic Crystal Fibres

In this section the use of PCFs as active fibres or fibre lasers is discussed. When introducing a new technology a key issue is to characterise

the differences between the new and the existing technology. Focus will therefore be on the advantages and disadvantages of PCF amplifiers and the novel possibilities which arise. RED PCFs is an active research area. The first results were presented in 1999 [63], and since then many results have been published [64–69], with a focus on double cladding fibres, where PCFs shows great promise.

3.2.1 Fabrication of Active Photonic Crystal Fibres

The use of PCFs as RED fibre amplifiers, creates some new possibilities, due to the way PCFs are manufactured.

Materials

When using PCFs as active fibres, it is necessary to apply the same considerations as for conventional fibres. As PCFs are mostly fabricated in SiO_2 just as conventional fibres, the choices of dopants and co-dopants and, hence, wavelength regimes are the same. Therefore, as described in the previous section, the two choices of erbium and/or ytterbium are the most interesting doping materials. The majority of published results on active PCFs have been based on erbium and/or ytterbium, and the rest of this chapter will also focus on these materials. Other materials could be very interesting, especially when considering alternative host materials such as polymer or soft glasses. However, this will not be considered here.

Co-dopants

As described previously, co-doping of RED amplifiers can alleviate certain detrimental effects and affect emission/absorption transition cross section spectra. Certain co-dopants also raise the refractive index of the glass host, and they have, in fibre amplifiers based on traditional fibres, been used to control the guiding properties of the amplifier. However for PCF amplifiers the raised index caused by co-dopants is often undesirable as the guiding properties of the fibre may be dominated by the raised index

rather than by the microstructure. This will be described in the next section waveguiding properties of PCF amplifiers.

Manufacturing

PCFs are typically manufactured by manually stacking silica rods and tubes into a preform, and then drawing the preform to a fibre [9]. The individual silica rods and tubes are manufactured using the same techniques as for standard fibre preforms [70], such as *modified chemical-vapour deposition* (MCVD), *outside-vapour deposition* (OVD), or *vapour-axial deposition* (VAD) and, as a result, the same options and limitations are valid. This means that several important properties, such as maximum dopant concentration, refractive index regimes, and effects of co-doping are the same for PCFs compared to conventional fibres.

After the deposition process, all the preform fabrication techniques mentioned above require collapsing or sintering of the central part of the preform after the material depositions. This means that the fibres are exposed to high temperatures at three separate stages during fabrication: the vapour deposition, the sintering stage, and the fibre drawing stage. During these stages all of the added dopants diffuse in the glass material. As a consequence, sharp index contrast edges may be softened, and — in RED fibres — some clustering of the RE materials may arise. The majority of the diffusion happens during the preform fabrication, because the preform is heated for an extended period of time compared to the fibre drawing process, where the fibre is only heated for a very short time. Usually the effects of RE ion clustering in fibre amplifiers are negligible. Clustering effects are caused by high doping concentrations, and it is easy to simply lower the doping concentrations in a fibre amplifier, since it only results in the need for a longer fibre. Clustering is therefore primarily an issue in planar optical waveguides where the doping concentrations are much higher, and in fibre lasers where the cavity length is an important parameter.

Since the preform fabrication as well as the fibre drawing processes are similar for PCFs and conventional fibres, it may seem as if there are no differences in which RE doping distributions may be obtained, but this is

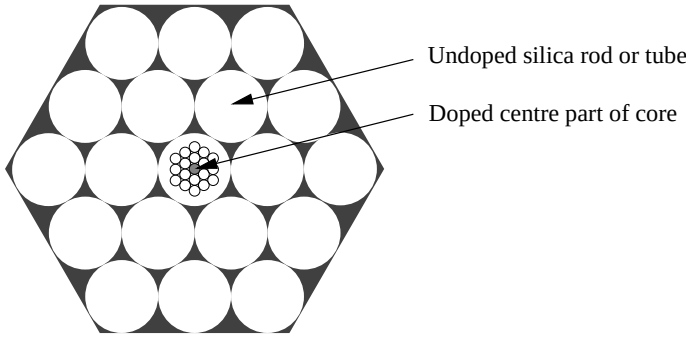

Figure 3.3: *Schematic example of tight confinement of rare-earth-ions in fibre core. The centre silica rod has been replaced by a stack of pre-drawn rods, where only one of the rods is doped.*

not the case. PCFs are just as sensitive to RE ions clustering, but because the PCF preforms are stacked between the sintering and the fibre drawing processing, it is possible to overcome some of the other limitations.

If the RE ions are confined tightly (while still avoiding clustering) to areas with high pump and signal intensities, it is possible to increase the efficiency of the amplifier/laser as will be described in chapter 4. In conventional fibres this is a difficult task since the ions will diffuse during the sintering process, but this may be avoided in PCFs by making a single preform with uniform doping. This rod is then stacked with pure silica rods and drawn to an intermediate stage. The resulting glass rod with a doped centre region is then used as the core in a standard PCF configuration. Such a fibre is illustrated in Fig. 3.3.

With such a super microstructured core, it is also possible to fabricate fibres with very accurately controlled low doping levels. The average doping level of the core is lowered by only making a fraction of the core rods doped. Since there will always be a small absolute uncertainty on the doping level of a particular rod, the doping level is more accurately controlled by, e.g., doping 1/10 of the area with a high concentration of RE ions compared to doping the complete area with a low concentration. This principle has been demonstrated in [67].

Optical systems are becoming more advanced, and this factor increases

the demands on the components. Controlling the doping levels accurately is therefore becoming more and more important. Fibre amplifiers are used to amplify signals in a broad spectral range, and the gain needs to be constant for all wavelengths, i.e. a flat gain curve, or to be accurately controlled in some other configuration. This may be obtained by using several techniques, such as complex pumping schemes, with several pumps at different wavelengths, or — more commonly — by using a gain flattening filter which introduces a wavelength dependent loss that equalises the power in each wavelength.

Such a passive filter will only equalise one specific gain spectrum. It is therefore important to be able to reproduce fabrication phases accurately to maka a fibre amplifier with the required properties.

3.2.2 Waveguiding Properties of Active Photonic Crystal Fibres

A primary advantage of PCFs is the novel waveguiding properties which arise due to several important properties of this technology:

- Increased geometric tailorability
- Higher index contrasts available
- Wavelength dependent cladding refractive index
- Extreme dispersion properties
- Possibility of photonic bandgap guidance

These are also the properties which yield new possibilities for active fibres:

The wavelength dependent cladding refractive index of PCFs allows design of fibres with both very large and very small cores, as described in numerous publications [9]. Small cores make it possible to design very efficient low-power amplifiers/lasers, while large cores make it feasible to design high-power *large-mode area* (LMA) amplifiers/lasers with very

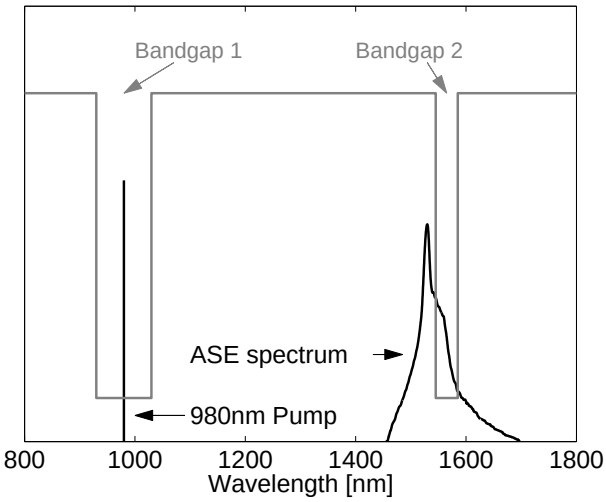

Figure 3.4: *Bandgap guiding PCFs may be used to reduce the amount of ASE in an active fibre. A bandgap is needed at both the pump and signal wavelengths. The narrow bandgap around the signal will reduce the amount of ASE by narrowing the acceptance angle and acting as a spectral filter.*

high damage thresholds. The dispersion properties also increase the possibilities of fine tuning the overlap between the pump mode, the signal mode, and the RE doped regions.

Photonic bandgap guiding fibres may also open up whole new areas within active fibres. Photonic bandgaps may be used to limit the bandwidth of the ASE, thereby decreasing the power lost to noise. For a conventional single cladding fibre, it will be necessary to design a fibre with a bandgap both at the signal and the pump wavelength. If the signal is subsequently located in a relatively narrow bandgap, any part of the spontaneous emission with a wavelength outside the bandgap will not be guided and, consequently, will not be amplified. The angle of acceptance may also be reduced for wavelengths in the bandgap. The principle is illustrated in Fig. 3.4, where the pump is located in the first bandgap and the signal is located in the second bandgap. A significant part of the ASE spectrum is located outside the bandgap and will therefore not be guided.

Air-guiding fibres [33] may be also be used to fabricate novel lasers or amplifiers. This subject will be thoroughly described in chapter 5.

The fundamental waveguiding properties of an undoped PCF is governed by the position and the size of the air holes, and this gives PCFs some unique properties. Doping with RE ions changes the refractive index profile and therefore also the waveguiding properties. Therefore, a raised index caused by co-dopants added for other reasons, e.g. alleviating concentration quenching, must be considered in the design process of a PCF amplifier. The issue has been addressed by several authors [66–68], and guidelines have been presented in [66] through two limiting conditions. The first condition ensures single-mode guidance by imposing a limit on the allowable normalized frequency defined as in [15]:

$$V = \frac{2\pi\rho}{\lambda} NA = \frac{2\pi\rho}{\lambda}\sqrt{(n_{silica} + \Delta n)^2 - n_{cl}^2} < 2.405, \tag{3.1}$$

where ρ is the core radius, n_{cl} is the effective cladding index and Δn is the index increase caused by addition of dopants in the core. The effective refractive index in the cladding can be established using the methods first described in [71], where the cladding index is calculated as the fundamental space filling mode of the perfect cladding structure. The second condition ensures that the guiding properties are dominated by the microstructure and not by the raised index:

$$\Delta n < \frac{n_{silica}^2 - n_{cl}^2}{2n_{silica}} \tag{3.2}$$

One method to ensure this is to add an index lowering co-dopant in the core region. As an example, fluorine was added in the amplifier presented in [68].

This means that accurate control of the doping levels is vital to keep the PCF advantage of improved tailorabilty

3.2.3 Active Double Cladding Photonic Crystal Fibres

As described in chapter 3.1.3, double cladding fibres have made it possible to design fibre lasers and amplifiers with very high output power. Using

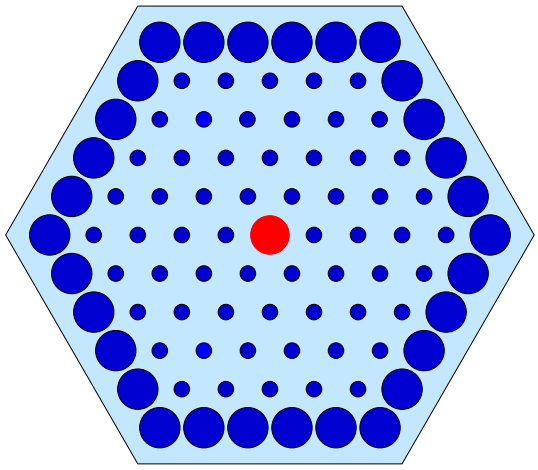

Figure 3.5: *Design of a double cladding PCF, for cladding pumped applications. The outer ring of large holes creates a very large NA, enabling coupling of high power to the inner cladding pump modes. The signal propagates as the fundamental mode in centre defect, which is doped with RE-ions.*

PCFs as double cladding fibres, the improved design flexibility may be used to improve the performance of cladding pumped systems.

The core and the inner cladding of a microstructured fibre amplifier is constructed as a traditional single-mode fibre with a geometry of air holes and a defect in the core region. The inner cladding is surrounded by the outer cladding which have a high air filling fraction, and hence, a low effective index. A schematic of a double cladding PCF is shown in Fig. 3.5.

A fibre design, very close to the one presented in Fig. 3.5 was published in [72]. This design resulted in a fibre laser with a low threshold and high efficiency. Another example of a cladding pumped PCF was presented by Limpert et al. in [68] and is shown in Fig. 3.6. The figure clearly shows how the large air holes in the outer cladding, indicating the very high NA.

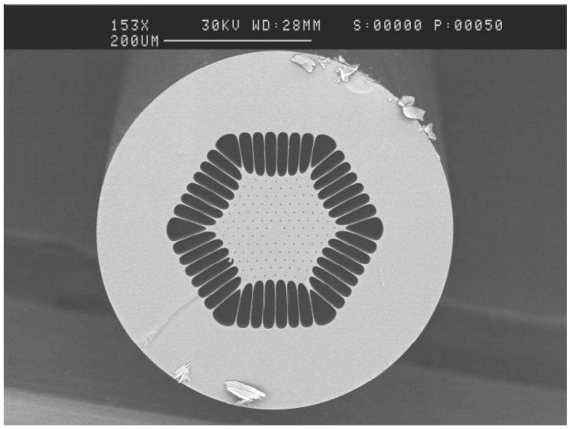

Figure 3.6: *Example of a double cladding PCF laser. Reproduced from [68] with kind permission from Optics Express and Jens Limpert.*

Pump absorption

In a traditional double cladding fibre with a circular inner/outer cladding interface, only a certain fraction of the modes supported by the inner cladding interact with the doped core. As a result, a fraction of the pump power will exist in a gallery of modes that never interact with the core, thereby causing poor pumping efficiency. This has been compensated for using different shapes of the inner/outer core interface whereby a larger fraction of the modes have good overlap with the doped core, see, e.g., [73]. In the case of double cladding PCFs, the problem has not been studied as intensively, since the solutions from conventional double cladding fibres could be adapted. As mentioned in [67] the core position is easily offset relative to the inner cladding, thereby increasing the pump absorption. Very efficient PCF-based lasers have been presented, and slope efficiencies of e.g. 78% was reported in [68].

The main advantages with using PCF-based double clad structures are:

Increased numerical aperture to outer cladding

Very low effective indices can be reached in the outer cladding. If the silica bridges between the air-holes are made sufficiently narrow, the index can approach 1. Such bridge widths would however make the fibres very difficult to cleave and handle. Still effective indices well below 1.3 are easily obtained. As an example a NA of 0.8 was reported in [67], which corresponds to a outer cladding refractive index of 1.2.

Large Mode Area in the Core Region

As described in chapter 2, PCFs may be designed to have very large mode areas. This can be used to lower the intensity of the field, reducing e.g. non-linear effects, and allowing for transmission of more power, since the maximum pulse energy, of a pulsed cladding-pumped fibre laser, is proportional to the effective core area [56]. Typical LMA-designs can be used in double cladding configurations, giving PCF-based fibres an advantage, since the index step can be controlled accurately. For ultra high power applications, one of the key issues is accurate controlling of the index step to the core region [52].

Reduced Size of Inner Cladding

Conventional cladding-pumped fibres are usually fabricated with a polymer outer cladding. This is to achieve as large an NA as possible for the inner cladding, allowing for efficient coupling from high power diode arrays. The polymer cladding is applied during the drawing stage, after the silica has cooled down. This means that the diameter of the fibres during the drawing is equal to the diameter of the inner cladding. As a consequence, cladding-pumped fibres a generally made with very large inner claddings to ensure that the fibre diameter is large enough to avoid breaking during the drawing process [72, 74]. Very large inner claddings result in reduced pump absorption, due to low core/inner cladding area ratios.

With photonic crystal fibres the large NA can be made by the use of large holes in the outer cladding to create a large index contrast. This means that the outer cladding is included in the drawing process, which removes the size restraints on the inner cladding.

However, it should be mentioned, that very often the large inner claddings are desirable, since it allow for efficient pump coupling. Especially for very high pump powers, the large inner cladding is needed. However, for some applications, where efficient pump absorption is desirable, the possibility of creating arbitrary inner claddings could make PCFs the best option.

3.3 Modelling Fibre Amplifiers and Lasers

Since the development of the fibre amplifier, numerous numerical models, for simulating their behaviour, have been developed [3]. Accurate numerical models are an important tool in the development of new technologies, and are generally effective to achieve an understanding of the basic properties of a system, as well as optimizing designs.

The first models of optical amplification were based on a plane wave description of the pump and signal light [75]. Since then more accurate models were developed, in which the optical fields were represented by either an effective overlap with the doped region or an accurate transverse mode description. An accurate transverse modal description is essential for optimisation of waveguide design and dopant distribution. Because of the circular symmetric nature of standard fibres, all previous models are based on circular symmetric mode profiles and circular erbium doped regions. Therefore the models are one dimensional (1D), with a radial description of the field and doping characteristics. The transverse mode description also plays an important role in the description of cladding-pumped fibre amplifiers which are described in section 3.1.3. When modelling photonic crystal fibre amplifiers, the full two dimensional (2D) nature of the mode profiles and the erbium distribution must also be taken into account, if the differences between standard fibres and PCFs are to be examined.

In the remaining part of this chapter, the development of a new two-

dimensional model is presented. This model is based an an existing model, developed by Anders Bjarklev, and described in [3] and [76]. The basic properties of the model is presented and the numerical approach is described, followed by a small description of the developed model.

3.3.1 Designing Amplifier Models

All previous models originate from the same basic first-order rate equations, defining the interaction between the light and the dopants, but several approaches of varying complexity have been made.

The behaviour of many physical properties must be described numerically. The possible approaches and previous choices made in published models, are listed in [3]. Trade offs between complexity, speed and accurate modelling must be made for several of the amplifier/laser properties:

Broadening of the energy levels. Typically, amplifier models neglect in-homogeneous broadening of the energy levels, by assuming that homogeneous broadening is greatly dominant. Results on modelling in-homogeneous broadening effects have been published [77]. The model developed during this project, do not take in-homogeneous broadening effects into account.

Time varying effects versus steady state solutions. Again the simple approach is the dominant. Most model approaches have been on steady state solutions. The time varying effects have been shown to be negligible for most applications, due to the slow gain dynamics in rare-earth-doped fibre amplifiers. This is caused by the very long lifetimes in the metastable state.

Description of ASE. To obtain an accurate description of the amplifier noise properties and gain saturation effects, the spectral dependence of ASE must be included [3]. The first to describe the spectral dependence of ASE was Desurvire in 1989 [78]. Several models have replaced the ASE by an equivalent noise bandwidth. This simplifies the numerical problem considerably, thereby saving computational time, but also reduces the accuracy. The model developed in this

thesis includes the spectral properties of ASE by representing the ASE as a number of spectral components.

Transverse mode description. This is the primary reason to develop a new numerical model, since a full two-dimensional description of the mode shapes was needed. Any number of distinct pump and signal modes may be used, and any number of ASE spectral components, each with arbitrary mode profiles may be defined.

The determination of cross section was briefly described in chapter 3.1. The cross sections are given as input parameters to the developed model, therefore the accuracy of the cross sections and which models/theories are used to obtain them, is unrelated to the accuracy and general design of of the model.

3.3.2 Numerical Approach and Rate Equations

Now the equations for the steady state local inversion factor, i.e. the populations in the ground state, n_1, and excited state, n_2, are derived.

For a two level system, the steady state population can be written directly in terms of the total dopant density, ρ, and the rates, R, at which excitation and de-excitation occurs:

$$n_1 = \rho \frac{R_e + A_e}{R_a + R_e + A_e} \tag{3.3}$$

$$n_2 = \rho \frac{R_a}{R_a + R_e + A_e} \tag{3.4}$$

Where R_e is the rate of stimulated emission, R_a is the rate of stimulated absorption, and A_e is the spontaneous emission rate. Generally, throughout this thesis, subscripts p and s will correspond to pump and signal specific values respectively, while subscripts a and e, correspond to absorption and emission values, respectively. Only (3.3) or (3.4) needs to be solved, since they are coupled through the simple relation of particle conservation:

$$\rho = n_1 + n_2 \tag{3.5}$$

(3.3) and (3.4) does not take cooperative up-conversion, discussed in chapter 3.1, into account. As described, significant up-conversion only occurs for very high erbium concentrations, and can be neglected for typical dopant concentrations used in fibre amplifiers.

The rates, R, at a given point can be expressed as photon intensity times the corresponding cross section. Since photons of different frequency are present, an integration over all frequencies is necessary:

$$R_a = \int_0^\infty \sigma_a(\nu)\frac{I_S(\nu)}{h\nu}\mathrm{d}\nu \tag{3.6}$$

$$R_e = \int_0^\infty \sigma_e(\nu)\frac{I_S(\nu)}{h\nu}\mathrm{d}\nu \tag{3.7}$$

Where σ_e is the emission cross section, σ_a is the absorption cross section, ν is the frequency of the light and h is Planck's constant. $I_S(\nu)$ is the total spectral power density at the frequency ν, counting all pumps, signals and ASE contributions. By separating the pump, signal, and ASE contributions the rates can be written as:

$$R_a = R_{pa} + R_{sa} + R_{aa} \tag{3.8}$$

$$R_e = R_{pe} + R_{se} + R_{ae} \tag{3.9}$$

where the three right hand terms in each equation correspond to pump, signal and ASE induced absorption and emission, respectively. These terms can be calculated as:

$$R_{pa} = \sum_n \sigma_a(\nu_{p,n})P_{p,n}|E^2_{p,n}|\frac{1}{h\nu_{p,n}} \tag{3.10}$$

$$R_{sa} = \sum_m \sigma_a(\nu_{s,m})P_{s,m}|E^2_{s,m}|\frac{1}{h\nu_{s,m}} \tag{3.11}$$

$$R_{aa} = \int_0^\infty \sigma_a(\nu)S_{ASE}|E_\nu|^2\frac{1}{h\nu}\mathrm{d}\nu \tag{3.12}$$

$$R_{pe} = \sum_n \sigma_e(\nu_{p,n})P_{p,n}|E^2_{p,n}|\frac{1}{h\nu_{p,n}} \tag{3.13}$$

$$R_{se} = \sum_m \sigma_e(\nu_{s,m})P_{s,m}|E^2_{s,m}|\frac{1}{h\nu_{s,m}} \tag{3.14}$$

$$R_{ae} = \int_0^\infty \sigma_e(\nu)S_{ASE}|E_\nu|^2\frac{1}{h\nu}\mathrm{d}\nu \tag{3.15}$$

The notation $P_{s,m}$ indicate power for the signal mode no. m. The summation n is a sum over all pump modes present in the fibre in both directions, and the summation m is equivalently a sum over all signals. S_{ASE} corresponds to both the backward and forward travelling ASE power spectral density. P is the power in the considered mode and E is the normalized mode profile intensity, normalized according to:

$$\int_{-\infty}^{\infty} |E(x,y)|^2 \mathrm{d}x\mathrm{d}y \;=\; 1 \tag{3.16}$$

With these equations, the local inversion factor can be calculated. Note that the dopant density, ρ, and the normalized mode intensity, E, generally depend on the position in the fibre cross section. When (3.12) and (3.15) is represented numerically the continuous range of frequencies will be represented by a number of spectral components. Equations (3.10) to (3.15) will then be almost identical, illustrating the similarity of the numerical treatment of pump, signal and ASE contributions. The six equations simply calculate the number of transitions that occur.

The absorption and emission of power by the dopants, change the power in the pumps, signals and ASE modes propagating in the fibre. The differential equations defining the propagation of the light will now be derived:

First the emission and absorption factors are defined:

$$\gamma_e(\nu,z) \;=\; \sigma_e(\nu) \int_0^{2\pi}\int_0^{\infty} n_2(r,\phi,z)\; |E(r,\phi)|^2 \; r \; \mathrm{d}r\mathrm{d}\phi \tag{3.17}$$

$$\gamma_a(\nu,z) \;=\; \sigma_a(\nu) \int_0^{2\pi}\int_0^{\infty} n_1(r,\phi,z)\; |E(r,\phi)|^2 \; r \; \mathrm{d}r\mathrm{d}\phi \tag{3.18}$$

Where, again, E is the electrical field, normalized according to (3.16). These factors indicate the how likely an absorption and emission are to occur. The change in signal can then for each signal mode be expressed as:

$$\frac{\mathrm{d}P_s(z)}{\mathrm{d}z} \;=\; (\gamma_e(\nu_s,z) - \gamma_a(\nu_s,z) - \alpha(\nu_s))P_s(z) \tag{3.19}$$

Where α is the background loss attenuation coefficient. The change in forward and backward propagating ASE can be written as:

$$\frac{\mathrm{d}S^+_{ASE}(z)}{\mathrm{d}z} \;=\; 2h\nu\gamma_e + (\gamma_e(\nu,z) - \gamma_a(\nu,z) - \alpha(\nu))S^+_{ASE}(z) \tag{3.20}$$

$$\frac{\mathrm{d}S^{-}_{ASE}(z)}{\mathrm{d}z} = -2h\nu\gamma_e - (\gamma_e(\nu,z) - \gamma_a(\nu,z) - \alpha(\nu))S^{-}_{ASE}(z) \quad (3.21)$$

The extra term in the ASE equations, compared to (3.19), relates to the spontaneous emission, which add power to the ASE. Finally, the pump mode propagation can be written as:

$$\frac{\mathrm{d}P_p(z)}{\mathrm{d}z} = \mathcal{F}(\gamma_e(\nu_p,z) - \gamma_a(\nu_p,z) - \alpha(\nu_p))P_s(z) \quad (3.22)$$

The coefficient $\mathcal{F}$ distinguishes between pump modes propagating in the forward direction ($\mathcal{F} = 1$) and in the backward direction ($\mathcal{F} = -1$).

The effects of ESA is neglected in (3.22). Significant ESA occurs when pumping in the 800nm pump band, but today 980nm and 1480nm pumps are used almost exclusively, and it is therefore not included in the model. If ESA, for the 980nm pump scheme, was to be considered, the model should be expanded to account for the population in more than two levels. The two-level system considered here, would not be able to account for ESA from the $^4\mathrm{I}_{11/2}$ level, since this state is assumed to be depopulated because of the fast transition to the $^4\mathrm{I}_{13/2}$ level. (See Fig. 3.1 on page 37).

The derivation of these equations is based on an EDFA, but this model could easily be applied to amplifiers using other dopants. The only limitation is that only two non-empty levels are considered. If more levels are included (as with 980nm pumping) the population in these levels must be zero. The empty levels result in a simplification of the differential equations for the power distribution, since some of the cross sections will be zero. For instance when considering 980nm pumping, the emission cross section for the pump (σ_e) is zero, and (3.13) vanish. This illustrates that the $^4\mathrm{I}_{11/2}$ state is completely depopulated.

3.3.3 Model Development

The mathematical differences between 1D models (based on the effective overlap), 2D models (based on circular symmetry), and this model, which is based on arbitrary two-dimensional variations, are not significant. All

equations presented in the previous section can be applied to take cross-sectional variations in optical field and dopant distribution into account. The local inversion, (3.3) and (3.4), must be solved in all points within the considered two-dimensional area. This is done by evaluating (3.10) to (3.15) for all these points. Only points containing rare-earth ions need to be considered, the remaining points may be skipped, as long as the background attenuation is taken into account.

When the inversion is known, the change in power for all modes can be calculated, using (3.19) to (3.22). Since both forward propagating and backward propagating powers exist, the problem constitutes a two-point boundary value problem for which established so-called relaxation and shooting methods exist. Experience gained in the analysis of traditional index guiding fibre amplifiers show that it can be hard to reach convergence with the shooting method and the relaxation method is usually preferred [48]. Insight into the methods used for solving two-point boundary value problems are referred to [79].

The relaxation method is also used here. The problem is solved by first integrating all forward propagating powers in he forward direction. The results obtained are used as values of the forward propagating powers, while the backward integration is performed. Integration of powers is only done in their respective direction of propagation, to avoid divergence [3]. If powers are integrated in the direction opposite of propagation, wrong start values may lead to divergence, i.e. infinite pump values, and breakdown of the model.

To further avoid instability of the algorithm, the inversion factor in iteration no. n, is calculated as a weighted average of the results obtained using (3.3) and the inversion calculated in iteration n-1. If this is not done, the method may result in an oscillation around the solution, and no convergence.

When the solution is found, the gain and noise characteristics of the amplifier can be calculated. For this the *signal-to-noise ratio* (SNR) for an infinitesimal bandwidth is calculated. The noise figure of the amplifier is defined as the SNR at the input divided by the SNR at the output. The SNR will inevitably deteriorate when the signal is amplified in an EDFA,

because of the stochastic nature of the light/matter interaction [3]. The noise figure can be expressed as a function of the forward propagating ASE signal and the gain as:

$$F = \frac{1}{G}\left(\frac{S^{+}_{ASE}(\nu_s, L)}{\mathrm{h}\nu} + 1\right) \tag{3.23}$$

3.4 Summary of Chapter 3

In this chapter the concepts of optical amplification with RE-ions and the possibility of using double cladding fibres have been presented. The advantages of PCF-based lasers and the new possibilities obtained have also been investigated. Finally the development of a numerical model to simulate the behaviour of PCF-based lasers and amplifiers was described.

Chapter 4

High Efficiency Fibre Amplifiers

In the previous chapter the advantages and disadvantages of using *photonic crystal fibres* (PCFs) as amplifiers and lasers were discussed. One of the advantages is the possibility of very large index contrasts, which can be used to obtain very small effective areas. This chapter describes how this can be used to design highly efficient optical fibre amplifiers, which can be operated at very low pump powers.

As optical networks evolve from point-to-point nature into more advanced network topologies, the need for small-scale optical amplification will increase. Cheap and efficient optical amplifiers with a moderate gain may be used for splitting of signals and/or design of transparent components for optical signal processing. If components are often added or removed from the network, it will be desirable to have components which are transparent to the rest of the network, which means that a component must include a way to compensate for the loss caused by its primary function. Such devices may be created using *rare-earth* (RE) doped PCF-based amplifiers operated at very low pump powers. This is achieved by using PCFs with large air holes and thereby large index contrasts. With these high index contrast fibres, it is possible to obtain very small *mode-field diameters* (MFDs) [80]. This allows for the design of low pump

power fibre amplifiers. Since these amplifiers are meant as telecommunication components, and therefore should work at typical telecommunication wavelengths, the RE material used is erbium.

4.1 Modelling of photonic crystal fibre amplifiers

The results presented in this chapter are based on numerical investigations. First the electromagnetic field distributions in the PCFs are calculated. This can be done using any of the methods described in chapter 2.2. In this case the freely available program *MIT Photonic Bands* (MPB) is used [19]. MPB is based on a full vectorial plane wave expansion method [18], and delivers excellent results. The calculated 2-dimensional field distributions are then used as input to the amplifier calculations. In these calculations a Runge Kutta method is applied to find a steady state solution to the population rate equations presented in chapter 3.3.

4.2 Design considerations

The fibres considered have a simple design. The cladding consists of pure silica with air holes arranged in a triangular pattern, see Fig. 4.1. The core is formed by removing a single air hole, (see the inset in Fig. 4.3). The refractive index of the core is therefore higher than the surrounding cladding, and the fibre is thus index-guiding. As in the previous chapters, the parameters Λ and d are used as the pitch and the hole size of the PCF.

The silica rod in the core (or part of it) may have a raised refractive index due to the presence of erbium ions. The diameter of the doped region is denoted d. In all the calculations performed in this chapter, the fibre loss is neglected. This is done to isolate the influence of the considered parameters, and are in general a valid simplification, since the majority of designs considered are with very short lengths of fibre. The concentration of erbium in the core of the fibre is kept at a constant value of $3{\cdot}10^{25}$ m^{-3}. This value is chosen to be a realistic choice for a high doping level. Since

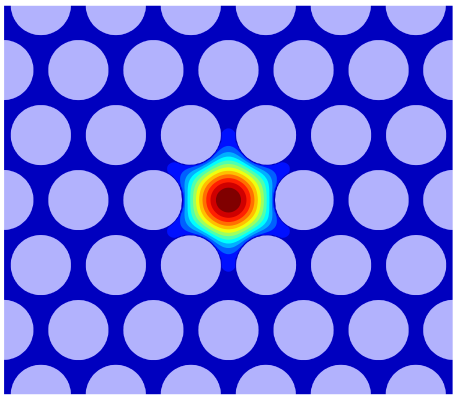

Figure 4.1: *Cross section of the considered fibres. The fibres have a conventional triangular hole arrangement with a single rod removed in the core. The mode profile of a fundamental mode is superimposed on the structure.*

fibre loss is neglected, a change in erbium concentration can be cancelled out by simply changing the length of the fibre, as to keep the total number of erbium ions in the fibre constant. In all calculations a pump wavelength of 980 nm and a signal wavelength of 1550 nm are used. The refractive index of silica is set to 1.451 at the pump wavelength and to 1.444 at the signal wavelength. The index changes resulting from the erbium doping are not varied with the wavelength. The specific erbium absorption and emission cross sections used in these calculations may be found in [76].

4.2.1 Definition of optimisation parameter

To describe the amplifier performance a new parameter is defined: For a given fibre design, the minimum pump power, P_{min}, which results in a predefined target gain value, (typically chosen to be 15 dB) is found. This is done by varying the length of the fibre, each time finding the pump power, which results in the specific target gain. This is then carried out for a range of fibre designs and varying target gains. This parameter is based on the need for small scale amplification in metro networks, where it is necessary to compensate for the loss in a single component.

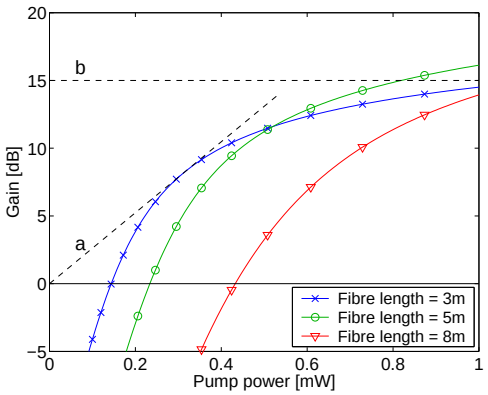

Figure 4.2: *The fibre amplifiers are designed to be able to deliver a predefined gain with as little pump power as possible (15dB in the figure), illustrated by the curve b. Other typical parameters used to describe fibre amplifiers include the gain divided by the pump power, which is the slope of the curve labelled a.*

The definition of this parameter is illustrated in Fig. 4.2. Of the three fibres shown, the best fibre length with respect to the newly defined parameter is 5 meter, (green curve). This parameter corresponds to optimizing the gain coefficient (gain divided by pump power, as indicated with the dashed line a), at a fixed gain value. (A better solution, than the one shown, could be found for an other value of the fibre length). Notice that it is the small signal gain that is calculated. If the signal power becomes large, more pump power would be needed to prevent gain saturation.

4.3 Simulations of high efficiency amplifiers

Simulations are performed to find the minimum pump power needed to obtain a specific gain for a range of PCF and *step-index fibre* (SIF) designs.

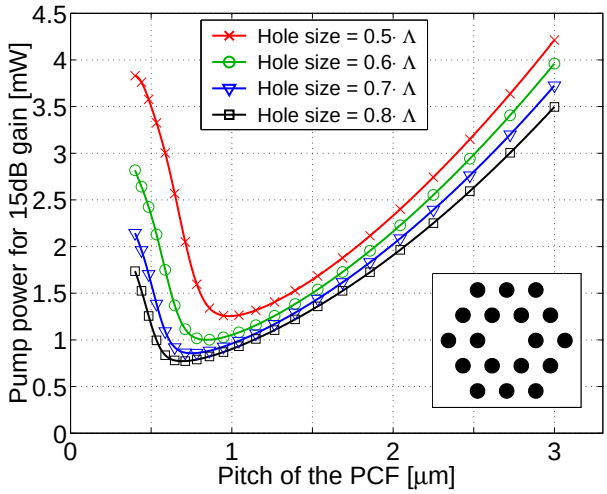

Figure 4.3: *Minimum pump power to achieve 15 dB gain in a PCF amplifier as a function of the pitch for four values of the hole size.*

4.3.1 Optimizing for a constant target gain of 15dB

In Fig. 4.3 the minimum pump power to achieve 15 dB gain in a doped PCF as a function of the pitch is shown for several values of the relative hole size. The dope diameter d is 0.5Λ in this case, which means that only the central part of the silica core rod is doped, and the resulting refractive index change, Δn, in this section is 0.01.

As could be expected, large air holes result in low pump powers. This is a result of the larger index contrast which allows tighter confinement of the pump and signal light. The minimum pump value depends strongly on the pitch of the fibre. For large pitches the core size as well as the MFD increases. This results in the need for more pump power because the pump light intensity drops when the MFD increases. For small pitches the pump value also increases. This is caused by an increase in the signal MFD. When the structure becomes too small, the signal light can no longer be confined to the very small core, and the light spreads out into the cladding. For a normalized hole size of 0.8 we see that the minimum pump power to achieve 15 dB gain is only 0.69 mW. This results in a fibre with a length of 6 meters.

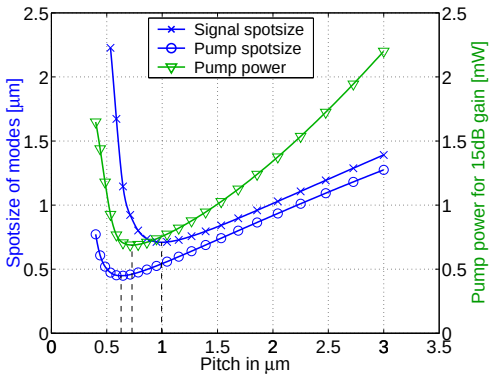

Figure 4.4: *The spot size of the pump and the signal in a PCF amplifier with* $\frac{d}{\Lambda} = .8$ *as a function of the pitch, (left axis) and the needed pump power to reach a gain of 15dB (right axis).*

In Fig. 4.4, the explained spot size variations are shown. It is seen that the pitch resulting in the lowest pump power is located between the pitch values resulting in minimum spot size for the pump and signal respectively. If the pitch is reduces to much, the light very abruptly starts to spread out again. The spot size of the pump is lower than the signal wavelength, due to the significantly lower wavelength.

To compare these PCF values with what can be obtained with standard fibre technology, the same minimum pump value is calculated for step-index fibres. In Fig. 4.5 the minimum pump value is shown for varying core radius and three different refractive index steps. For a large index contrast of 0.03, the minimum pump value to achieve 15 dB gain is 3.5mW, which is five times larger than in the PCF case. The improved performance of the PCFs is a result of two important properties: With PCFs it is possible to obtain much larger index contrasts and, thus, smaller MFDs. This means that a given intensity may be reached at a lower optical power level.

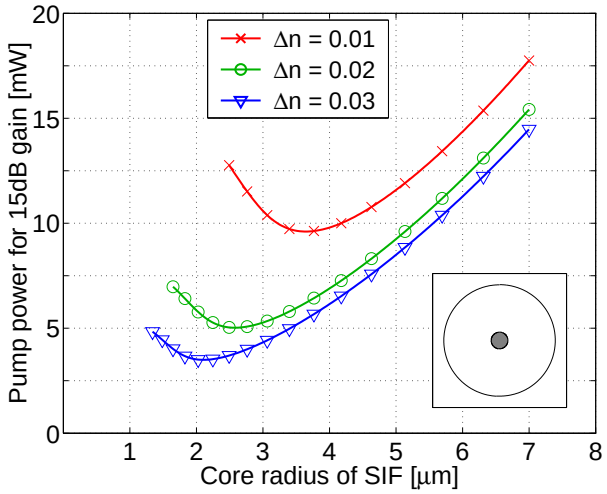

Figure 4.5: *Minimum pump power to achieve 15 dB gain in a SIF as a function of the core size for three values of the refractive index step.*

4.3.2 Size of doped area

The area of the doped region, should also be considered in order to effectively minimize the pump power. If the dope diameter is reduced, the RE-ions are concentrated in regions with higher pump and signal intensity, thus increasing the interactions, and lowering the demands of pump power. The price is a longer fibre, since the area of doping is reduced, reducing the gain per length of fibre. This principle have been used since the invention of the optical fibre amplifier [81], and it may also be used to improve PCF bases amplifiers. The dope radius dependency is shown in Fig. 4.6, for three different dope radii. Fig. 4.6(a) shows the needed pump as function of pitch, and Fig. 4.6(b) show the resulting fibre length. Confining the erbium-ions within a radius of 0.5Λ results in significantly reduced pump powers, but also results in a 6 metres long fibre, compared to 2 metres at a dope diameter of 1Λ. A further reduction of the dope diameter only results in a minor reduction in needed pump power, because the erbium-ions are already confined to an area where the pump and signal field intensity is relatively constant. It does however, increase the length of the fibre, which is increased to 10.5 metres. As the figure

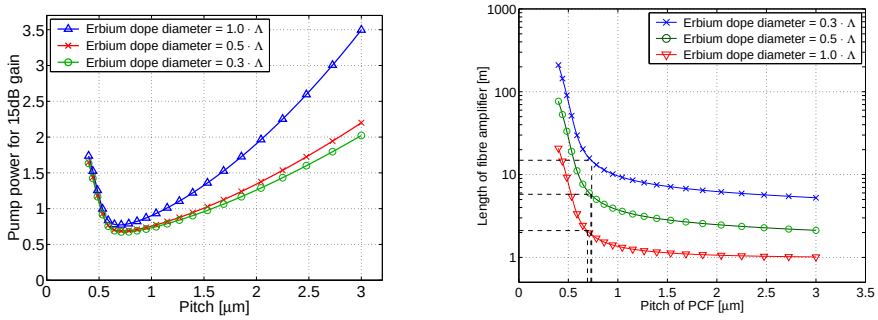

(a) Pump power needed for three values of the dope diameter.

(b) Length of the fibre amplifier needed to obtain 15dB gain

Figure 4.6: *Effects of varying the dope diameter on the pump power and fibre length needed to obtain a gain of 15dB as a function of the pitch.*

shows, the reduction in dope radius is mainly important in larger structures, as the difference between the curves decreases for smaller values of the pitch. Reducing the dope diameter is also feasible in conventional fibres, by using another material, like germanium, to increase the core index in the undoped core region.

4.3.3 Refractive index changes

One of the advantages of using PCFs is that the waveguiding properties are controlled by the holes and not the doping. This means that refractive index changes caused by the RE-doping, does not have a significant influence on the confinement of the modes.

This is illustrated in Fig. 4.7. Again the minimum pump power as a function of pitch is shown, for two dope radii, and three values of the index step to the RE-doped regions, $\Delta n = 0.1$, $\Delta n = 0.2$, and $\Delta n = 0.3$. Increasing the index step only marginally decreases the pump power, since the index step is small compared to the effective index step to the core region. For a step index fibre, doped in the entire core region, the index step has a vital influence, as shown in Fig. 4.5. Since the doping does not change amplifier performance in PCF amplifiers, co-doping may be

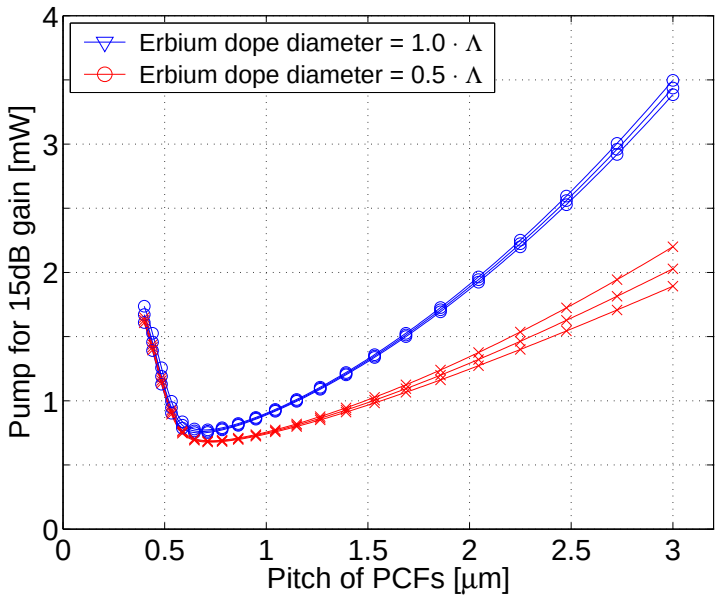

Figure 4.7: *Effects of changing the refractive index in the doped region. Minimum pump power as a function of pitch, for two different doping radii and an index step in the doped region of* $\Delta n = 0.1$, $\Delta n = 0.2$, *and* $\Delta n = 0.3$. *Lower curves correspond to a high index step.*

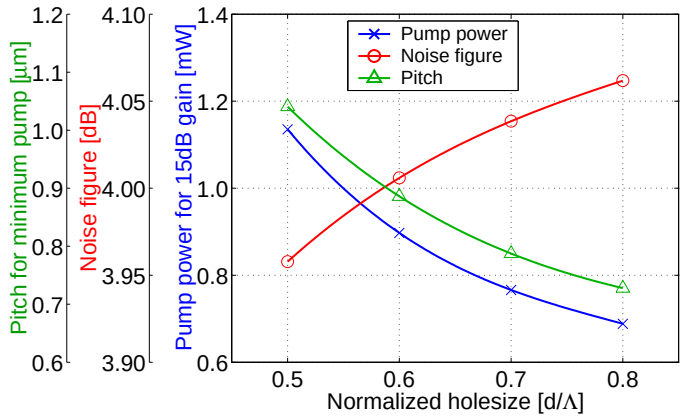

Figure 4.8: *Optimum pitch, noise figure, and minimum pump power to obtain 15 dB gain in a PCF as functions of the relative hole size.*

used to influence other aspects of the amplifier, like dispersion.

4.3.4 Amplifier parameters for varying hole sizes

Using the acquired data from the four minimums in Fig. 4.3, a further investigation of the PCF amplifier performance is performed. In Fig. 4.8 the minimum pump, the noise figure, and the optimum pitch are shown as functions of hole size. Again it is clearly seen that for large holes, the necessary pump power decreases. For a hole size of 0.5 the minimum pump power is 1.13 mW, compared to 0.69 mW at 0.8. Larger hole sizes also result in the structure being scaled down due to the increased index contrast. The variations does not have any significant effect on the noise figure, which only increases about 0.1 dB from 3.96 dB to 4.07 dB, indicating a mediocre noise level for the amplifier. This noise level is also about 4 dB in the SIF amplifier.

4.3.5 Varying the target gain value

Finally the target gain is varied. The results are shown in Fig. 4.9. Again the minimum pump power, the noise figure, and the optimum pitch are

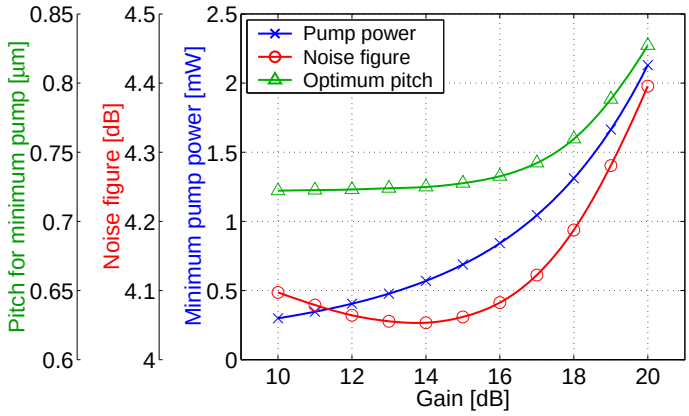

Figure 4.9: *Optimum pitch, noise figure, and minimum pump power in a PCF with relative hole size of 0.8, as functions of the target gain.*

shown, this time as functions of the target gain. The values are calculated for a PCF with a relative hole size of 0.8 and a doped radius of 0.5. The minimum pump value naturally increases with the target gain. 10 dB gain may be obtained with less than 0.3 mW of optical pump power. The noise figure increases slightly for larger gains from about 4 dB to 4.5 dB. An interesting point is that the optimum pitch is almost constant for gains between 10 dB and 16 dB, indicating that by choosing the correct length of fibre the same fibre may be used at different gain values. For larger gains, it is important to tailor the pitch of the fibre to the specific gain.

These investigations assume that the pump and signal light are already coupled to the fibre in question. For real use one must also take the coupling issues into account. The PCF, with the optimum design, has a signal MFD of about 1.7 microns, which makes it very difficult to couple light into and out of the fibre. Simple butt coupling such a fibre to a standard single mode fibre with an MFD of about 8 microns will result in a loss of about -8 dB. As a consequence, it will be necessary to address this problem if this design should be used in a system configuration. The fibre also has a high nonlinear coefficient due to the small MFD. Nonlinear effects are, however, not significant when the fibre is operated at such low intensities.

4.4 Summary of chapter 4

In this chapter the design of highly efficient fibre amplifiers have been described. By using PCFs with very large air holes, it is possible to design amplifiers with very small mode field diameters and, as a consequence, obtain gain in these fibres with very low pump powers. 15 dB gain may be obtained with less than 0.7 mW of optical power.

The design help to illustrate that the flexibility of PCF technology may allow us to design PCF amplifiers for specific applications that will outperform amplifiers based on standard fibres. However, to take full advantage of the technology, it is necessary to address the coupling issues.

Chapter 5

Air-guiding Photonic Crystal Fibre Lasers

As described previously, in chapter 3.1.3 and chapter 3.2.3, double cladding fibres have made it possible to design fibre lasers with very high output powers [52, 62, 82, 83]. Output powers of double cladding fibre lasers are typically limited by the available pump sources. But as pump sources evolve, and pump powers reach hundreds or even thousands of watts, output powers may be limited by other mechanisms such as non-linear effects, or the electric field strength reaching the dielectric breakdown limit. To increase power levels further, the light intensity in the silica, must be reduced. This is generally achieved by increasing the core area [52], but this approach eventually leads to problems such as high bending sensitivity, multi-mode fibres, and difficulties controlling the refractive index step to the core, which must be reduced, in order to limit the number of guided modes. See chapter 3.1.3 for more details on this. In chapter 3.2.3 a *large-mode area* (LMA) *photonic crystal fibre* (PCF) was described, which could alleviate some of these problems, but bending losses would still impose limitations on the effective mode area of such fibres.

This chapter describes the possibility of using air-guiding PCFs as double cladding fibre lasers. Since the field is then primarily located in the hollow

core, both the non-linear effects and the maximum field intensity in the silica, at a given power level, may be reduced significantly. Guidance of 1 nanosecond pulses with peak powers up to 10TW in hollow capillary tubes have been demonstrated in the literature [84], showing that confining the light to air may indeed be used to increase peak powers significantly. The leaky nature of the light in a hollow capillary tube, limits the propagating lengths in these devices to about $10mm$, but using air-guiding fibres the problem of effectively confining the light is solved. This have recently been exploited to transmit pulses, with pulse energies high enough to damage bulk silica, through hollow core PCFs [85–87]. Those investigations have considered high power delivery through passive air-guiding fibres, while this chapter will include discussions of how to incorporate the amplifying stage into the air-guiding fibre. Apart from the low field intensity, air-guiding fibres also posses excellent bending properties [88], and could therefore have the potential to deliver more power, without the limitations imposed on fibre lasers based on solid core fibres.

Using *photonic bandgap* (PBG) fibres also means that one must operate within in a narrow spectral window. The signal mode must be inside the bandgap region. The width of the bandgap for air-guided modes depends on the normalized hole size. Fig. 5.1 show the width of the bandgap region as a function of hole size. The bandgap width is defined as the gap width to centre frequency ratio. The other y-axis show bandgap width in nanometers, if the signal wavelength of 1060nm is located in the middle of the gap. For large hole sizes the spectral widths may exceed 300nm, while the possible wavelength interval is less than 30nm wide for $\frac{d}{\Lambda} = 0.81$. For small hole sizes, the size of the spectral window could be a limiting factor, if short pulse applications are considered. The bandgap width may also be further descreased by including the core in the calculation. Depending on the design, the core may introduce surface modes, which causes loss peaks at the avoided crossings in the bandgap, as described previously.

5.1 Rare-earth-doped air-guiding fibres

The first question which arises, is where to position the *rare-earth* (RE) ions. As seen previously, the RE ions should be positioned where overlap

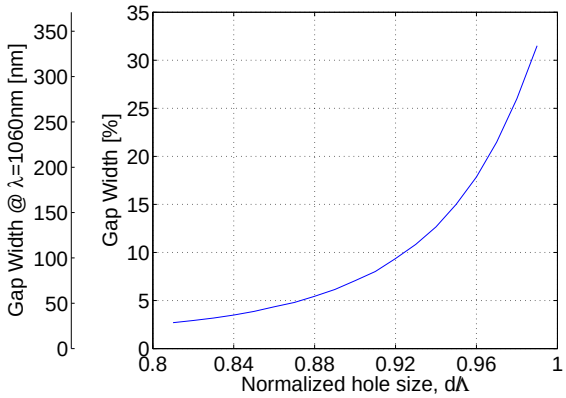

Figure 5.1: *Width of the photonic bandgap region as a function of normalized hole size. The gap width is defined as the ratio between the gap width and the centre frequency. The width in nanometers for a centre wavelength of 1060nm is also shown.*

to the field and the pump is as high as possible, but in this case the signal field is confined to the air core, where it is not possible to place the RE ions. A fraction of the light is, however, located in the silica material in the vicinity of the core, and it is therefore possible to have interaction between the air-guided mode and the RE ions. As described in the previous chapter, the positioning of the RE materials is very important if optimising the pump usage has priority. For double cladding high power fibre lasers, however, a main challenge often is to efficiently absorb the available pump light, due to the large cladding-to-core area ratio. So to absorb the pump light in a sufficiently small length of fibre, the area of the doped region and the concentration must be large. The doping concentration is limited by the solubility of the RE-ions in the silica glass, while the area of doping is limited by the signal overlap with the glass regions. This last point will be discussed in section 5.3.

5.1.1 Ytterbium based fibre laser

In this chapter only ytterbium is considered as RE ion. The reason for this is the low quantum defect, as described in chapter 3.1.1. Since the im-

portant advantage of using air-guiding fibres as fibre lasers, is the reduced field intensity in the silica regions, air-guiding fibre lasers are, essentially, only for high power applications. This means that a large quantum defect will result in a huge amount of power being transformed to heat, which will lead to both a reduction in the slope efficiency and a need for active cooling and/or reduction in the maximum power which can be delivered. Therefore RE elements such as erbium cannot be used. Due to the importance of efficient pump absorption it is also necessary with a RE ion with a large absorption cross-section, which again makes ytterbium the RE ion of choice. A pump wavelength of 976nm and a signal wavelength of 1060nm is assumed.

5.2 Design considerations

5.2.1 Double cladding structure

The only way to achieve the very high output powers needed, is to use double cladding fibres, since you need high power diode laser pumps, hence the hollow core fibre must have a double cladding structure. These fibres must support modes which are confined to the air core *and*, in order to promote pump coupling, should have as large a *numerical aperture* (NA) to the outer cladding as possible. This is difficult to obtain simultaneously, since in general, large holes are needed to confine light to the air core, but large holes reduce the NA to the outer cladding. These issues are discussed later in the chapter. An example of an air-guiding fibre, with a double cladding, is shown in Fig. 5.2.

5.2.2 Idealised structures

The PCFs considered in this chapter are all *idealised* structures, in the sense that all holes are circular and have the same size. The core is created by inserting a larger hole in the centre of the structure. As shown in chapter 2.4.1, manufactured hollow core fibres tend to have slightly hexagonal air holes, and, due to surface tension during the high temper-

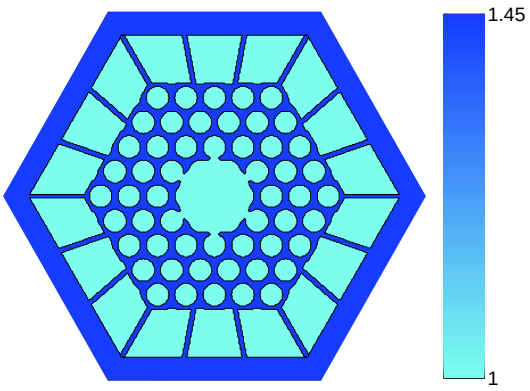

Figure 5.2: *An example of a double-cladding air-guiding PCF. The inner cladding, which must have a photonic band gap extending below the air line, is surrounded by an outer cladding, with a very high air filling fraction, enabling coupling of pump light to the inner cladding.*

ature fibre drawing process, the shape and size of the core and the holes near the core are altered. Such *real* fibres may, as shown in chapter 2.2.4, be represented quite accurately with the developed numerical tools, but to isolate the influence of specific parameters, (the hole size and the core size), the number of degrees of freedom have been minimized. Specifically, this design allows for creation of cores in the fibres, without introducing surface modes [47]. So even though the exact fibre designs considered here might be difficult to realize, the investigations gives valuable information about the considered parameters, which would otherwise be difficult to isolate.

The choice of circular air holes results in a maximum air filling fraction of 90.7%. Since the considered fibres are double cladding fibres, and the NA to the outer cladding is important, it will not be desirable to have higher air filling fractions, so this limit on the air filling fraction is not a problem.

Normalized hole sizes from $\frac{d}{\Lambda} = 0.8$ to $\frac{d}{\Lambda} = 0.99$ are considered. Modes confined tightly to the core region can be found for any hole size in this interval, as shown in Fig. 5.3. For larger air holes, the modes are tighter

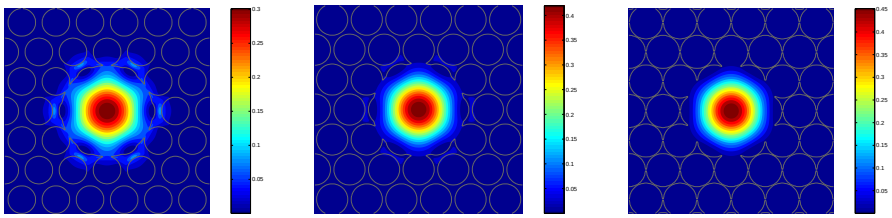

(a) $\frac{d}{\Lambda} = 0.81$ (b) $\frac{d}{\Lambda} = 0.90$ (c) $\frac{d}{\Lambda} = 0.99$

Figure 5.3: *Fundamental air-guided mode profile for three values of the hole size.*

confined to the core. For smaller hole sizes, it is still possible to find guided modes, but the modes are weaker confined and more difficult to separate from cladding and surface modes. For hole sizes below $\frac{d}{\Lambda} = 0.77$ it is no longer possible to find modes, with the majority the light located in the air core.

5.2.3 Core design

Three different core designs were investigated. These three core designs are shown in Fig. 5.4. The red areas surrounding the core regions are examples of how such fibres could be doped. The three core radii, are chosen so that they lie in first three intervals without surface modes, described in chapter 2.4.1 and in [47]. The second and third core design resemble the two most used air-guide core designs, the 7-rod and the 19-rod cores, while the first small core is chosen to investigate the effects of a smaller cores. Only the smallest core design results in single mode behavior in the complete bandgap.

5.3 Ytterbium distribution

As previously mentioned, the optimum distribution of the RE ions is primarily determined by the signal field distribution. This means that the more the signal field penetrates into the silica regions, the larger

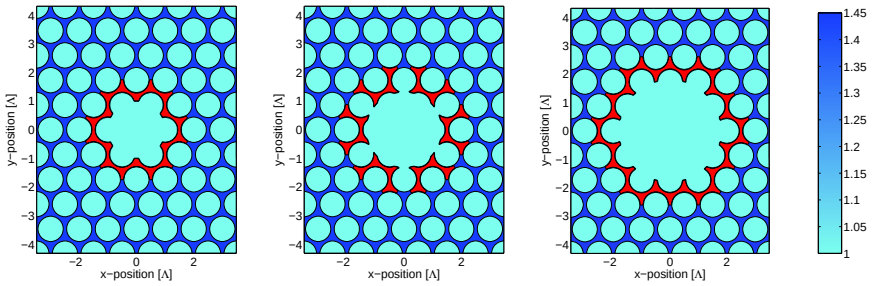

(a) Core rad. $= 1\Lambda$ (b) Core rad. $= \frac{\sqrt{7}}{2}\Lambda$ (c) Core rad. $= \frac{\sqrt{13}}{2}\Lambda$

Figure 5.4: *Index profiles of fibres with three considered core designs. All core radii is chosen to avoid surface modes. Note that a core radius of* $\sqrt{13}\Lambda/2$ *and* $\sqrt{7}\Lambda/2$ *may result in multi-mode fibres, depending on the hole size. The red regions surrounding the core areas, show how the fibre could be doped in the silica regions.*

should the doping area be.

Other factors which should be considered include pump efficiency and noise. By doping any area, where the signal field intensity is non-zero, the gain per unit length of fibre is increased — under the assumption that enough pump power is present to invert the RE-ions. However, if the signal field strength is very low, the increase in gain may be very small, and the increased doping area will also result in more noise and lower pump efficiency, since more power will be lost to *spontanous emission* (SE) and *amplified spontaneous emission* (ASE). Therefore, when the signal strength becomes too low, it will be more advantageous to obtain an increase in output power by using a longer fibre, with all the advantages and disadvantages this will incur. Thus, the optimum area of doping depends on the signal field distribution, but also on the specific application.

5.4 Overlap between core mode and rare-earth ions

A prerequisite to determine the optimum dopant distribution is knowing how the signal field is distributed. In this section a thorough investigation

of the signal field is presented. The intensity distributions of the signal modes are examined by calculating the electric power density, u, defined as:

$$u \;=\; \frac{1}{2}\,\mathbf{E}\cdot\mathbf{D} \;=\; \frac{1}{2}\,\epsilon\,\mathbf{E}^2 \tag{5.1}$$

The units used, correspond to the power density being normalized according to:

$$\int_{\Omega} u \,\mathrm{d}a \;=\; 1 \tag{5.2}$$

where Ω is the fibre cross section. The power density is used because the stimulated absorption and emission from the RE-ions in a given section are proportional to the power density. As mentioned, only idealised structures are considered. This means that the fundamental mode consists of two orthogonal, quasi-linear, degenerate polarisation states. Since the core modes consists of two polarisation states, the power density, calculated for the fundamental mode, is an average of the power density of the two degenerate polarisation states.

5.4.1 Numerical approach

The electric field is calculated as described in chapter 2.2, primarily using the finite difference method. A primary goal of these investigations is to determine the fraction of power in the silica and air regions respectively. This is done by multiplying the power density distribution with a structure matrix, which have a value of 1 in considered regions and a value of 0 in the remaining cross section and then integrating over the fibre cross section. Since the structure matrix is created using the previously described *subgridding*-method (see chapter 2.2.4), some points, which are located on a silica/air boundary, will have a value between 0 and 1. When the power density is calculated using the generated structure matrix, it is assumed that the power in these boundary computational cells are evenly distributed, which might not be the case. It is difficult to assess how large the resulting error is. If a cell is half air and half silica, it is tempting to assume that the majority of the power in the cell is located in the silica, since light tends to concentrate in the high index regions. At the same time, the distribution in the cell also depends on the overall change in the

field strength on a larger scale, and last but not least, the field must, of course, fulfil the electromagnetic boundary conditions, which means that the orientation between the polarisation and the material interface plays a significant role. It would be possible to make simulations to examine this problem, but since several factors has influence on the result, it would be difficult to obtain a general solution, therefore a uniform distribution is assumed in the calculations performed.

This problem has only minor implications in general, but when energy distributions in small silica regions are considered, it becomes a significant source of error. When the air holes become large, the number of points on the air/silica interface increases, and the total number of points in the silica regions decreases. For a hole size of $\frac{d}{\Lambda} = 0.95$ and a resolution of 30 points per unit cell, the total number of computational cells in each silica node[1] is approximately 85. The number of cells on the air/silica boundary is about 37. This means that a significant fraction of the cells are on the boundary, where it is difficult to determine how the power is distributed. To compensate for this, the resolution in these calculations must be increased, compared to the calculations performed previously, in order to obtain reliable results. The resolution in the following calculations is therefore fixed at 50 points per unit cell. The accuracy has been tested, using a few higher resolution results. The size of the supercell used is $10\Lambda \times 6\sqrt{(}3)\Lambda \approx 10\Lambda \times 10\Lambda$. This results in computations, where a single mode/eigenvalue is found in 3-4 minutes (approximately 7 minutes for both polarisation states).

5.4.2 Radial intensity distribution

The electric power density is now calculated, for the fundamental mode in an air-guiding fibre with a hole size $\frac{d}{\Lambda} = 0.88$ and a core size of $\sqrt{7}\Lambda$. In Fig. 5.5(a) the guided mode for a frequency in the middle of the bandgap is shown. The light is strongly confined to the air core (Fig. 5.5(a)), but a small fraction of the power (about 6 percent), is located in the silica region, which is clearly seen in Fig. 5.5(b), which shows the same mode, but with the part of the power which is located in the air, removed. The

[1] Silica regions between three air holes as defined in chapter 2

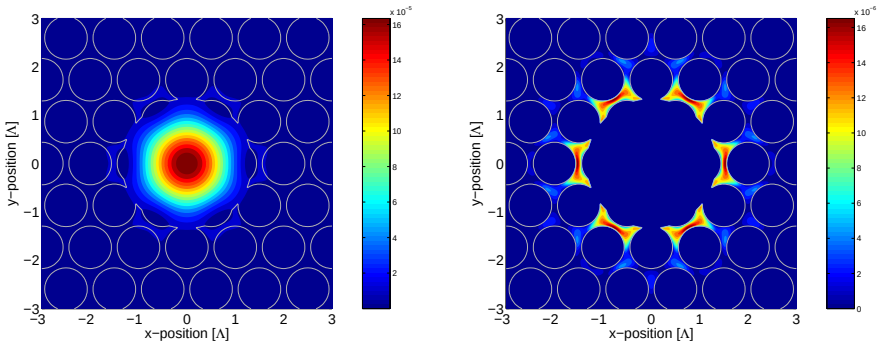

(a) Fundamental mode.

(b) Power in the air removed.

Figure 5.5: *Electric power density of an air-guided mode, and the same mode plotted where all the power, which were located in the air, is removed.*

intensity is relatively high in the innermost silica regions, but some power in the surrounding silica nodes can also be seen.

To better determine how the active material should be positioned, the signal field intensity distribution in the fibre cross-section is investigated more thoroughly. To find the signal intensity in the silica regions, the nodes are divided into groups, with each group of nodes located symmetrically around the core, at a fixed distance from the centre of the fibre. Fig. 5.6(a) shows this grouping. The distance to the centre, for the first 4 node groups are $\sqrt{7/3}$, $\sqrt{13/3}$, $\sqrt{16/3}$, and $\sqrt{19/3}$, respectively, while the distance in the last group varies between $\sqrt{25/3}$ and $\sqrt{37/3}$.

The electric power density in the fibre, and in the individual node groups, is then calculated as a function of radial position, for a normalized hole size of $\frac{d}{\Lambda} = 0.88$, and a normalized frequency $\frac{\Lambda}{\lambda} = 1.42$, which is the centre of the bandgap. The result is shown in Fig. 5.6(b). The black curve shows the total power density, the blue show the power density in the silica, while the remaining curves show the power density in the individual node groups. The intensity is Gaussian shaped in the core region (parabolic on the logarithmic scale), and decreases in the cladding region. The four colored arrows indicate the centres of the first 4 node groups. The majority of the light is located in the first node group, but

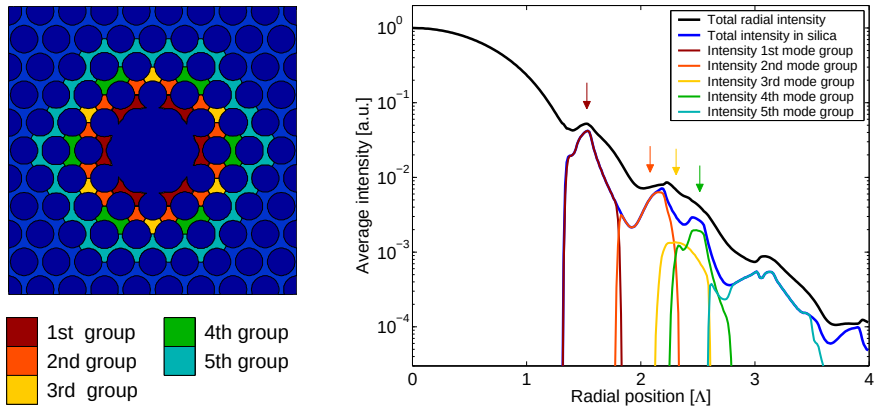

(a) The silica nodes surrounding the core are divided into groups.

(b) Radial intensity distribution in total and in different silica nodes for a guided mode in an air-guiding fibre.

Figure 5.6: *Grouping of the silica nodes, and radial intensity in the individual node groups. Colored arrows shows the centres of the node groups. The blue curve is the total intensity in silica.*

the exponential decrease in the cladding is not very steep, and a non-trivial part of the light is located in silica regions further away from the core. By looking at the difference between the black curve for the total power and the blue curve for the power in silica, it is also seen that some light is located in air regions outside the core area. In total, this mode has 88.4% of the power located in the core, about 6% in the silica, and the remaining 5.6% in the air regions outside the core. These numbers together with the intensity and power in the node groups are summarised in Table 5.1. Of the 6% power in the silica, two thirds are in the first node group, and only one-sixth is outside the first two node groups. Doping, for instance, the first two node groups, would give 83% of the maximum possible gain for the signal, which would be equal to 5% of the gain the mode would experience, if it was completely confined to a doped glass region.

On a side note, these numbers also illustrate one of the reasons that losses in PBG fibres typically are higher, compared to index-guiding fibres. The field is weaker confined, and the field intensity typically decreases slower

	Number of nodes in group	Avg. intensity (normalized)	Total power fraction in area	Glass power fraction in node group
1st node ring	12	1.00	3.95%	65.6%
2nd node ring	12	0.27	1.07%	17.7%
3rd node ring	6	0.15	0.29%	4.9%
4th node ring	12	0.087	0.34%	5.7%
5th node ring	42	0.019	0.27%	4.4%
Remaining silica	n.a.	n.a.	0.10%	1.7%
Total in	n.a.	n.a.	6.0%	100%
Air core	n.a.	5.7	88.4%	n.a.
First hole ring	n.a.	0.25	4.8	n.a.
Remaining air	n.a.	n.a.	0.8%	n.a.

Table 5.1: *Power distribution in different sections of a fibre.*

in the cladding region, compared to *conventional optical fibres* (COFs). Surface roughness in the cladding then couples the core mode to lossy cladding modes. Thus to achieve very low losses, it is necessary to have a significant number of hole rings, and avoid surface roughness as much as possible.

5.4.3 Bandgap variations

The calculations in the previous section was performed for a guided mode in the middle of the bandgap. The power distribution varies across the bandgap, and to form a general view it is therefore necessary to examine these variations.

In Fig. 5.7 the effective index of the fundamental mode across the bandgap is shown. Again a hole size of $\frac{d}{\Lambda} = 0.88$ is used as an example. The gray region is the bandgap, which is surrounded by a large number of cladding modes. The cladding modes defining the bandgap are indicated with red lines. The green line indicate modes, which are confined to the air core region. As in chapter 2.4.1, the white regions outside the shaded area are not photonic bandgaps, but a result of the finite size of the su-

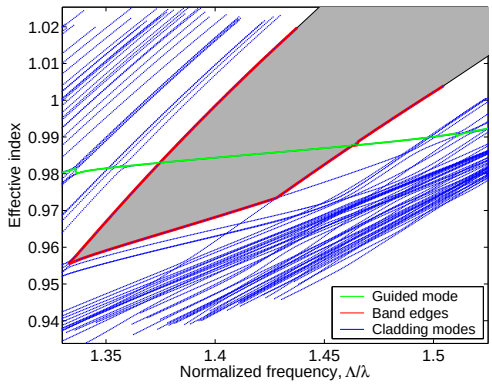

Figure 5.7: *Modes in an air-guiding fibre with a hole size* $\frac{d}{\Lambda} = 0.88$. *Blue lines indicate cladding modes and the green line indicate modes confined to the air core. Red lines shows the cladding modes, defining the edges of the shaded bandgap region.*

percell. As the figure shows, it is possible to find confined core modes outside the bandgap. These modes do exist, but the loss in such modes will be very large, due to the existence of cladding modes with almost the same effective refractive index.

The investigations described in the previous section is then repeated for guided modes along the green line. Fig. 5.8 shows the fraction of power in the silica and in the different node groups as a function of normalized frequencies across the bandgap region. Fig. 5.8(a) shows the fraction of the total power, which is confined to the silica regions, and Fig. 5.8(b) shows the fraction, of the power in silica, located in the different node groups. At this hole size the power distribution is relatively constant across the bandgap. The fraction of power in the silica regions ranges from 6% close to the low frequency band edge, to 7% at the high frequency band edge. The power in the node groups is also almost constant across the bandgap, with 60% to 66% (of the power in the silica) located in node group 1 and about 18% in node group 2. This means that, for this hole size, the power distribution is relatively insensitive to the position in the bandgap, and the optimum position is free to be determined from other parameters. Notice that outside the bandgap region the fraction of power in the silica regions has several pronounced spikes, corresponding

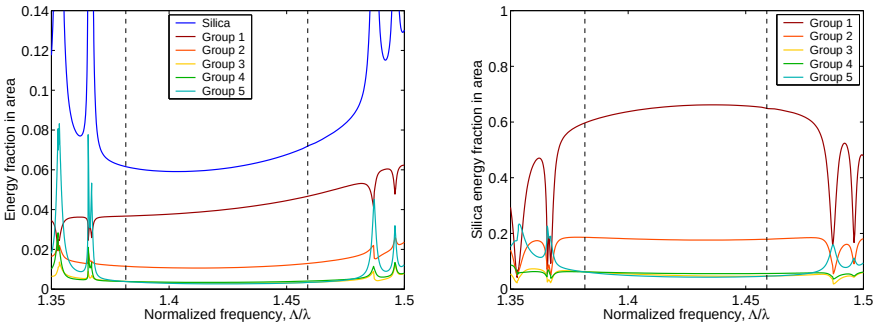

(a) Total power fraction in node groups

(b) Fraction of power in silica in each node groups

Figure 5.8: *Power distribution in the silica and in the defined silica node groups (see Fig. 5.6(a)) plotted for frequencies across the bandgap. Total power fraction in silica and silica nodes, (a), and fractional part of the power in silica, located in the different node groups (b). Dashed black lines indicate bandgap edges.*

to avoided crossings with certain core modes. This can also just be made out in Fig. 5.7, since the effective index curve of the core mode (green curve) jumps slightly at these crossings. No peaks are observed when the guided modes crosses the cladding modes forming the bandgap edges. Avoided crossing still occurs, but the transition region is very narrow, and the resolution in Fig. 5.8 is too coarse to show it. The width of the avoided crossings at the band edges are about $0.1nm$ compared to about $5 - 10nm$ at the crossings which generates the peaks in Fig. 5.8.

These investigations show that some variations do occur across the bandgap. Generally the optimum position will be where the mode is best confined to the air core. Some light *is* needed in the cladding region, to allow for gain, but if the silica power fraction should be increased it is more beneficial to do so, by decreasing the hole size, since this will improve the important NA.

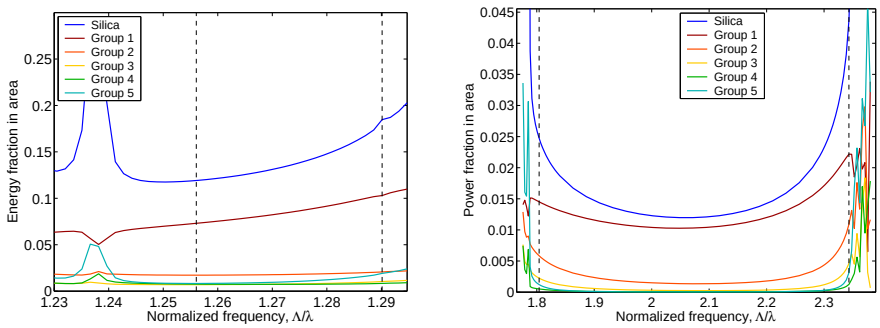

(a) Hole size $\frac{d}{\Lambda} = 0.81$ (b) Hole size $\frac{d}{\Lambda} = 0.98$

Figure 5.9: *Electric power density in silica and in the individual node groups for frequencies across the bandgap and for two values of the hole size. Vertical dashed lines indicate bandgap edges.*

5.4.4 Hole size variations

For a hole size of $\frac{d}{\Lambda} = 0.88$ the power distribution do not depend on the position in the bandgap. This is, however, not the case at all hole sizes. Fig. 5.9 shows the same sweep over the bandgap region as in Fig. 5.8(a), but for a hole size of $\frac{d}{\Lambda} = 0.81$ (a) and $\frac{d}{\Lambda} = 0.98$ (b).

For a hole size of $\frac{d}{\Lambda} = 0.81$ the fraction of power in the silica is 50% higher at the high frequency band edge (18%) compared to the low frequency band edge (12%). This increase at the high frequency edge is caused by an increased coupling to the cladding mode defining the bandgap edge, resulting in a weaker confinement of the mode. Notice that the amount of power in the 5th node group is increased by more than a factor of two across the bandgap, indicating that the light spreads out into silica nodes in the entire cross section of the fibre, which would increase the loss considerably. The increase starts out approximately in the middle of the bandgap. This effect will tend to drive the optimum position in the bandgap towards the low frequency band edge. The increased coupling to band edge modes is even more pronounced when very large holes are considered. Fig. 5.9(b) shows the power distribution for a hole size of $\frac{d}{\Lambda} = 0.98$, where the hole edges almost touch the neighbouring holes. The power in the silica regions increase drastically at both band edges,

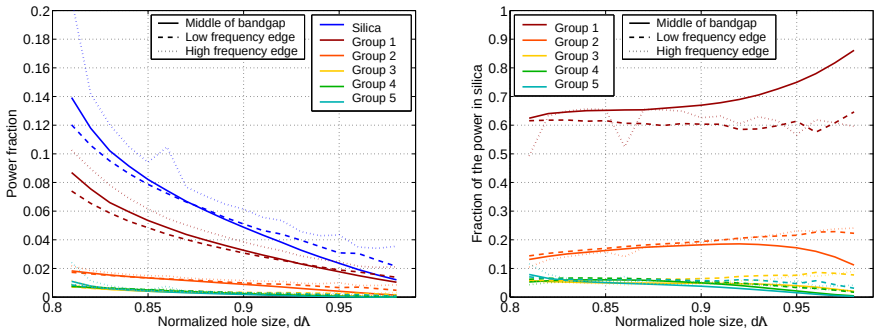

(a) Total power fraction in node groups

(b) Fraction of power in silica in node groups

Figure 5.10: *Fraction of the power located in silica and in the individual nodegroups, as a function of normalized hole size. (a) shows the fraction of the total power, (b) shows the fraction of the power located in the silica.*

meaning that such a fibre must be operated in the centre of the bandgap.

To more generally investigate influence of hole size variations, calculations, similar to the above described, are performed for normalized hole sizes between 0.80 and 0.99. For each hole size, the power distribution is examined at three frequencies in the bandgap. One in the middle of the bandgap, one 5% (of the bandgap width) above the low frequency band edge and one 5% below the high frequency edge. The results are shown in Fig. 5.10

The figure shows, as expected, that larger air holes results in a lower fraction of power in the silica. This is a result of the larger air-filling fraction, but also due to tighter confinement of the core mode to the air core. Tight confinement results in a faster decay of the intensity in the cladding region. The improved confinement can be seen by looking at the solid lines in Fig. 5.10(b), which shows that the power in the silica becomes almost entirely confined to the first node group. Thus larger air holes will then, as expected, result in a lower gain value in the laser, due to the declining coupling between the signal mode and the active ions.

Fig. 5.10(a) also show a general trend that larger holes leads to more

power in silica at the band edges, as shown for $\frac{d}{\Lambda} = 0.98$ in Fig. 5.9(b). For smaller holes the power in the silica increases near the high frequency edge, but drops, compared to the middle of the bandgap, at the low frequency edge. While the trend for larger holes is very general, the behaviour for small hole sizes is actually very dependant on the core design. If the core size is increased slightly, from $\sqrt{7} \approx 2.65$ to 2.90, the power will instead increase in the silica near the low frequency band edge. The increasing power levels in the silica regions are controlled by the coupling to cladding modes and surface modes, and is therefore highly sensitive to the choice of core design. Thus for small hole sizes, the optimum position in the bandgap depends on the core design.

These investigations show that it is difficult to give a general description of how the signal power distribution varies across the bandgap. In most cases, operating in the centre of the bandgap is a sensible choice. It is, however, not a foolproof choice. For normalized hole sizes below about 0.9, a better mode confinement to the core region, may typically be achieved away from the centre of the bandgap, towards the low frequency band edge. Better confinement to the core region is desirable, since it allows for smaller hole size, which will give a larger numerical aperture to the outer cladding and increases the area which may be doped.

Concerning which regions should be doped with RE-ions, the investigations have shown that the power distribution in the silica, remains relatively constant, not only across the bandgaps, but also within a broad hole size interval, ranging from $\frac{d}{\Lambda} = 0.80$ to $\frac{d}{\Lambda} \approx 0.92$. In this interval, and for a core diameter of $d = \sqrt{7}\Lambda$, about two thirds of the power in the silica is located in the group of nodes closest to the core. About one sixth of the power is located in the second group of nodes. Doping of the first two node groups therefore seems like a rational choice. If the hole size is large, it may be better to only dope the first node group. The resulting overlap between the signal and the doped region is shown in Fig. 5.11.

The results presented above was for a core diameter of $\sqrt{7}$. For the other investigated core designs a different definition of node groups was needed. The general behaviour of the fraction of light in air for all three core sizes are shown in Fig. 5.12. Larger core sizes means that a higher percentage of the power may be confined to the core region. Even for small air holes

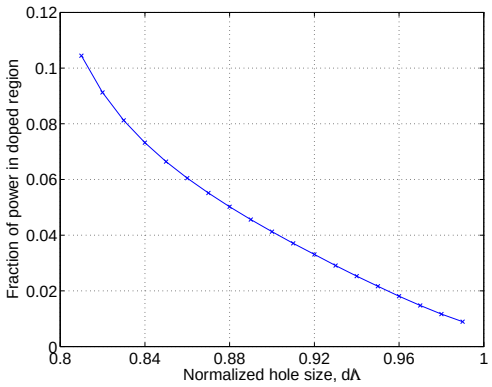

Figure 5.11: *Fraction of signal power in the region chosen for doping, which is node group 1 and 2.*

more than 90% of the power is in the core region for a corediameter of $\sqrt{13}\Lambda$. Using large air holes more than 98% of the light may be confined to the air region (95% in core) even for a core size of 2Λ, and less than half a percent of the light is located in silica if the core diameter is $\sqrt{13}\Lambda$.

5.5 Pump distribution and absorption

Double cladding structures are typically pumped in the outer cladding using high power diode arrays. It is important to efficiently absorb the launched pump power, which is governed by the overlap between the doped region and the pump light. As described in chapter 2.4.1, the number of modes in the outer cladding is very high, and the beam quality of the pump diodes is very low, therefore it is very difficult to to use a modal analysis to accurately determine the pump distribution in the inner cladding.

In the literature the general approach is to assume that the pump distribution in the inner cladding is uniform. This means that the absorption is purely determined by the concentration of RE-ions and the area ratio between the doped region and the inner cladding. In the case of air-guiding double clad structures, the cladding consists of large air holes in silica,

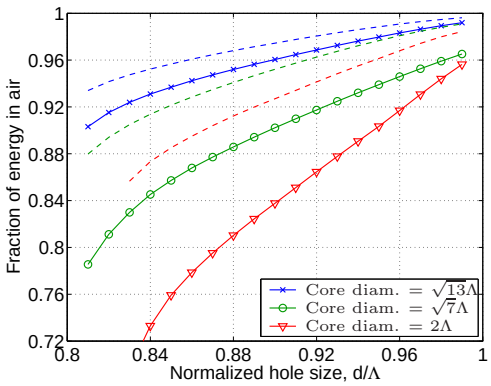

Figure 5.12: *Fraction of power in air and in the core area, for three values of the core size, as a function of the normalized hole size. Dashed line show power in air, solid lines show power in the core region.*

thus the pump light can no longer be assumed uniform, but will likely have increased intensity in the high index regions.

5.5.1 Pump distribution in inner cladding

The primary bandgap in an air-guiding fibre is located between the 4th and 5th band in the simple cell. Therefore the first 4 modes have effective indices above 1 and the higher order modes have indices below 1, since the bandgap must cover the region around 1. This means that all pump light, which is coupled to modes below the bandgap is lost, since modes with index below 1 cannot be confined (without a bandgap). The first 4 modes are all modes with the power located in the high index nodes of the structure. The sum of the power density in the first 4 modes of the simple cell (copied to fill a larger section) are shown in Fig. 5.13(a). If the size of the structure is increased, the number of modes above the bandgap is also increased, but the distribution still resembles the distribution in the four original modes, and if the power in all the modes are added up, the total distribution is unchanged, as shown in Fig. 5.13(b), which means that the power is located in the high index regions. The pump in the inner cladding is therefore assumed to be distributed as shown in Fig.

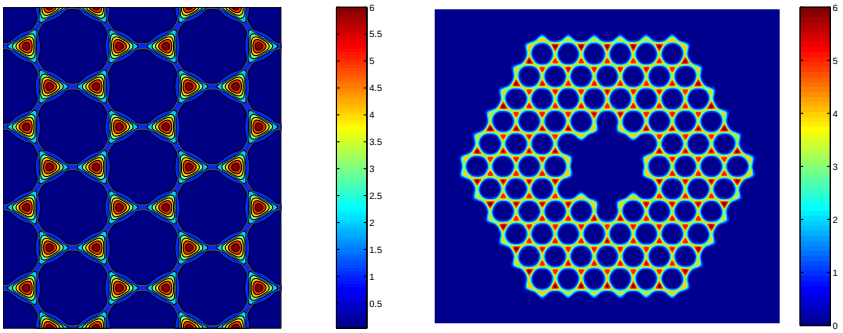

(a) Calculated from simple cell (b) Complete fibre structure

Figure 5.13: *Pump distribution in the inner cladding calculated from a simple cell (a) and a complete fibre structure (b). The pump power is confined to the high index regions.*

5.13(a), which means that the pump distribution can be evaluated from calculations on the simple cell. Using the distribution, it is possible to estimate both the coupling efficiency from the laser diodes and the pump absorption in the doped region.

Since the pump distribution is equal in all silica nodes, the pump absorption can be estimated simply by the base absorption in a doped node times the number of doped nodes divided by the the total number of nodes in the inner cladding. By increasing the size of the inner cladding, the absorption is thus reduced, as explained in chapter 3.1.3. A detailed analysis of the laser behaviour is needed to make a more accurate description of the pump absorption, because the absorption in the doped region depends on how efficiently the laser mode de-excites the RE-ions. The influence of the non-uniform distribution on the mode mixing are also neglected. Since the power is distributed in separate high index regions, effective mixing of the modes might be impossible, especially for high air-filling fractions, since the high index regions will then be more de-coupled.

Because the pump power is located in the high index regions, there will be a mode mismatch between the laser diode pump beam and the inner cladding pump distribution. This will result in a reduced coupling effi-

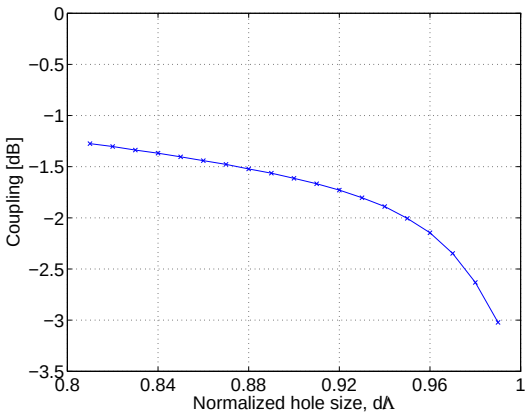

Figure 5.14: *Mode mismatch between pump and inner cladding. Coupling losses increase with the hole size.*

ciency. If the diode output distribution is assumed to be uniform, it is possible to estimate the coupling losses. The pump distribution is calculated for a range of hole sizes and the overlap between a the uniform diode pump distribution is evaluated. The result is shown in Fig. 5.14. The figure predicts loss values from 1.3dB at $\frac{d}{\Lambda} = 0.81$ to 3dB at $\frac{d}{\Lambda} = 0.99$. The light is confined effectively to the high index regions, which means worse overlap for larger holes. Coupling to the microstructured cladding is difficult, and the minimum loss in the curve corresponds to loosing 25% of the pump light at the interface.

5.6 Numerical aperture to outer cladding

The NA to the outer cladding should be as large as possible, in order to facilitate the coupling of pump power to the inner cladding. It is, however, not obvious how to determine the NA of the inner as well as the outer cladding regions.

Assuming that the outer cladding consists of one ring with thin silica bridges suspended in air, the effective index depends on three structural parameters, as indicated in Fig. 5.15. The distance between bridges,

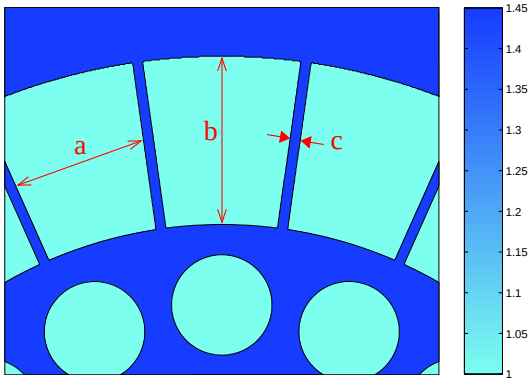

Figure 5.15: *Parameters determining the effective index of an outer cladding consisting of one ring of narrow silica bridges, suspended in air.*

marked a, the width of the air cladding region, or the length of the bridges, marked b, and the width of the bridges, marked c.

In these calculations it is assumed that the distance between bridges is large enough to avoid coupling between the bridges, and that the bridges are long enough to effectively separate the modes in the inner cladding from the modes outside the outer cladding. If this is fulfilled, the effective index of such a structure, may be approximated by the effective index of a corresponding slab waveguide. The effective index as a function of bridge width is shown in Fig. 5.16(a). The blue curve corresponds to the index of the fundamental TE-mode in a 1-dimensional slab waveguide. The effective index of a slab waveguide depends on the polarisation of the light. The effective index of the fundamental TM-mode is shown with red circles, which shows that the TE modes has the highest index, therefore the TE index is used to define the NA.

The effective index in the inner cladding must also be approximated. In the previous section, it was estimated that the pump signal was distributed as the *fundamental space-filling mode* (FSM) of the cladding structure. The effective index of the inner cladding, is therefore assumed to be the effective index of the FSM. This index, as a function of the normalized hole size, is shown in Fig. 5.16(b).

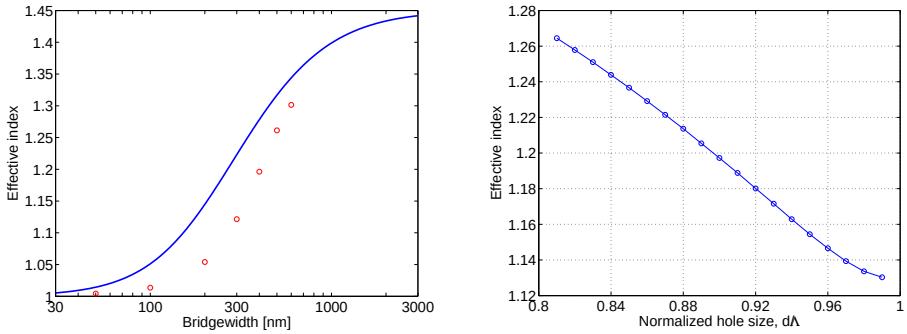

(a) Effective index of outer cladding (b) Effective index of inner cladding

Figure 5.16: *Effective index of the outer cladding as a function of silica bridge width (a), and the effective index of the inner cladding as a function of hole size (b).*

The resulting NA between the inner and outer cladding is shown in Fig. 5.17. The width of the bridges is of course very important. If the bridge width is 300nm, the effective index of the outer cladding is higher than the index of the inner cladding, for normalized hole sizes above 0.85. If the bridge width is below 100nm, very high NAs can be obtained, even to structures with very large air holes. Such narrow bridges are easily fabricated, but unfortunately these narrow bridges makes it very difficult to cleave the fibres. Therefore typical bridge widths in double cladding PCFs are typically around 300-400nm [89].

5.7 Maximum power level

The primary goal of using air-guiding PCFs as high power lasers, is the reduced light intensity in silica, which allows for a higher total power in the fibre, before reaching the *laser induced damage threshold* (LIDT) in the silica. Using the results presented in the previous section, it is possible to determine the increase in maximum power transmission.

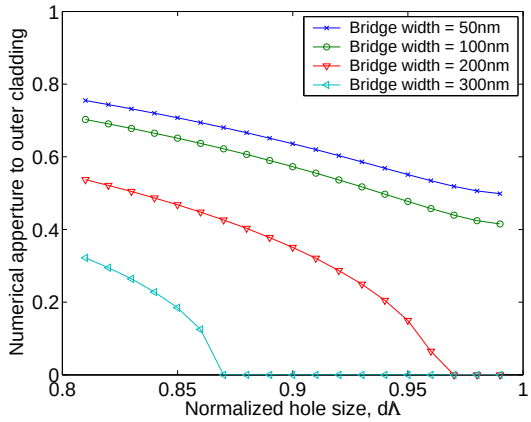

Figure 5.17: *Numerical aperture between inner and outer cladding as a function of the normalized hole size, for 4 values of the width of the outer cladding silica bridges.*

5.7.1 Laser induced damage threshold of silica

The LIDT of bulk silica depends on several factors, and can be difficult to determine accurately. Material properties, such as doping, impurities and local defects, such as bubbles or micro cracks, play a significant role, and the LIDT is also a function of both the light frequency and pulse duration [90]. Previous work report a LIDTs of bulk silica of $100 - 120\ J/cm^2$ at 1060nm and for 8 ns pulses [91], corresponding to a an average power in the pulse duration of $12.5 - 15\ GW/cm^2$. [92] reports a damage threshold in silica of $55 GW/cm^2$. In [93] a empirical formula for the LIDT of silica is expressed:

$$I_{th} \ = \ 1.45\ \lambda^{0.43} \tag{5.3}$$

where I_{th} is in J/cm^2 and λ is the wavelength in nanometers. The pulse width is $1.1ns$. At $\lambda = 1060$ (5.3) predicts a LIDT of $29 J/cm^2$, (or an average power of $26 GW/cm^2$). The LIDT is lower due to the shorter pulse duration. The LIDT of the cladding region of an air-guiding PCF has been estimated to $115 - 130 J/cm^2$ in $8ns$ pulses [86]. This was measured by exposing the complete cladding region, which means that a significant part of the light is incident on the air regions, and it is difficult to directly compare these results. However, the absolute value of the LIDT is not

critical, since the primary objective of these initial investigations, is to evaluate the improvement of air-guiding fibre lasers compared to COF-base fibre lasers. Therefore a maximum value of the peak power in the silica is chosen to be $I_{th} = 10GW/cm^2 = 100W/\mu m^2$, which is suitable to give an idea of the power levels obtainable, without taking properties such as pulse duration into account.

5.7.2 Power levels in air-guiding fibres

The position and size of the photonic bandgap depends on the size of the air holes. When the size of the air holes is decreased, the bandgap is shifted towards lower normalized frequencies, which (since the signal wavelength is constant) results in a smaller pitch. This is shown in Fig. 5.18(a). The pitch at $\frac{d}{\Lambda} = 0.99$ is $2.37\mu m$ but decreases to $1.35\mu m$ at $\frac{d}{\Lambda} = 0.81$. The smaller structure means smaller core and smaller *mode-field diameters* (MFDs), as shown in Fig. 5.18(b). When the MFD is normalized with respect to the pitch, the MFD of the fundamental mode is increased at smaller hole sizes, but due to the smaller pitch at lower hole sizes, the absolute MFD drops from $3.8\mu m$ at $\frac{d}{\Lambda} = 0.99$ to below $2.6\mu m$ for all hole sizes below 0.90. Lowering the MFD has the unfortunate effect of increasing the intensity at a given power level, thereby decreasing the maximum power transmittable in the fibre.

Maximizing the intensity

To evaluate the intensity and power levels obtainable, the maximum intensities in the fibres are calculated. The maximum intensity in the mode and the maximum intensity in silica are shown in both normalized units and absolute units in Fig. 5.19. The intensity is specified in Watts per area per Watt of total optical power. Without taking the absolute value of the pitch into account, the maximum intensity in the core of the fibre increases with the hole size, while the intensity in the silica region drops from $0.09\Lambda^{-2}$ to $0.0025\Lambda^{-2}$. This is because the light becomes more confined to the air core. The factor between the maximum intensity in the core and in the cladding, determines the maximum intensity, which may

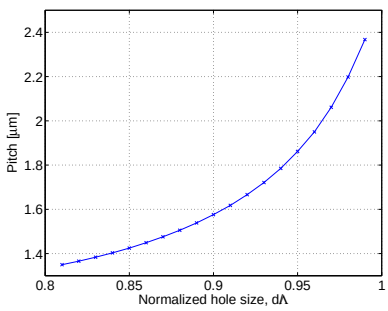

(a) Pitch as a function of hole size, for a fixed wavelength of 1070nm located in the middle of the bandgap.

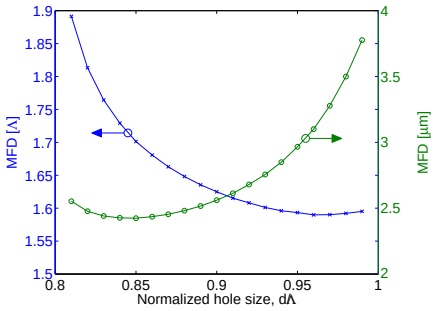

(b) Mode field diameter of the fundamental mode, specified in pitches as well as absolute units.

Figure 5.18: *Pitch (a) and mode field diameters (b) of the guided mode in the middle of the bandgap, as a function of hole size, for a core radius of* $\sqrt{(7)}/2$ *and center wavelength of 1070nm.*

be delivered by such fibres. The maximum intensity in the core is 3 times larger than the intensity in the silica at $\frac{d}{\Lambda} = 0.81$, and 20 times larger at $\frac{d}{\Lambda} = 0.99$. Previously the LIDT was assumed to be $100W/\mu m^2$, which means that an intensity of $2000W/\mu m^2$ can be obtained with a hole size $\frac{d}{\Lambda} = 0.99$.

Translating these numbers to absolute units, (Fig. 5.19(b)) shows that the maximum intensity in the silica regions decreases significantly for larger hole sizes. The maximum intensity is more than 10 times smaller at $\frac{d}{\Lambda} = 0.99$ compared to $\frac{d}{\Lambda} = 0.81$.

Maximizing the power level

Using the LIDT of $100\,W/\mu m$ and the maximum intensities found, the maximum transmittable power levels can be calculated. In Fig. 5.20 the maximum power level as a function of hole size is shown. The above investigations are made for the three defined core sizes. For comparison the maximum transmittable power for a *step-index fibre* (SIF), with a MFD of $6\mu m$ and a LMA-fibre with a MFD of $20\mu m$ is also shown in the figure, indicated with the horizontal lines. It is seen that for small hole

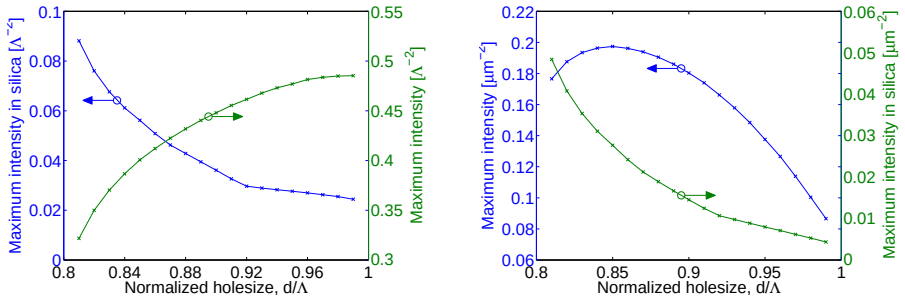

(a) Maximum intensity in normalized units.

(b) Maximum intensity in absolute units.

Figure 5.19: *Maximum intensity in air and silica as a function of hole size, for a guided mode in the middle of the bandgap. A maximum intensity of x/nm^2 means x W/nm^2 per Watt of optical power. Notice that the colors are reversed in the two figures.*

sizes, the power limit of the air-guiding fibres is actually lower than for a SIF, for two of the core designs, despite the fact that a significant part of the light is located in the air core. This is because a small hole size results in fibres with a small pitch and therefore a small MFD.

The power limit increases significantly when going to larger hole sizes, but as will be described, larger hole sizes has several unfortunate side effects. The power levels attainable in LMA fibres, may only be exceeded for large hole sizes and large core diameters. In high power applications, the core size is generally large, to increase possible power levels. The MFDs if the air-guides investigated here are small, compared to typical LMA-fibres. Despite having the majority of the light confined to the air core, the maximum intensity in the silica is higher in the air-guiding fibres with small cores, compared to LMA-fibres. Increasing the core-size will increase the power limit, but will lead to both multi-mode behaviour and very little overlap with the active material in the silica. Increasing the core area by increasing the pitch is not an option, because the considered wavelengths would then no longer be in the bandgap. Better performance might be obtained by moving to higher order bandgaps. Higher order bandgaps are located at higher normalized frequencies, resulting in physically larger fibres at the considered wavelength. The possibility of using higher order

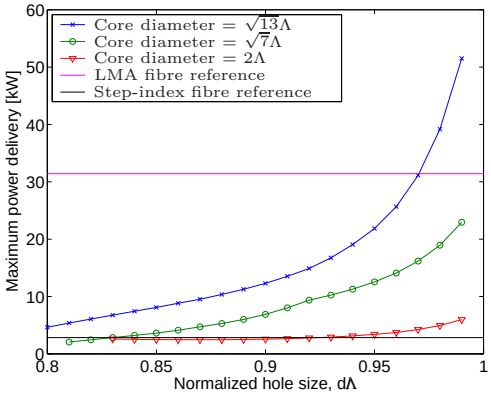

Figure 5.20: *Maximum transmittable power before reaching a LIDT of* $10GW/cm^2$*, shown as a function of hole size, for three different core designs. Horizontal lines indicate maximum power in a LMA-fibre (MFD=20) and a SIF (MFD=6).*

bandgaps has not been investigated.

5.8 Feasibility of air-guiding fibre lasers

The major areas of double cladding fibre amplifiers have been investigated. Some areas show promising results, but several problems are also encountered. The main areas considered were:

Core mode / dopant overlap: The overlap between the core mode and the doped region may reach values from 10% at $\frac{d}{\Lambda} = 0.81$ to only 1% at $\frac{d}{\Lambda} = 0.99$ for a core diameter of $\sqrt{13}\Lambda$. This should allow for reasonable gain values, as long as the core size and hole size is kept reasonable low.

Pump absorption: Neglecting questions about mode mixing, the pump absorption should not impose any limitations compared to existing technology. Mode mixing may, however, have serious implications. Pump light located in isolated high index regions might, limit the pump absorption, especially for large air holes.

Pump coupling: The coupling to the inner cladding is a significant problem. 25% to 50% of the light is lost at the interface. When dealing with high power applications and kilowatts of optical power, coupling losses of this magnitude is intolerable.

Numerical aperture: If the silica bridges in the outer cladding are kept sufficiently narrow, very high NAs may be obtained. However, this means that physical handling (cleaving, splicing, etc.) of the fibres might be an issue.

Maximum power levels: This is the primary motivation to use air-guiding fibres as fibre lasers. However, the location of the primary bandgap means that the MFD of the core modes are small, which means that the advantage of having the power in the hollow core cannot outweigh the increased intensity caused by the small MFD, compared to solutions based on index guiding LMA-fibres. For very large hole sizes and large core diameters the maximum power does supersede the value found for a $300\mu^2$ LMA fibre, but such a choice of parameters would result in severe problems in several of the areas above.

All things considered, air-guiding PCFs will not be able to compete with LMA PCF-based fibre amplifiers. Air-guiding fibres still have very interesting properties for high power / high intensity applications, but not as RE-doped lasers. In stead the fibres should be used for beam delivery, where no overlap with the silica is needed, and no outer cladding or pump sources is involved, such as described in chapter 2.4.1 and in [85–87].

5.9 Summary of chapter 5

In this section the use of double cladding air-guiding PCFs as RE doped fibre amplifiers have been investigated. The basic goal is to increase the maximum transmittable power, which is achieved by decreasing the light intensity in the silica regions. Several concepts have been investigated, but the overall conclusion is that RE-doping of air-guiding fibres cannot compete with fibre lasers based on LMA double cladding fibres. The only

way to increase the maximum power levels is to increase the hole size as well as the core size, which has several negative consequences, such as reduced pump coupling efficiency and multi-mode behaviour.

Chapter 6

Conclusion

Optical fibres are used extensively both within optical communication systems, but also in a number of other areas. By doping with rare-earth-ions, optical fibres may be used as optical amplifiers or fibre lasers. Such fibres have had a huge effect on optical fibre system deployment. The new class of optical fibres, *photonic crystal fibres* (PCFs), are becoming a viable alternative to conventional fibres within many applications, due to a wide range of interesting properties.

In this thesis the use of PCFs as rare-earth doped active fibres have been considered. The novel properties of PCFs may be used to design fibre amplifiers and lasers with improved performance.

The basic properties of PCFs have been investigated. The effective refractive index of the microstructured cladding region of a PCF is highly wavelength dependant. Small structures may result in large index contrasts, allowing for very tight mode confinement and large structures may result in small index contrasts, allowing for *large-mode area* (LMA) fibres, which have very large mode-field diameters. For hole sizes below approximately 0.45Λ, where Λ is the lattice period in the cladding region, PCFs only support a single guided mode irrespectively of the wavelength of the guided light. The highly wavelength dependant cladding index also result in very interesting dispersion properties.

The tight confinement of light, and thus small mode-field diameters, makes PCFs well suitable for non-linear applications, such as white light generation. LMA PCFs may be used to reduce the non-linear effects and enable laser beam delivery of very high power levels.

PCFs may also use a completely new guiding mechanism, *photonic bandgap* (PBG) guiding. This mechanism is fundamentally different from total internal reflection, which is the guiding mechanism of all previous optical waveguides. PBG guiding allow for confinement of the light to low index regions, something that is impossible with total internal reflection guiding fibres. Taken to its most extreme form, this may be used to confine light to air regions, where only a tiny fraction of the light is located outside the air core region.

The advantages of PCF based amplifiers and lasers have been described. Using the possibility of large air holes and thus tight confinement to the core region, it is possible to design high efficiency fibre amplifiers, which may deliver a small signal gain of 15dB using less than $0.7mW$ of optical pump power. Such components may be useful for creating transparent components for optical communication systems. Difficult coupling properties may be a serious obstacle for these devices.

Air-guiding fibres may be used to decrease the light intensity in the silica for a given power level, thereby increasing the power levels needed to reach the laser induced damage threshold of silica. Using air-guiding PBG fibres as double cladding, high power fibre lasers, was investigated, with the goal of designing a laser, capable of delivering output powers which would result in catastrophic damage to solid core fibre lasers. This was however not possible. Only for large core diameters and large hole sizes, did the maximum attainable power level exceed what can be obtained using index guiding, double cladding, LMA fibres. Large air holes in the cladding results in reduced pump coupling efficiency, and large core diameters results in bad overlap with the doped regions. Large air holes and large core diameters also results in multi-mode behaviour.

PCFs are already extensively used within a number of applications, and active rare-earth doped PCFs may become a significant player in the field of fibre amplifiers. The most mature area for active PCFs is LMA high

power lasers, where impressive results have already been published. PCFs are still lacking behind conventional fibres in many respects, but advances are being made in a rapid pace, and PCFs may become a very important part of the optical fibre systems of tomorrow.

References

[1] F.P. Kapron, D.B. Keck, and R.D. Maurer. Radiation losses in glass optical waveguides. *Applied Physics Letters*, 17:423–5, 1970.

[2] R.J. Mears, L. Reekie, I.M. Jauncey, and D.N. Payne. Low-noise erbium-doped fibre amplifier operating at 1.54 μm. *Electronics Letters*, 23(19):1026–8, 1987.

[3] Anders Bjarklev. *Optical Fiber Amplifiers, Design and System Applications*. Arctech House, Inc., 1993.

[4] Homepage of IPG Photonics. http://www.ipgphotonics.com.

[5] A. Katzir. Lasers and optical fibers in medicine. *Optics & Photonics News*, 2(2):18–22, 1991.

[6] Duncan P. Hand and Julian D.C. Jones. 300 Watt Nd:YAG laser delivery through single-mode optical fibres for micro-machining applications. *Laser Institute of America, Proceedings*, 83:A91–A98, 1997.

[7] J.P. Dakin and A.D. Kersey, editors. *Proceedings of the 1998 Fiber Optic and Laser Sensors and Applications, Including Distributed and Multiplexed Fiber Optic Sensors VII*, volume 3541. Society of Photo-Optical Instrumentation Engineers, 1999.

[8] J. C. Knight, T. A. Birks, P. St. J. Russell, and D. M. Atkin. All-silica single-mode optical fiber with photonic crystal cladding. *Optics Letters*, 21:1547, 1996.

[9] Anders Bjarklev, Jes Broeng, and Araceli Sanchez Bjarklev. *Photonic Crystal Fibres*. Kluwer Academic Publishers, 2003.

[10] P. Szarniak, W. Saj, R. Buczynski, D. Pysz, R. Stepien, and T. Szoplik. Modeling of highly birefringent photonic fiber with rectangular air holes in square lattice. *Transparent Optical Networks, 2003. Proceedings of 2003 5th International Conference on*, 1:216–219 vol.1, 2003.

[11] S.E. Barkou, J. Broeng, and A. Bjarklev. Silica-air photonic crystal fiber design that permits waveguiding by a true photonic bandgap effect. *Optics Letters*, 24(1):46–8, 1999.

[12] T.M. Monro, P.J. Bennett, N.G.R. Broderick, and D.J. Richardson. Holey fibers with random cladding distributions. *Optics Letters*, 25(4):206–8, 2000.

[13] K.P. Hansen. Dispersion flattened hybrid-core nonlinear photonic crystal fiber. *Optics Express*, 11(13):1503–1509, 2003.

[14] Jesper Riishede, Jesper Laegsgaard, Jes Broeng, and Anders Bjarklev. All-silica photonic bandgap fibre with zero dispersion and a large mode area at 730 nm. *Journal of Optics A: Pure and Applied Optics*, 6(7):667–670, 2004.

[15] T. A. Birks, J. C. Knight, and P. St. J. Russell. Endlessly single-mode photonic crystal fiber. *Optics Letters*, 22(13):961–963, July 1997.

[16] B. Scaife. *Principles of dielectrics*. Clarendon Press, 1989.

[17] Homepage of Crystal Fibre A/S. http://crystal-fibre.com.

[18] Steven G. Johnson and J. D. Joannopoulos. Block-iterative frequency-domain methods for maxwell's equations in a planewave basis. *Optics Express*, 8(3):173–190, 2001.

[19] Steven G. Johnson. MIT photonic-bands software. Available at: http://ab-initio.mit.edu/mpb/.

[20] Kenji Kawano and Tsutomu Kitoh. *Optical waveguide analysis*. John Wiley & Sons, 2001.

[21] J. Riishede, N.A. Mortensen, and J. Laegsgaard. A 'poor man's approach' to modelling micro-structured optical fibres. *Journal of Optics A: Pure and Applied Optics*, 5(5):534–8, 2003.

[22] A. Cucinotta, S. Selleri, L. Vincetti, and M. Zoboli. Holey fiber analysis through the finite-element method. *IEEE Photonics Technology Letters*, 14(11):1530–1532, 2002.

[23] CUDOS MOF utilities. Freely available simulation software. http://www.physics.usyd.edu.au/cudos/mofsoftware/.

[24] Kristian Hougaard, Anders Bjarklev, Erik Knudsen, Stig E. Barkou Libori, and Jesper Riishede. Coupling to photonic crystal fibres. *OFC 2002*, 70(ThGG11):627–628, March 2002.

[25] T.A. Birks, D. Mogilevtsev, J.C. Knight, P.St.J. Russell, J. Broeng, P.J. Roberts, J.A. West, D.C. Allan, and J.C. Fajardo. The analogy between photonic crystal fibres and step index fibres. *OFC/IOOC'99. Optical Fiber Communication Conference and the International Conference on Integrated Optics and Optical Fiber Communications (Cat. No.99CH36322)*, pages 114–16 vol.4, 1999.

[26] D. Marcuse. Loss analysis of single-mode fiber splices. *The Bell System Technical Journal*, 56(5), May - June 1977.

[27] M.D. Nielsen, J.R. Folkenberg, and N.A. Mortensen. Singlemode photonic crystal fibre with effective area of $600\mu m^2$ and low bending loss. *Electronics Letters*, 39(25):1802–1803, 2003.

[28] Thorkild Sørensen, Nikola Ivanov Nikolov, Ole Bang, Anders Bjarklev, Kristian Hougaard, and Kim Per Hansen. Dispersion engineered cob-web photonic crystal fibers for efficient supercontinuum generation. *Optical Fiber Communication Conference, 2004. OFC 2004*, 1:572–574, 2004.

[29] T.A. Birks, P.J. Roberts, P.S.J. Russell, D.M. Atkin, and T.J. Shepherd. Full 2-d photonic bandgaps in silica/air structures. *Electronics Letters*, 31(22):1941 –1943, 1995.

[30] Sajeev John. Strong localization of photons in certain disordered dielectric superlattices. *Physical Review Letters*, 58(23):2486–2489, 1987.

[31] Eli Yablonovitch. Inhibited spontaneous emmission in solid-state physics and electronics. *Physical Review Letters*, 58(20):2059–2062, May 1987.

[32] John D. Joannopoulos, Robert D. Meade, and Joshua N. Winn. *Photonic Crystals. Molding the Flow of Light.* Princeton University Press, 1995.

[33] R F Cregan, B J Mangan, J C Knight, T A Birks, P St J Russett, P J Roberts, and D C Allan. Single-mode photonic band gap guidance of light in air. *Science - International Edition - AAAS - Weekly Paper Edition*, 285(5433):1537–1539, 1999.

[34] J. Broeng, S.E. Barkou, T. Sondergaard, and A. Bjarklev. Analysis of air-guiding photonic bandgap fibers. *Optics Letters*, 25(2):96–8, 2000.

[35] B.J. Mangan, L. Farr, A. Langford, P.J. Roberts, D.P. Williams, F. Couny, M. Lawman, M. Mason, S. Coupland, R. Flea, H. Sabert, T.A. Blirks, J.C. Knight, and P. St.J. Russell. Low loss [1.7 dB/km] hollow core photonic bandgap fiber. *Optical Fiber Communication Conference, 2004. OFC 2004*, 2:728–730, 2004.

[36] P.J. Roberts, F. Couny, H. Sabert, B.J.Mangan, D.P. Williams, L. Farr, M.W. Mason, A. Tomlinson, T.A. Birks, J.C. Knight, and P.St.J. Russel. Ultimate low loss of hollow-core photonic crystal fibres. *Optics Express*, 13(1):236–244, January 2005.

[37] J.M. Pottage, D.M. Bird, T.D. Hedley, T.A. Birks, J.C. Knight, P.St.J. Russell, and P.J. Roberts. Robust photonic band gaps for hollow core guidance in PCF made from high index glass. *Optics Express*, 11(22):2854–2861, 2003.

[38] C.J.S. De Matos, S.V. Popov, A.B. Rulkov, J.R. Taylor, J. Broeng, T.P. Hansen, and V.P. Gapontsev. All-fiber format compression of frequency chirped pulses in air-guiding photonic crystal fibers. *Physical Review Letters*, 93(10):103901–1–103901–4, 2004.

[39] F. Benabid, J.C. Knight, and P.St.J. Russell. Particle guidance in hollow-core photonic crystal fiber. *Lasers and Electro-Optics, 2002. CLEO '02. Technical Digest.*, pages 48–49 vol.1, 2002.

[40] Jesper Laegsgaard, Niels Asger Mortensen, Jesper Riishede, and Anders Bjarklev. Material effects in air-guiding photonic bandgap fibers. *Journal of the Optical Society of America B: Optical Physics*, 20(10):2046–2051, 2003.

[41] Douglas C. Allan, Nicholas F. Borrelli, Michael T. Gallagher, Dirk Muller, Charlene M. Smith, Natesan Venkataraman, James A. West, Peihong Zhang, and Karl W. Koch. Surface modes and loss in air-core photonic band-gap fibers. *Proceedings of SPIE - The International Society for Optical Engineering*, 5000:161–174, 2003.

[42] Hyang Kyun Kim, M.J.F. Digonnet, G.S. Kino, J. Shin, and Shanhui Fan. Simulations of the effect of the core ring on surface and air-core modes in photonic bandgap fibers. *Optics Express*, 12(15), 2004.

[43] K. Saitoh, N.A. Mortensen, and M. Koshiba. Air-core photonic band-gap fibers: the impact of surface modes. *Optics Express*, 12(3), 2004.

[44] Anders Bjarklev. *Singlemode fibre characterisation and applications of mode coupling theory.* PhD thesis, Electromagnetics Institute, Technical University of Denmark, February, 1988.

[45] James A. West, Charlene M. Smith, Nicholas F. Borrelli, Douglas C. Allan, and Karl W. Koch. Surface modes in air-core photonic band-gap fibers. *Optics Express*, 12(8):1485–1496, 2004.

[46] H.K. Kim, J. Shin, S. Fan, M.J.F. Digonnet, and G.S. Kino. Designing air-core photonic-bandgap fibers free of surface modes. *Quantum Electronics, IEEE Journal of*, 40(5):551–556, 2004.

[47] Michel J.F. Digonnet, Hyang Kyun Kim, Jonghwa Shin, Shanhui Fan, and Gordon S. Kino. Simple geometric criterion to predict the existence of surface modes in air-core photonic-bandgap fibers. *Optics Express*, 12(9):1864–1872, 2004.

[48] E. Desurvire. *Erbium Doped Fiber Amplifiers: Principles and Applications.* Wiley-Interscience, 1994.

[49] E. Desurvire, D. Bayart, B. Desthieux, and S. Bigo. *Erbium Doped Fibre Amplifiers - Device and Systems Developments*. Wiley-Interscience, 2002.

[50] W.J. Miniscalco. Erbium-doped glasses for fibre amplifiers at 1500nm. *J. Lightwave Technol*, 9(2):234–250, 1991.

[51] P. Adel and C. Fallnich. High-power ultra-broadband mode-locked Yb^{3+}-fiber laser with 118nm bandwidth. *Opt. Express*, 10(14):622–627, 2002.

[52] A. Liem, T. Limpert, H. Zellmer, A. Tunnermann, V. Reichel, K. Morl, S. Jetschke, S. Unger, H.-P. Muller, J. Kirchhof, T. Sandrock, and A. Harschak. 1.3 kW Yb-doped fiber laser with excellent beam quality. *Conference on Lasers and Electro-Optics, 2004. (CLEO)*, 2:1067–1068, 2004.

[53] H. Zellmer, K. Plamann, G. Huber, H. Scheife, and A. Tünnermann. Visible double-clad upconversion fibre laser. *Electron. Lett.*, 34(6):565–567, 1998.

[54] A. Tünnermann H. Zellmer, S. Buteau and H. Welling. All fibre laser system with 0.1 W output power in blue spectral range. *Electron. Lett.*, 33(16):1383–1384, 1997.

[55] E. Snitzer H. Po, R. Tumminelli, L. Zenteno, F. Hakimi, N. M. Cho, and T. Haw. Double clad high brightness Nd fiber laser pumped by GaAlAs phased array. *Optical Fiber Communication Conference Technical Digest*, PD7, 1989.

[56] C C Renaud, H L Offerhaus, J A Alvarez-Chavez, J Nilsson, W A Clarkson, P W Turner, D J Richardson, and A B Grudinin. Characteristics of Q-switched cladding-pumped ytterbium-doped fiber lasers with different high-energy fiber designs. *IEEE Journal of Quantum Electronics - Institute Electrical and Electronic Engineers*, 37(2):199–206, 2001.

[57] Valérie Doya, Olivier Legrand, and Fabrice Mortessagne. Optimized absorbtion in a chaotic double-clad fiber amplifier. *Optics Letters*, 26(12):872–874, June 2001.

[58] J. Nilsson. Cladding-pumped erbium-doped fiber amplifiers for low noise high-power WDM and analog CATV boosters-new design using ring-doping. *OFC '98. Optical Fiber Communication Conference and Exhibit. Technical Digest. Conference Edition. 1998 OSA Technical Digest Series Vol.2 (IEEE Cat. No.98CH36177)*, pages 38–9, 1998.

[59] M. Soderlund, S. Tammela, P. Poyhonen, M. Leppihalme, and N. Peyghambarian. Amplified spontaneous emission in cladding-pumped L-band erbium-doped fiber amplifiers. *IEEE Photonics Technology Letters*, 13(1):22–4, 2001.

[60] V. Dominic, S. MacCormack, R. Waarts, S. Sanders, S. Bicknese, R. Dohle, E. Wolak, P.S. Yeh, and E. Zucker. 110 W fibre laser. *Electronics Letters*, 35(14):1158–60, 1999.

[61] J. Limpert, A. Liem, H. Zellmer, and A. Tunnermann. 500 W continuous-wave fibre laser with excellent beam quality. *Electronics Letters*, 39(8):645–647, 2003.

[62] C.-H. Liu, B. Ehlers, F. Doerfel, S. Heinemann, A. Carter, K. Tankala, J. Farroni, and A. Galvanauskas. 810 W continuous-wave and single-transversemode fibre laser using 20μm core Yb-doped double-clad fibre. *Electronics Letters*, 40(23):1471–1472, 2004.

[63] R.F. Cregan, J.C. Knight, P.St.J. Russell, and P.J. Roberts. Spontaneous emission from an erbium doped photonic crystal fibre. *Technical Digest. Summaries of papers presented at the Conference on Lasers and Electro-Optics. Postconference Edition. CLEO '99. Conference on Lasers and Electro-Optics (IEEE Cat. No.99CH37013)*, page 559, 1999.

[64] W. J. Wadsworth, J. C. Knight, W. H. Reeves, P. S. J. Russell, and J. Arriaga. Yb^{3+}-doped photonic crystal fibre laser. *Electronics Letters*, 36(17):1452–4, 2000.

[65] W. J. Wadsworth, J. C. Knight, and P. S. J. Russell. Large mode area photonic crystal fibre laser. In *Conference Proceedings - Lasers and Electro-Optics Society Annual Meeting (CLEO)*, page 319, 2001.

[66] K. Furusawa, A. Malinowski, J.H.V. Price, T.M. Monro, J.K. Sahu, J. Nilsson, and D.J. Richardson. Cladding pumped ytterbium-doped fiber laser with holey inner and outer cladding. *Opt. Express*, 9(13):714–720, 2001.

[67] W.J. Wadsworth, R.M. Percival, G. Bouwmans, J.C. Knight, and P.S.J. Russell. High power air-clad photonic crystal fibre laser. *Optics Express*, 11(1):48–53, 2003.

[68] J. Limpert, T. Schreiber, S. Nolte, H. Zellmer, A. Tünnermann, R. Iliew, F. Lederer, J. Broeng, G. Vienne, A. Petersson, and C. Jakobsen. High-power air-clad large-mode-area photonic crystal fiber laser. *Opt. Express*, 11(7):818–823, 2003.

[69] Fiona C. McNeillie, Erling Riis, Jes Broeng, Jacob Riis Folkenberg, Anders Petersson, Harald Simonsen, and Christian Jacobsen. Highly polarized photonic crystal fiber laser. *Optics Express*, 12(17):3981–3987, 2004.

[70] Govind P. Agrawal. *Fiber-Optic Communications Systems*. John Wiley & Sons, Inc., 1997.

[71] J. C. Knight, T. A. Birks, P. St. J. Russel, and J. P. Sandro. Properties of photonic crystal fiber and the effective index model. *J. Opt. Soc. Am. A*, 15:748, 1998.

[72] J.K. Sahu, C.C. Renaud, K. Furusawa, R. Selvas, J.A. Alvarez-Chavez, D.J. Richardson, and J. Nilsson. Jacketed air-clad cladding pumped ytterbium-doped fibre laser with wide tuning range. *Electronics Letters*, 37(18):1116–1117, 2001.

[73] P. Leproux, S. Février, V. Doya, P. Roy, and D. Pagnoux. Modeling and optimization of double-clad fiber amplifiers using chaotic propagation of the pump. *Opt. Fiber Technol.*, 6:324–339, 2001.

[74] B.C. Dickinson, S.D. Jackson, and T.A. King. 10mJ total output from a gain-switched Tm-doped fibre laser. *Optics Communications*, 182(1-3):199–203, 2000.

[75] E. Desurvire, J. R. Simpson, and P. C. Becker. High-gain erbium-doped traveling-wave fibre amplifier. *Optics Letters*, 12(11):888–890, 1987.

[76] B. Pedersen, K. Dybdal, C.D. Hansen, A. Bjarklev, J.H. Povlsen, H. Vendeltorp-Pommer, and C.C. Larsen. Detailed theoretical and experimental investigation of high-gain erbium-doped fiber amplifier. *IEEE Photonics Technology Letters*, 2(12):863–865, 1990.

[77] E. Desurvire, J.W. Sulhoff, J.L. Zyskind, and J.R. Simpson. Study of spectral dependence of gain saturation and effect of inhomogeneous broadening in erbium-doped aluminosilicate fiber amplifiers. *IEEE Photonics Technology Letters*, 2(9):653–655, 1990.

[78] E. Desurvire and J.R. Simpson. Amplification of spontaneous emission in erbium-doped single-mode fibers. *Lightwave Technology, Journal of*, 7(5):835–845, 1989.

[79] W.H. Press, B.P. Flannery, S. A. Teukolsky, and W.T. Vetterling. *Numerical Recipes in C - The Art of Scientific Computing*. Cambridge University Press, 1993.

[80] Jes Broeng, Dmitri Mogilevstev, Stig E. Barkou, and Anders Bjarklev. Photonic crystal fibers: A new class of optical waveguides. *Optical Fiber Technology*, 5:305–330, 1998.

[81] Bo Pedersen, Anders Bjarklev, Jørn Hedegaard Povlsen, Kristen Dybdal, and Carl Christian Larsen. The design of erbium-doped fiber amplifiers. *Journal of Lightwave Technology*, 9(9):1105–1112, September 1991.

[82] Y. Jeong, J.K. Sahu, D.N. Payne, and J. Nilsson. Ytterbium-doped large-core fiber laser with 1.36 kW continuous-wave output power. *Optics Express*, 12(25):6088–6092, 2004.

[83] V.P. Gapontsev, N.S. Platonov, O. Shkuribin, and L. Zaitsev. 400W low-noise single-mode CW ytterbium fiber laser with an integrated fiber delivery. *Lasers and Electro-Optics, 2003. CLEO '03. Conference on*, pages 2134–2136, 2003.

[84] M. Borghesi, A.J. Mackinnon, R. Gaillard, O. Willi, and A.A. Offenberger. Guiding of a 10-TW picosecond laser pulse through hollow capillary tubes. *Physical Review E (Statistical Physics, Plasmas, Fluids, and Related Interdisciplinary Topics)*, 57(5):R4899–902, 1998.

[85] S.O. Konorov, A.B. Fedotov, O.A. Kolelvlatova, V.I. Beloglazov, N.B. Skibina, A.V. Shcherbakov, E. Wintner, and A.M. Zheltikov. Laser breakdown with millijoule trains of picosecond pulse transmitted through a hollow-core photonic-crystal fibre. *Journal of Physics D: Applied Physics*, 36(12):1375–1381, 2003.

[86] J.D. Shephard, J.D.C. Jones, D.P. Hand, G. Bouwmans, J.C. Knight, P.St.J. Russell, and B.J. Mangan. High energy nanosecond laser pulses delivered single-mode through hollow-core PBG fibers. *Optics Express*, 12(4):717–723, 2004.

[87] G. Humbert, J.C. Knight, G. Bouwmans, P.St.J. Russell, D.P. Williams, P.J. Roberts, and B.J. Mangan. Hollow core photonic crystal fibers for beam delivery. *Optics Express*, 12(8):1477–1484, 2004.

[88] T.P. Hansen, J. Broeng, C. Jakobsen, G. Vienne, H.R. Simonsen, M.D. Nielsen, P.M.W. Skovgaard, J.R. Folkenberg, and A. Bjarklev. Air-guiding photonic bandgap fibers: Spectral properties, macrobending loss, and practical handling. *Lightwave Technology, Journal of*, 22(1):11–15, 2004.

[89] Thorkild Sørensen, Nikola Ivanov Nikolov, Ole Bang, Anders Bjarklev, Kristian Hougaard, Kim Per Hansen, and Jens Juul Rasmussen. Cob-web microstructered fibers optimized for supercontinuum generation with picosecond pulses. In *Non-Linear Guided Waves 2004*, page WC4, 2004.

[90] S.W. Allison, G.T. Gillies, D.W. Magnuson, and T.S. Pagano. Pulsed laser damage to optical fibers. *Applied Optics*, 24(19):3140–5, 1985.

[91] F. Rainer, L.J. Atherton, J.H. Campbell, F.D. DeMarco, M.R. Kozolowski, A.J. Morgan, and M.C. Staggs. Four-harmonic database of laser-damage testing. *Procedings SPIE*, 1624(116), 1992.

[92] Sheila Galt, Mats Sjoberg, Manuel Lopez Quiroga-Teixeiro, and Sverker Hard. Optical breakdown in fused silica and argon gas: Application to Nd:YAG laser limiter. *Applied Optics*, 42(3):579–584, 2003.

[93] N. Kuzuu, K. Yoshida, H. Yoshida, T. Kamimura, and N. Kamisugi. Laser-induced bulk damage in various types of vitreous silica at 1064, 532, 355, and 266 nm: evidence of different damage mechanisms between 266-nm and longer wavelengths. *Applied Optics*, 38(12):2510–15, 1999.

List of Publications

[1] **Kristian Hougaard**, Anders Bjarklev, Erik Knudsen, Stig E. Barkou Libori, and Jesper Riishede. Coupling to photonic crystal fibres. *OFC 2002*, (ThGG11), March 2002.

[2] **Kristian Hougaard**, Anders Bjarklev, and Jes Broeng. Low pump power photonic crystal fibre amplifiers. *Danish Optical Society Annual Meeting*, November 2003.

[3] **Kristian Hougaard**, Anders Bjarklev, and Jes Broeng. Low pump power photonic crystal fibre amplifiers. *CLEO 2003*, (CWA59), June 2003.

[4] **Kristian Hougaard**, Anders Bjarklev, and Jes Broeng. Low pump power photonic crystal fibre amplifiers. *Electronics Letters*, 39(7):599–600, April 2003.

[5] **Kristian Hougaard** and Frederik D. Nielsen. Amplifiers and lasers in pcf configurations. *Journal of Optical and Fiber Communications Reports*, 1(1):63–83, 2004.

[6] Maja Albertsen, Jesper Lægsgaard, Stig E. Barkou Libori, **Kristian Hougaard**, Jesper Riishede, and Anders Bjarklev. Coupling-reducing k-points for photonic crystal fibre calculations. *Photonics and Nanostructures, Fundamentals and Applications*, 1/1:43–53, 2003.

[7] Anders Bjarklev, Kim P. Hansen, Theis P. Hansen, **Kristian Hougaard**, Erik Knudsen, Stig Libori, Jesper Lægsgaard, Martin D.

Nielsen, Jesper Riishede, and Thomas T. Larsen. Photonic crystal fibres - the state-of-the-art. *ECOC 2002*, 1(S1.1), September 2002.

[8] Anders Bjarklev, **Kristian Hougaard**, Jesper Riishede, Stig Libori, Erik Knudsen, and Jes Broeng. Photonic crystal fibres - a variety of applications. *Photonics Praque 2002*, April 2002.

[9] Anders Bjarklev, Jesper Bo Jensen, Jesper Riishede, Jes Broeng, Jesper Lægsgaard, Thomas Tanggaard Larsen, Thorkild Sørensen, **Kristian Hougaard**, and Ole Bang. Photonic crystal structures in sensing technology. *Second European Workshop on Optical Fibre Sensors*, (Invited paper, proceedings, page 9-16), 2004.

[10] Michael H. Frosz, **Kristian Hougaard**, Stig E. Barkou Libori, Jesper Lægsgaard, and Anders Bjarklev. Radial deformation losses in photonic crystal fibers. *Journal of Optics A*, 5(3):268–271, 2003.

[11] Rune S Jacobsen, Jesper Laegsgaard, Anders Bjarklev, and **Kristian Hougaard**. Very low zero-dispersion wavelength predicted for single-mode modified-total-internal-reflection crystal fibre. *Journal of Optics A: Pure and Applied Optics*, 6(6):604–607, 2004.

[12] Jesper Bo Jensen, Jesper Riishede, Jes Broeng, Jesper Lægsgaard, Thomas Tanggaard Larsen, Thorkild Sørensen, **Kristian Hougaard**, Erik Knudsen, Stig E. B. Libori, , and Anders Bjarklev. Photonic crystal fibers; fundamental properties and applications within sensors. *IEEE Sensors, invited paper*, 2003.

[13] Jesper Bo Jensen, Jesper Riishede, Jesper Lægsgaard, Thomas Tanggaard Larsen, Thorkilk Sørensen, **Kristian Hougaard**, Erik Knudsen, Stig E. Barkou Libori, Anneline Carlsen, Jesper Bevensee Jensen, Anders Bjarklev, L.H. Pedersen, P.E. Hoiby, L.B. Nielsen, Jes Broeng, and J.R. Folkenberg. Photonic crystal fiber based sensors. (1):23–27, 2003.

[14] Jesper Lægsgaard, Stig E. Barkou Libori, **Kristian Hougaard**, Jesper Riishede, Thomas Tanggaard Larsen, Theis Peter Hansen, Kim Per Hansen, Martin Dybendal Nielsen, Jesper Bo Jensen, and Anders Bjarklev. Dispersion properties of photonic crystal fibers - issues and opportunities. *MRS fall*, (W.7.1.1), 2003.

[15] Jesper Lægsgaard, Kim Per Hansen, Martin Dybendal Nielsen, Theis Peter Hansen, Jesper Riishede, **Kristian Hougaard**, Thorkild Sørensen, Thomas Tanggaard Larsen, Niels Asger Mortensen, Jes Broeng, Jesper Bo Jensen, and Anders Bjarklev. Photonic crystal fibers. *IMOC, invited paper*, 1:259–264, 2003.

[16] Jesper Riishede, **Kristian Hougaard**, Stig Libori, Thomas Søndergaard, and Anders Bjarklev. Bragg gratings in index-guiding photonic crystal fibres. *ECOC 2002*, 3(3.4.4), September 2002.

[17] Thorkild Sørensen, **Kristian Hougaard**, and Anders Bjarklev. Higher-order mode dispersion in photonic crystal fibres. *ECOC 2003*, 3(We 4.P.36):628–629, September 2003.

[18] Thorkild Sørensen, Nikola Ivanov Nikolov, Ole Bang, Anders Bjarklev, **Kristian Hougaard**, Kim Per Hansen, and Jens Juul Rasmussen. Cob-web microstructered fibers optimized for supercontinuum generation with picosecond pulses. *Non-Linear Guided Waves 2004*, (WC4), 2004.

[19] Thorkild Sørensen, Nikola Ivanov Nikolov, Ole Bang, Anders Bjarklev, **Kristian Hougaard**, and Kim Per Hansen. Dispersion engineered cob-web photonic crystal fibers for efficient supercontinuum generation. *Optical Fiber Communication Conference, 2004. OFC 2004*, 1:572–574, 2004.

List of Figures

List of Acronyms

ASE	amplified spontaneous emission
COF	conventional optical fibre
EDFA	erbium doped fibre amplifier
ESA	excited state absorption
FEM	finite element method
FSM	fundamental space-filling mode
GSA	ground state absorption
LIDT	laser induced damage threshold
LMA	large-mode area
MFD	mode-field diameter
MPB	MIT Photonic Bands
MTIR	modified total internal reflection
NA	numerical aperture
PBG	photonic bandgap
PCF	photonic crystal fibre
PWM	plane wave method
RE	rare-earth

RED	rare-earth doped
SE	spontanous emission
SEM	scanning electron microscope
SIF	step-index fibre
SNR	signal-to-noise ratio
TIR	total internal reflection